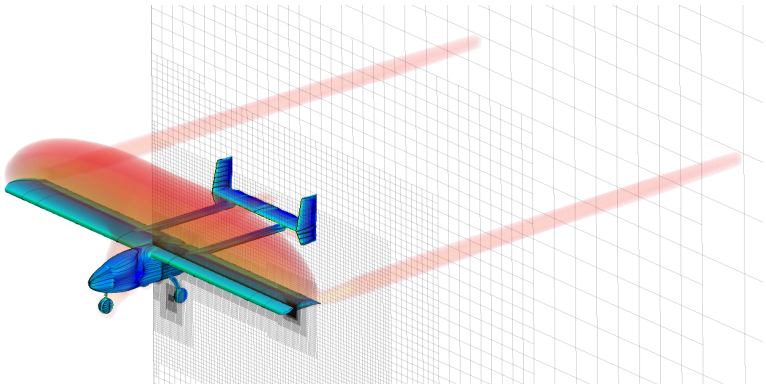

Best Practice Guidelines in External Aerodynamics CFD

Applied to Unmanned Aerial Vehicles at Cruise Conditions

Ricardo José Cabral Veríssimo

Alferes-Aluno ENGAER 136867-C

Thesis to obtain the Master of Science Degree in

Military Aeronautical Sciences - Aeronautical Engineering

Supervisor: Dr. Nelson Pereira Caetano Marques
Co-supervisors: Major ENGEL João Manuel Moreira Simões
Capitão ENGAER Ana Sofia Andrês dos Reis Lesiário

Examination Committee

Chairperson:	MGen PILAV Joaquim Manuel Nunes Borrego
Supervisor:	Dr. Nelson Pereira Caetano Marques
Co-supervisors:	Major ENGEL João Manuel Moreira Simões
	Capitão ENGAER Ana Sofia Andrês dos Reis Lesiário
Member of the Committee:	Major ENGAER Carlos Pereira da Silva

Sintra, July 2016

“Basic research is what I’m doing when I don’t know what I am doing.”

Wernher von Braun

Dedico este trabalho à minha família e amigos.
Aos primeiros, por me ajudarem a chegar ao destino.
Aos últimos, pelos desvios no caminho.

Agradecimentos

Aos meus orientadores, o Dr. Nelson Marques, a Capitão Ana Lesiário e o Major João Simões, agradeço todo o apoio, *feedback* e disponibilidade oferecidos, assim como a acessibilidade e paciência demonstradas desde o início deste trabalho.

Ao Dr. Nelson Marques, em particular, gostaria ainda de agradecer a hospitalidade e a oportunidade que me ofereceu ao disponibilizar a infraestrutura da BlueCAPE para a concretização da componente computacional do projecto. Aproveito esta oportunidade para agradecer também todo o apoio que recebi por parte do pessoal da BlueCAPE, nomeadamente: Bruno Santos, Jorge Azevedo, Pedro Freitas, Rui Gabriel e Vera Rodrigues. Este trabalho não teria sido possível sem a sua ajuda e boa vontade.

Ao pessoal do Centro de Investigação, Desenvolvimento e Inovação da Força Aérea (CIDIFA), e respectivo Núcleo de Operações UAV, gostava de agradecer todo o investimento no apoio ao trabalho experimental aqui apresentado. Destes destaco, principalmente, o SAJ Paulo Mendes e SCH Fernando Santos, pelas muitas horas despendidas na preparação da aeronave não tripulada ANTEX-X02 ALFA NC 17507 (A07) para voo e pela qualidade do trabalho realizado. Agradeço ainda ao Major Santos por ter colocado os recursos do Laboratório de Aeronáutica da Academia da Força Aérea ao meu dispôr, à Major Paula Gonçalves pela ajuda na preparação de toda a documentação oficial requerida pela Autoridade Aeronáutica Nacional para a autorização dos ensaios em voo, e, por último, ao Capitão João Caetano pela prontidão, pragmatismo e profissionalismo demonstrados, juntamente com o SAJ Jorge Fernandes, SAJ Joaquim Gomes e SAJ Paulo Teixeira, durante o longo dia de testes no Centro de Operações UAV, no Centro de Formação Militar e Técnica da Força Aérea (CFMTFA).

Quero também agradecer a participação e excelente desempenho do estagiário João Vieira, aluno da Universidade de Manchester, no Reino Unido, nomeadamente, nas fases de preparação dos ficheiros CAD dos modelos para teste em túnel aerodinâmico e impressão 3D. A experiência e *know-how* que partilhou comigo neste domínio foram uma grande mais-valia para todo o trabalho. Agradeço ainda ao CADAL André Gomes, CADAL Gonçalo Gameiro e CADAL João Vilaça, pelo interesse demonstrado neste trabalho e pela ajuda prestada na preparação e execução dos ensaios em túnel aerodinâmico.

Aos meus camaradas naquele que é o melhor curso que jamais passou e alguma vez passará na Academia da Força Aérea, obrigado pelo apoio. Em particular, agradeço ao ALF Miguel Fonseca pela ajuda na preparação do sistema de aquisição de dados para os ensaios experimentais.

Por último, gostaria de expressar a minha profunda gratidão pela contribuição do Professor Dr. Vasco de Brederode, o qual recordo pela humildade e disponibilidade que me demonstrou. Considero-me afortunado pela oportunidade que me foi proporcionada quando o conheci, gozando hoje do privilégio de ter aprendido com a sua vasta experiência.

Resumo

O presente trabalho visa o estabelecimento de uma metodologia para a caracterização aerodinâmica de veículos aéreos não-tripulados (VANT) em condições de cruzeiro no âmbito de projectos de investigação na Força Aérea Portuguesa. Este estudo foca-se no preparação de modelos baseados na mecânica de fluidos computacional (CFD) e de testes em túnel de vento e voo que permitam correlação e validação cruzada de resultados. O caso de estudo é um VANT de classe I que opera a baixas velocidades subsónicas. Informação relativa a esta aplicação específica deste tipo de estudos é limitada na comunidade científica e, dado o crescente interesse em tecnologia ligada a VANTs, considera-se altamente relevante para a industria aeroespacial tanto no sector civil como militar.

Casos de validação bidimensionais (perfil alar) a tridimensionais (asa finita) são apresentados por forma a aferir a precisão dos resultados e as limitações dos métodos utilizados comparativamente a dados publicados. As simulações foram implementadas em Star-CCM+ e testes em túnel de vento foram executados numa secção de teste aberta com meio-modelos, equipados com tomadas de pressão e produzidos por impressão 3D, para escoamentos entre os números de Reynolds de 3.0×10^5 e 4.1×10^5. Testes de visualizacção de escoamentos foram efectuados por forma a obter informacção adicional para uma validacção qualitativa. Os testes de voo introduzem equipamentos desenvolvidos específicamente para pequenas plataformas aéreas não tripuladas a partir de componentes electrónicos de baixo custo. Os resultados computacionais correlacionam-se favorávelmente com dados publicados e estão em excelente acordo com os resultados dos testes de visualização de escoamentos. As leituras de pressão nas tomadas de pressão em túnel de vento correlacionam-se bem com os resultados experimentais mas não foram bem sucedidas em voo. As forças aerodinâmicas medidas em túnel de vento não validam as previsões computacionais mas aparentam subestimar sustentação e sobrestimar a resistência aerodinâmica consistentemente.

Palavras-chave: Veículos Aéreos Não-Tripulados, Aerodinâmica de Escoamentos Exteriores, Mecânica de Fluidos Computacional, RANS, Túnel Aerodinâmico, Ensaios em Voo, Impressão 3D.

Abstract

The purpose of this paper is to establish a methodology for the aerodynamic characterization of unmanned aerial vehicles at cruise conditions in the Portuguese Air Force, focusing on the set-up of computational fluid dynamics models and both wind tunnel and flight testing experimental procedures that warrant correlation and cross-validation of results. The case study is a Class I UAV with a twin boom pusher prop configuration that operates at low subsonic speeds. Information for this specific application was found to be limited in the scientific literature and, given the increasing interest in unmanned aerial vehicle technology, it is considered highly relevant for the aerospace industry on civil and military sectors alike.

2-Dimensional (airfoil) and 3-dimensional (finite wing) validation test cases are presented in order to access the accuracy of the results and limitations of the employed methods against published data. Numerical simulations were implemented with commercial software Star-CCM+ and wind tunnel tests were executed in an open test section with a reflection plane and 3D printed semi-span models with pressure taps, for Reynolds numbers ranging from 3.0×10^5 to 4.1×10^5. Flow visualization wind tunnel tests with china-clay were performed in order to collect additional qualitative experimental validation data. Flight testing introduces several proof-of-concept equipments featuring low-cost sensors for unmanned flight data acquisition in small platforms.

The computational results correlate favourably with the available reference data and are in excellent agreement with the experimental flow visualization results. Pressure tap measurements from wind tunnel tests compare well against computational results but were unsuccessful in flight. Wind tunnel force coefficient results do not validate the computational predictions, but appear to consistently under-predict lift and over-predict drag.

Keywords: Unmanned Aerial Vehicles, External Aerodynamics, Computational Fluid Dynamics, Reynolds Averaged Navier-Stokes, Wind Tunnel Testing, Flight Testing, 3D Printing.

Contents

Agradecimentos vii
Resumo ix
Abstract xi
List of Tables xv
List of Figures xx
Nomenclature xxii

1 Introduction **1**
1.1 Context and Motivation 1
1.2 Objectives 3
1.3 Approach 3
1.4 Outline 4

2 State-of-the-Art **5**
2.1 Low Reynolds Number Aerodynamics 5
2.2 Computational Fluid Dynamics 9
2.2.1 The Use of CFD 9
2.2.2 Turbulence and Transition Modelling 12
2.2.3 Meshing and Near Wall Treatment 17
2.2.4 Errors, Uncertainties, Validation and Verification 22
2.2.5 Sensitivity Tests and Grid Independence 25
2.3 Wind Tunnel Testing 26
2.3.1 Background and Basic Principles 26
2.3.2 Testing Facilities, Measurements and Models 28
2.3.3 Scalling to Free Flight 37
2.4 Note on the Complementarity of CFD and Wind Tunnel Testing 39

3 Methods **43**
3.1 The Application and Validation Cases 43
3.2 Computational Simulation 45
3.3 Flight Testing 47
3.4 Wind Tunnel Testing 48

4 Results **49**
4.1 2-Dimensional Validation Case 49
4.1.1 Sensitivity Tests 49
4.1.2 Grid Independence and Uncertainty Analysis 51
4.1.3 Aerodynamic Performance Curves 53
4.1.4 Chordwise Pressure Distribution 54
4.1.5 Flow Features 56
4.2 3-Dimensional Validation Case 60
4.2.1 Grid Independence and Uncertainty Analysis 60
4.2.2 Aerodynamic Performance Curves 62
4.2.3 Chordwise Pressure Distribution 64
4.2.4 Flow Visualization 64
4.3 ALFA Application Case 66
4.3.1 Cruise Angle of Attack 67
4.3.2 Aerodynamic Performance, Grid Independence and Uncertainty Analysis 68
4.3.3 Chordwise Pressure Distribution 69
4.3.4 Flow Visualization 71

5 Conclusions **75**

6 Future Work and Recommendations **77**

Bibliography **86**

A Best Practice Guidelines **87**

List of Tables

4.1 Summary of set-up specifications. 50
4.2 Summary of sensitivity test results. 51
4.3 Grid independence and uncertainty analysis. 52
4.4 Comparison between numerical and experimental results. 54
4.5 Comparison between experimental and computational flow feature location results. 57
4.6 Summary of set-up specifications. 60
4.7 Grid independence and uncertainty analysis. 61
4.8 Comparison between numerical and experimental results. 63
4.9 Summary of set-up specifications. 67
4.10 Grid independence and uncertainty analysis. 68

List of Figures

2.1 Boundary layer over a flat plate [Visavale, accessed May 23rd, 2016]. 6

2.2 Laminar separation bubble [Ananda et al., 2012]. 7

2.3 The effects of LSBs: (a) Aerodynamic hysteresis; (b) LSB drag polar, the well-behaved polar is similar to that of conventional airfoils at Reynolds numbers above 10^6 [Lissaman, 1983]. 8

2.4 Flow over high AR finite wing [Ananda et al., 2012]. 9

2.5 Estimate of CPU resources for RANS and wall-resolved LES for a single turbine blade [Menter, 2011]. 11

2.6 Oil Flow Visualization vs SST vs an RSM model. Improved predictions of the size of the corner separation bubble can be observed [Menter, 2011]. 15

2.7 (a) Regular grid; (b) Body fitted grid [Agarwal, 1999]. 18

2.8 (a) Structured Grid [Agarwal, 1999]; (b) Unstructured grid [Muller, accessed May 23rd, 2016]. 18

2.9 (a) Bock Structured Grid (b) and Chimera Grid [Agarwal, 1999]; (c) Hybrid Grid, with prismatic layers [Linkoping University, accessed May 23rd, 2016]. 19

2.10 Unstructured mesh with local refinement (from grid adaptation) in order to properly capture shocks [Agarwal, 1999]. 19

2.11 (a) Adimensional velocity boundary layer profile for a flat plate for a null pressure gradient; (b) High y+ first grid point; (c) Low y+ first grid point [Ewing, 2015]. 21

2.12 Applicability of wall functions [LEAP CFD Team, accessed May 23rd, 2016] 21

2.13 (a) Typical layout of an open circuit wind tunnel; (b) Typical layout of a closed circuit wind tunnel [Barlow et al., 1999]. 29

2.14 Examples of PSP results against CFD solutions (a) For a typical airliner configuration [Jahanmiri, 2011] and (b) for a typical jet-fighter configuration [Jackson, accessed May 23rd, 2016]. 31

2.15 Schematic representation of PSP concept [McLachlan and Bell, 1995]. 31

2.16 (a) Streamlines past an airfoil visualized by smoke wire techniques; (b) Flow visualization with the tuft net method [Barlow et al., 1999] 32

2.17 Fluorescent mini-tufts under an ultraviolet light source [Barlow et al., 1999]. 33

2.18 (a) Coloured oils with natural light [ONERA, accessed May 23rd, 2016]; (b) Fluorescent oils in UV light [NASA, accessed May 23rd, 2016a]. 33
2.19 China clay flow visualization [University of Washington, College of Engineering, accessed May 23rd, 2016]. 34
2.20 Aerospace industry grade semi-span wind tunnel model [NASA, accessed May 23rd, 2016b]. 35

3.1 The Antex-X02 ALFA. 43
3.2 The Wortmann FX63-137 airfoil. 44

4.1 Numerical uncertainty due to discretization for the calculated lift (a) and drag (b) coefficients. The grid characteristic number, r_i, on the horizontal axis, is defined as $r_i = \sqrt{\frac{h_f}{h_i}}$, where h_f refers to the number of cells in the most refined mesh and h_i is the number of cells in each different grid. 52
4.2 (a) Lift coefficient grid independence; (b) drag coefficient grid independence. 52
4.3 Comparison between numerical results and published experimental data: (a) lift coefficient ; (b) drag coefficient. 53
4.4 Comparison between numerical results and published experimental data: (a) lift coefficient ; (b) drag coefficient; (c) drag polar. 54
4.5 Comparison between published experimental pressure coefficient distribution data from pressure tap measurements [Wo and Covert, 1989], Star-CCM+ simulation results and XFLR5 calculations. 55
4.6 Pressure coefficient distribution over the Wortmann FX63-137 airfoil for different angle of attack values from Star-CCM+ simulations. 56
4.7 Pressure coefficient distribution over the Wortmann FX63-137 airfoil for fully turbulent *(dashed line)* and transition predictive simulations *(full line)*. 56
4.8 Contour plot of the velocity of the flow field (a) and streamlines around the airfoil (b). . . . 57
4.9 Detail of recirculating flow regions associated with laminar separation bubbles (a) and trailing edge turbulent separation (b). 57
4.10 Flow feature location from: (a) the skin friction coefficient distribution [McGranahan and Selig, 2003]; and (b) pressure coefficient distribution [Hu and Yang, 2008]. 58
4.11 Skin friction distribution, over the surface of the Wortmann FX63-137 airfoil, detailing separated flow location and extent (negative values). 58
4.12 Comparison of important flow feature locations between numerical solutions and published experimental data. 59
4.13 Turbulent boundary layer solution from Star-CCM+ simulations superimposed over theoretical turbulent boundary layer approximations, namely for the viscous sublayer (*full line*) and the logarithmic and defect layers (log-law, *dashed line*) [White and Corfield, 2006]. . . 59
4.14 Numerical uncertainty due to discretization for the calculated lift (a) and drag (b) coefficients. 61
4.15 (a) Lift coefficient grid independence; (b) drag coefficient grid independence. 61

4.16 Comparison between numerical results and experimental data: (a) lift coefficient ; (b) drag coefficient. 62
4.17 Comparison between numerical results and experimental data: (a) lift coefficient; (b) drag coefficient; (c) drag polar. 63
4.18 Comparison between published 2-dimensional experimental pressure coefficient distribution data from pressure tap measurements (from [Wo and Covert, 1989]) and both infinite wing (2D) and finite wing (3D, from the airfoil section across the symmetry plane) Star-CCM+ simulation results. 64
4.19 Comparison between china-clay flow visualization wind tunnel results (*left*) and skin friction distribution and near surface streamlines from CFD simulations (*right*) over the upper (a) and lower (b) wing surfaces. 65
4.20 Detail of the comparison between china-clay flow visualization wind tunnel results (*top*) and skin friction distribution and near surface streamlines from CFD simulations (*bottom*) over the upper (a) and lower (b) wing surfaces. 66
4.21 Wind tunnel calibration curve correcting for fuselage and wing interference. The reference angle (0°) for the sensor output *(horizontal axis)* is offset to match the geometric orientation of the wingroot cross-section chord line. 68
4.22 Numerical uncertainty due to discretization for the calculated lift (a) and drag (b) coefficients. 69
4.23 (a) Lift coefficient grid independence; (b) drag coefficient grid independence. 69
4.24 Comparison between numerical results and experimental data: (a) lift coefficient ; (b) drag coefficient. 70
4.25 Pressure coefficient distribution from wind tunnel scale model pressure tap measurements, from two different equipments, and Star-CCM+ simulations at 48.6% of semi-wingspan. 70
4.26 Pressure coefficient distribution from pressure tap measurements with the data system, both from the scale model and the actual UAV (placed inside the wind tunnel test section), and Star-CCM+ simulations. 71
4.27 Comparison between the typical in-flight pressure coefficient distribution profile (collected with the data system and relative to a randomly selected levelled flight segment of the testing circuit) and Star-CCM+ results. 72
4.28 Comparison between china-clay flow visualization wind tunnel results (*left*) and skin friction distribution and near surface streamlines from CFD simulations (*right*) over the upper wing surface. 72
4.29 Comparison between china-clay flow visualization wind tunnel results (*left*) and skin friction distribution and near surface streamlines from CFD simulations (*right*) over the lower wing surface. 72
4.30 Detail of the comparison between china-clay flow visualization wind tunnel results (*bottom*) and skin friction distribution and near surface streamlines from CFD simulations (*top*) over the upper (a) and lower (b) wing surfaces. 73

Nomenclature

Acronyms

2D	2-Dimensional
3D	3-Dimensional
A07	ANTEX-X02 ALFA NC 17507
AFA	Academia da Força Aérea or Air Force Academy
ALFA	ANTEX-X02 ALFA
AoA	Angle of Attack
CFD	Computational Fluid Dynamics
CIDIFA	Centro de Investigação, Desenvolvimento e Inovação da Força Aérea
D3	Dull, Dirty and Dangerous
FSI	Fluid-Structure Interaction
FT	Flight Testing
ISA	International Standard Atmosphere
ISR	Intelligence, Surveillance and Reconnaissance
LABAER	Laboratório de Aeronáutica
LRN	Low Reynolds Number
LSB	Laminar Separation Bubble
MTOW	Maximum Take-Off Weight
NATO	North Atlantic Treaty Organization
PCB	Printed Circuit Board
PITVANT	Projecto de Investigação e Tecnologia em Veículos Aéreos Não Tripulados
PrtAF	Portuguese Air Force

R&D	Research and Development
STOL	Short Take-Off and Landing
UAV(s)	Unmanned Aerea Vehicle(s)
UN	United Nations
V&V	Verification and Validation
VANT	Veiculos Aéreos Não-Tripulados
WT	Wind Tunnel
WTT	Wind Tunnel Testing

Greek symbols

α	Angle of attack.
μ	Molecular viscosity coefficient.
ρ	Density.

Roman symbols

C_D	Coefficient of drag.
C_L	Coefficient of lift.
p	Pressure.
U	Velocity

Subscripts

∞	Free-stream condition.
i, j, k	Computational indexes.
n	Normal component.
x, y, z	Cartesian components.
0	Reference condition.

Chapter 1

Introduction

1.1 Context and Motivation

The past few decades have registered a steady growth in interest in the design and development of small unmanned aerial vehicles (UAVs), that are by now widely recognised as capable platforms over a large variety of military applications, starting with reconnaissance and surveillance missions, that are ideally suited for smaller configurations, either remotely piloted or autonomous [Mueller and DeLaurier, 2003].

UAV presence in armed conflicts gained relevance mainly after their successful employment during the 1982 operation Peace for Galilee by the Israeli Air Force, that used them to suppress Syrian air defences, and has become increasingly frequent since the advent of the global war on terrorism in 2001. Successful roles played by UAVs both at peace and during these conflicts motivated military doctrines to evolve and impose additional requirements on performance and capacity for future iterations of these platforms.

According to [Morgado and Sousa, 2009], one of the decisive arguments leading to these platforms' broader operational spectrum was recognising their potential to replace conventional aircraft and reduce risks to human life on missions categorized as Dull, Dirty and Dangerous (D3), i.e., missions where human tolerance levels are restrictive, missions over contaminated environments and missions on highly hostile territories, respectively.

This flexible operability, combined with lower associated life cycle costs (from design and production to operation and maintenance) when compared to conventional aircraft make UAVs an extremely cost-effective solution at a time when efficient allocation of resources is, more than ever before, a world-wide priority given the current global economical climate.

Portuguese Air Force's (PrtAF) research on unmanned aerial vehicle technology and operation began in 1996 at the Air Force Academy (AFA), in the context of these platform's prospective aptitude to assist peace maintenance operations – in the context of international commitments with the UN and NATO – and, most especially, maritime surveillance and search and rescue missions, inherent to Portugal's vast Exclusive Economic Zone. This vision, aided by modern trends of systematic miniaturization

of electrical components and increasing affordability of a wide assortment of sensors, has opened the door to technological innovation in the aeronautical industry for countries like Portugal.

The PITVANT program (Projecto de Investigação e Tecnologia em Veículos Aéreos Não Tripulados), which ended in 2015, successfully produced several Class I platforms (under 150 kg) over the last two decades [Barros and Gonçalves, 2015], and research on this subject continues with Class II models (under 600 kg) currently in development [Barros, 2015].

Presently, one of the main challenges on UAV development in the PrtAF is the aerodynamic and structural optimization of these vehicles as they require, at the outset, a robust strategy for aerodynamic characterization of the flow around each platform, which is generally is done for cruise conditions, since aircraft are typically optimized for maximum performance and efficiency at this flight regime.

There are typically three different ways to attempt to solve fluid dynamics and, particularly in this case, external aerodynamics problems: pure theory, pure experiment and computational fluid dynamics (CFD) [Anderson Jr, 1995]. Pure experiment came first, in the seventeenth century, from England and France. Pure theory came second, gradually developing over the eighteenth and nineteenth centuries, still mainly in Europe. As recently as in 1960, fluid dynamics would still be operating within a ”two-approach world”. However, with the advent of the high-speed computational power almost everyone enjoys today and the development of accurate numerical algorithms for solving physical problems, computational fluid dynamics entered the fray.

Even though none of the stated methods should replace one another, but only complement each other, there are several advantages to the most modern take on fluid dynamics. The ready availability of robust commercial CFD software and the massive increase in affordable computer speed and memory capacity over the last twenty years have led to a steady reduction in simulation costs when compared to the conventional experimental methods, making CFD simulations solving the Reynolds Averaged Navier-Stokes equations (RANS) the industrial standard tool for the design, analysis and performance determination of engineering problems involving fluid flow [Casey et al., 2000].

However, simplifying assumptions made in CFD models mean that there is no guarantee that the results are a good representation of the real world. In this specific case, for example, there are low Reynolds numbers (LRN) considerations that have to be taken into account due to the low subsonic operating speeds of small UAVs. And in that sense, analytical and experimental data, typically collected from wind tunnel testing or in-flight (when dealing with aerodynamics problems), or even computational results from simpler tools that can offer some sort of validation become extremely valuable.

Literature on CFD external aerodynamics for small unmanned aerial vehicles and, particularly, the availability of validation data for problems of this nature was found to be limited in the scientific community. Given the stated interest in unmanned aerial vehicle technology, the popularity of computational fluid dynamics and the relevancy of experimental data, the present work is considered highly relevant for the aerospace industry on civil and military sectors alike.

1.2 Objectives

In this context, the purpose of this dissertation is to propose a methodology for the aerodynamic characterization of unmanned aerial vehicles at low subsonic speed cruise conditions, focusing on the set-up of computational fluid dynamics models and both wind tunnel and flight testing experimental procedures that warrant correlation and cross-validation of results, in order to support aerodynamic and structural optimization efforts in the Portuguese Air Force.

Specifically, this dissertation presents the following goals:

- Evaluation of current state-of-the-art standard and recommended practices in both computational and experimental external aerodynamics;
- Development of a computational fluid dynamics model;
- Construction of a scale model for wind tunnel testing;
- Development of a data system equipped with the required sensors for on-board acquisition and recording of relevant flight data during flight testing;
- Execution of the respective simulations, wind tunnel tests and flight tests;
- Validation of procedures by use of test cases;
- Correlation of results obtained by computational and experimental methods.

A few observations should be made on the nature of these statements in light of institutional priorities. Firstly, it is of great interest that modern, low-cost and easy implementation solutions are explored in achieving these goals. Secondly, the fourth objective implies that one of the currently operational unmanned aerial vehicles in the PrtAF will be selected as the application study (or case study), so that flight testing is possible within the available time window. Finally, all these goals are directed towards the long term objective of establishing internal best practices that enable CFD and wind tunnel testing as viable and complementary tools for UAV external aerodynamics in the PrtAF.

1.3 Approach

These challenges are approached under the fundamental assumption that it is possible to establish a set of computational and experimental procedures, prepared and executed in parallel, following recommendations from the literature, that lends itself to a straight forward co-relation of results and, hopefully, their cross-validation.

The computational component of the project is directed towards the aerodynamic characterization of the UAV at cruise conditions, assuming symmetric flow conditions and hence explicitly modelling only half of the computational domain. The commercial software Star-CCM+ is used to perform several steady, incompressible, low Reynolds number, external aerodynamics simulations with a Reynolds Averaged Navier-Stokes (RANS) approach. Important mesh and physics modelling parameters are studied

and their influence on results is evaluated, in line with past studies performed for different configurations. Discussed topics include the computational domain, the mesh base size, local mesh refinement strategies, turbulence model selection, prediction of the onset of transition and the prescription of appropriate boundary conditions, amongst others.

The experimental component of this project comprises both wind tunnel and flight testing. Equipment and infrastructure currently available in the Air Force Academy (AFA) Research Center is employed and complemented with the introduction of innovative low-cost solutions with application for the aeronautical community, namely: the use of 3D printing for the rapid prototyping of wind tunnel test models and components used in flight testing, and the implementation of low-cost sensors and Arduino micro-controller based in-flight data acquisition systems.

Quantitative wind tunnel data comprises steady force measurements for lift and drag from a six-component balance and steady surface pressure distribution from pressure taps on a semi-span scale model over a chordwise section of the wing. Additional qualitative information is collected with the china clay flow visualization technique. Flight data comprises pressure readings from pressure taps at the same chordwise wing section on the actual aircraft and angle of attack measurements at cruise conditions.

Validation test cases for the proposed methods are performed by means of simpler two-dimensional (airfoil) and three-dimensional (finite wing) problems for which sufficient and reliable published data is available for comparison purposes.

1.4 Outline

Chapter 2 comprises a brief review of the state-of-the-art on the most relevant subjects, namely, low Reynolds number aerodynamics, computational fluid dynamics and wind tunnel testing. In this chapter, fundamental principles are introduced, major challenges identified, and currently available solutions discussed.

Chapter 3 covers the methods employed during the course of this work detailing both the numerical and the experimental methodologies.

Chapter 4 presents and discusses the validation results of both the 2-Dimensional (2D) and 3-Dimensional (3D) validation cases and both the computational and experimental results relative to the Antex-X02 ALFA unmanned aerial vehicle application case.

Chapter 5 draws the main conclusions of the project and evaluates the outcome in light of the original objectives. Here are discussed the practical applications of relevant achievements and their limitations.

Future developments and recommendations are proposed in Chapter 6, setting pointers on the way forward while accounting for the progress made.

Chapter 2

State-of-the-Art

2.1 Low Reynolds Number Aerodynamics

The Reynolds number of a fluid flow is a non-dimensional value that characterizes the ratio between the inertial and viscous forces acting on a fluid, and is given by:

$$Re = \frac{\rho U_\infty L}{\mu} \tag{2.1}$$

where ρ is the density of the fluid, L is the characteristic length (in external aerodynamics cases, the wing's mean chord is typically used), U_∞ is the free-stream velocity, and μ is the dynamic viscosity. The dynamic viscosity needed to calculate Reynolds number is temperature dependent and can be calculated using Sutherland's viscosity law:

$$\mu = \mu_0 \frac{T_0 + S}{T + S} \left(\frac{T}{T_0} \right)^{3/2}. \tag{2.2}$$

where μ_0 is the reference dynamic viscosity at the reference temperature T_0, and S is a constant defined as the Sutherland temperature.

In flows with $Re >> 1$, the inertial forces on the fluid are much larger than the viscous forces. This agrees with an inviscid fluid assumption where the fluids viscous effects are discarded. However, with the introduction of a stationary body (such as an airfoil or a flat plate) and the associated no-slip condition at the wall, the inviscid flow assumption is rendered inappropriate for most cases. The no-slip condition states that the tangential velocity of the fluid flow tends to zero as the solid boundary of a stationary body is approached, which results in a thin region close to the boundary of the body where the tangential velocity of the flow is retarded with respect to the fluid as a whole. This region is called the boundary layer and was initially discovered in 1904 by Ludwig Prandtl.

The boundary layer of a fluid is divided into three separate regions: a steady laminar region, a transition region, and an unsteady turbulent region (Figure 2.1). Approached by a steady flow, a laminar boundary layer initially grows from the forward stagnation point of the body and, as the flow proceeds downstream, there is a point where transition occurs, i.e. a point where the boundary layer becomes

unstable and Tollmien-Schlichting waves start to grow, leading to a turbulent flow. This point is dependent on the local Reynolds number of the flow (defined by replacing L by x in equation 2.14, where x refers to the distance made from the stagnation point) and the surface quality of the body (i.e., its smoothness or roughness). Downstream of this critical Reynolds number, the boundary layer becomes unstable and any small disturbances in the flow results in its progression to turbulent.

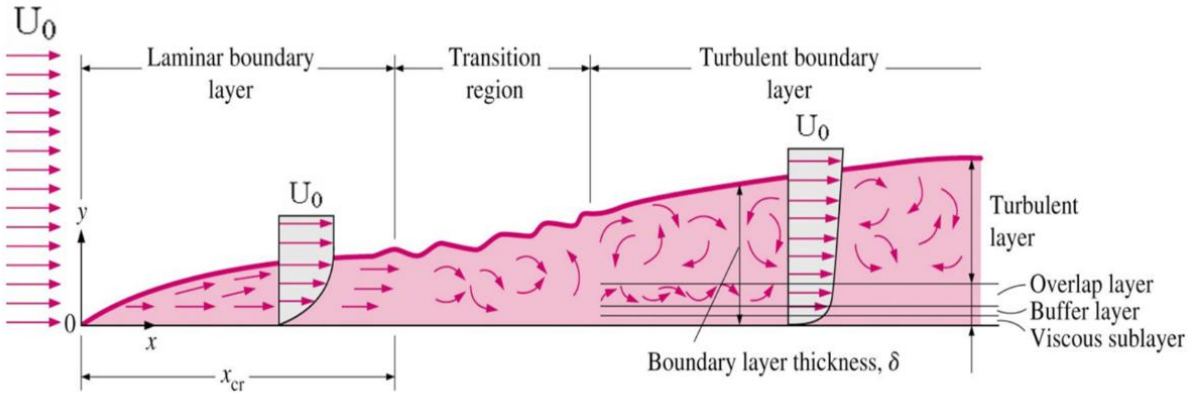

Figure 2.1: Boundary layer over a flat plate [Visavale, accessed May 23rd, 2016].

Chapter 1 introduced unmanned aerial vehicles, and how breakthroughs in miniature electronics and large-scale military backed interests caused research and development of small UAVs to explode over the past few decades. The combination of the characteristically small length scales and low velocities associated with typical UAV configurations and operations results in flight regimes with low wing-chord based Reynolds numbers (i.e., ranging from 1.5×10^4 to 5.0×10^5) that are at the source of the low Reynolds number aerodynamic research field coming into existence as, prior to this, scientific engagement in this regime was infrequent [Mueller and DeLaurier, 2003]. It is now well known that the performance of airfoils designed for chord Reynolds numbers greater than 5.0×10^5 [Lissaman, 1983][Mueller, 1985] deteriorates rapidly as the chord Reynolds number decreases below that value due to laminar boundary-layer separation.

In this flow regime, the boundary layer over an airfoil often remains laminar downstream of the minimum pressure point, separates to form a separated shear layer and, at reasonable Reynolds numbers ($> 5 \times 10^4$), transition occurs. Provided that the adverse pressure gradient is not too large, the flow can recover sufficient energy through entrainment (characteristic of the turbulent flow regime) to eliminate the reverse flow and reattach to the airfoil surface. Thus, on a time-averaged basis, a region of recirculating flow is formed, denominated as a laminar separation bubble (LSB), illustrated in 2.2.

Since LSBs act as a boundary layer trip, i.e. induces flow transition, the phenomena is sometimes referred to as a transitional separation bubble [Brendel and Mueller, 1990]. The flow is unsteady downstream of the maximum vertical displacement of the bubble (maked T in the picture), where transition to turbulent flow is assumed to take place, and steady upstream from it.

The following summarises low Reynolds numbers (LRN) airfoil behaviour [Mueller and DeLaurier, 2003]:

The range $3 \times 10^4 < Re < 7 \times 10^4$ is of great interest to MAV designers as well as model aircraft

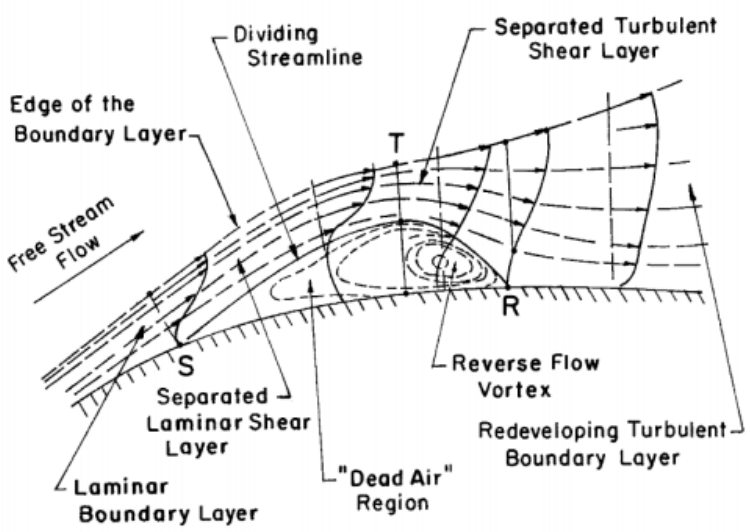

Figure 2.2: Laminar separation bubble [Ananda et al., 2012].

builders. The choice of an airfoil section is very important in this regime because relatively thick airfoils (above a 6% ratio of thickness over chord) can have significant hysteresis in the lift and drag forces caused by laminar separation with transition to turbulent flow. Below chord Reynolds numbers of 5×10^4, the free shear layer after laminar separation normally does not transition to turbulent flow in time to reattach to the airfoil surface. At the low Re numbers, the transitional bubble can occupy up to 40% of the airfoil surface.When this separation point reaches the leading edge, the lift decreases abruptly, the drag increases abruptly, and the airfoil is stalled.

At Reynolds numbers in the range of 7×10^4 to 2×10^5, the laminar separation bubble is ever present. At $Re = 1 \times 10^5$, for instance, the LSB generally extends over 20-30% of the airfoil and significantly changes the pressure distribution by altering the effective shape of the airfoil. Stall occurs when, as the angle of attack is increased, the LSB progressively reaches the trailing edge. For smooth airfoils, extensive laminar flow can be obtained, and therefore airfoil performance tipically undergoes great improvement in this regime. A rough airfoil and turbulent does not exhibit this abrupt performance change with Reynolds number as transition to turbulent flow has already occurred. Many MAVs and small UAVs fly in this range.

For Re above 2×10^5, airfoil performance improves significantly because the parasite drag due to the separation bubble decreases as the LSB shortens. This short bubble represents the transition-forcing mechanism of the flow, and as long as its length is minimized, its effect on airfoil performance is limited. Lift increases linearly with angle of attack until sudden stall occurs. This happens because as the angle of attach increases, the LSB grows and requires a progressively greater pressure recovery for reattachment. Eventually, the short bubble bursts, leading to an abrupt stall behaviour manifested by the drastic deterioration in airfoil performance, due to simultaneous decrease in lift and increase in drag.

This behaviour of the separation bubble is also a factor in the occurrence of hysteresis for some airfoils (Figure 2.3a). When the airfoil stalls due to its LSB bursting, a reduction in the angle of attack does not immediately unburst the bubble, a characteristic that is mainly due to the inherent instability of

the LSB [Maughmer and Selig, 1985].

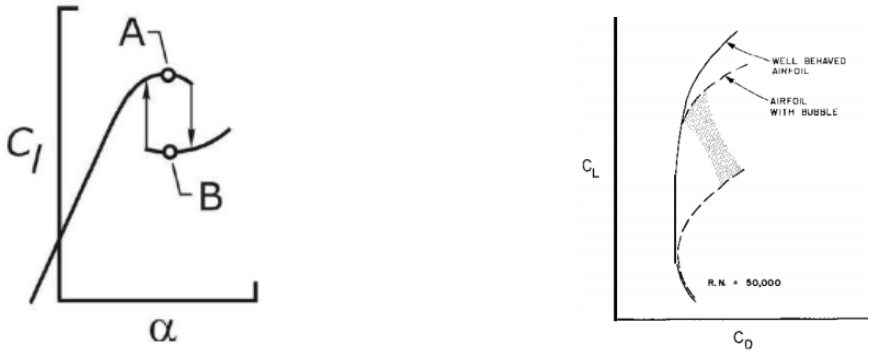

(a) (b)

Figure 2.3: The effects of LSBs: (a) Aerodynamic hysteresis; (b) LSB drag polar, the well-behaved polar is similar to that of conventional airfoils at Reynolds numbers above 10^6 [Lissaman, 1983].

The effects of the laminar separation bubble on airfoil performance are also illustrated in Figure 2.3b airfoil lift-drag polar.

Arguments given so far present the accurate prediction of a separation bubble's existence and extent as a necessary requirement when designing or studying low speed airfoils. However, as in any other flight regime, both the airfoil section and the wing planform of the lifting surfaces are mutually important. The aerodynamics of fixed-wing vehicles is critically dependent on both the Reynolds number and aspect ratio (AR), defined in equation 2.3, of the wing. Furthermore, the performance of finite wings is less than that of airfoils, as they are affected by exclusively three-dimensional flow features [Mueller and DeLaurier, 2003].

$$AR = \frac{b^2}{S} \tag{2.3}$$

where b is the span of the wing, and S is equal to wing's planform area. It can be re-written, for rectangular wings, as:

$$AR = \frac{b}{c} \tag{2.4}$$

where c is the chord of the wing.

The flow around a finite wing at low Reynolds number is characterized by complex three-dimensional flow phenomena as shown in Figure 2.4. The pressure difference between the top (suction side, lower pressure) and bottom surfaces (pressure side, higher pressure) of an airfoil, creates vorticity in the flow with greater intensity at the wingtips. The wake of the vortices trailing behind the wing rolls up into two main vortices, close to the tips. These vortices are of opposite sign (rotation) and deflected downwards, thereby causing the lift vector of the wing to be tipped backwards, producing induced drag.

However, two-dimensional airfoil data still plays an essential role in high AR wings (> 7) , where the local flow behaves approximately two-dimensionally, as illustrated in the center of section of the wing shown in Figure 2.1.

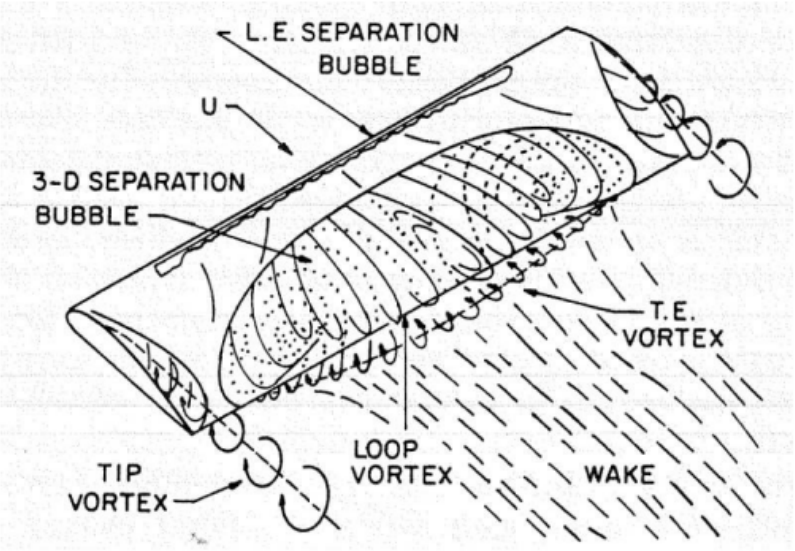

Figure 2.4: Flow over high AR finite wing [Ananda et al., 2012].

In contrast, for low AR wings (< 2), the local airfoil section characteristics cannot be separated from the wing, as these wings process two main sources of lift. The first, linear lift, is derived from the bound vortex flow associated with circulation around the wing. The second, non-linear lift is associated with strong wing-tip vortices that emanate from LAR wings, which induce such strong cross-flow velocities on the upper surface of the wing that further a decrease in pressure.

A word of caution should be offered at the conclusion of this section, regarding published data for this flight regime, which, at first glance, present a "bewildering assortment of inconsistencies", as noted by Lissaman (1983). However, tools have been developed, studies made and context given (the latter, reproduced in these pages) that help explain this behaviour, *"at least in the sense that, for a given performance, we can interpret it [the observation of inconsistencies] as a rational consequence of the boundary layer behaviour in the highly sensitive Reynolds-number domain where transition, separation and reattachment are all occurring on a short length of the airfoil. (...) These issues, relating intimately to the great interconnected puzzle of transition, turbulence, separation, and reattachment, are fundamental to classical fluid mechanics."*

2.2 Computational Fluid Dynamics

2.2.1 The Use of CFD

Over the last few decades Computational Fluid Dynamics (CFD) models solving the RANS equations have become the standard industrial simulation tool for design, analysis, performance determination and investigation of engineering systems involving fluid flows. This development has been driven by the ready availability of robust in-house and commercial CFD software and by the massive increase in affordable computer speed and memory capacity, leading to a steady reduction in the costs of simulations compared to traditional experimental testing [Casey et al., 2000].

Over 40 years ago, Chapman surmised that “computers should begin to supplant wind tunnels in the aerodynamic design and testing process”. He also stated that, eventually, computers would provide a numerical wind tunnel to obtain aerodynamic flow simulations in less time and at lower cost for the design of new aerospace vehicles [Chapman et al., 1975][Agarwal, 1999].

Although this has not yet fully realized, today, CFD tools have a very significant role in the context of a typical aerospace design work-flow, which starts with an initial sizing based on classical analytical or semi-empirical relations, followed by design refinement through CFD, with more accurate performance estimates, identification of potential design flaws and greater insight into overall flow behaviour. CFD can also be used to provide estimated corrections for wind tunnel testing as well as ideal instrumentation placement and functional requirement suggestions to be used during both wind tunnel and flight testing, further down the design cycle. This illustrates how CFD can benefit the aerospace industry.

The review of concepts presented in this entire section can be viewed as a summary of best practice guidelines in CFD present in recent literature. It is mainly (but not solely) based on several documents and workshops produced by the Special Interest Group on ”Quality and Trust in Indutrial CFD” of the European Research Community on Flow, Turbulence and Combustion [Casey et al., 2000][Casey and Wintergerste, 2000] and CD-adapco [Ewing, 2015][CD-adapco][CD-adapco, 2012], developer of the CFD software Star-CCM+, which is used in the computational component of this thesis. Whenever appropriate, the following discussion will be directed specifically to the low Reynolds numbers external aerodynamics application. Some of the nomenclature used may be software specific but, as most CFD packages offer equivalent tools and applications, this should not constitute serious challenge to any reader not particularly familiar to Star-CCM+.

Hirsch [2007] states that there are three fundamental approaches to CFD: the oldest and most traditional Finite Difference Method (FDM), which remains a reference for studies of numerical discretization, but is limited to application in structured grids; the Finite Element Method (FEM), derived from the world of structural mechanics, where it is most widely, applied and; the Finite Volume Method (FVM), by far the most widely used approach to CFD, which discretizes the integral form of the conservation laws directly, granting it greater generality, conceptual simplicity and easy implementation in unstructured grids. This discussion will be focused on the latter.

The computation of steady turbulent flow is one of the most common kind of simulation for the industrial use of CFD software, where solvers attempt to compute solutions for the Navier-Stokes and other conservation equations. However, to simulate turbulence directly by Direct Numerical Simulation (DNS) one needs to be able to capture the time and length scales of all the characteristic structures of the flow, from the energy-carrying large scales to the small dissipative scales. As these vary by several orders of magnitude, a typical spatial scale of 10^{-5} to 10^{-6} of the size of the computational domain in each coordinate direction has to be resolved. For engineering problems this is beyond the capacity of present or foreseeable computers, needing an increase of at least several orders of magnitude in computing power before it can become a general tool. One alternative is to model the turbulent structures, as opposed to actually resolving them.

The Reynolds Averaged Navier-Stokes Model

This was made possible when Osborne Reynolds proposed a new averaging concept for the Navier Stokes equations that significantly reduced the complexity of simulating turbulent flows. The resulting Reynolds Averaged Navier Stokes (RANS) equations are formulated in terms of the time averaged flow fields (velocity, pressure, density and temperature) fields while the average turbulent quantities account for the time-dependence of the turbulent fluctuations. In this sense, the RANS equations represent the temporal average of the fluid flow. Within the RANS concept, all turbulence is modelled, meaning the computer spends effort only on the computation of the mean flow, and no attempt is made to actually resolve existing turbulent structures in time and space.

While today's CFD simulations are based mainly on RANS models, certain classes of flows are better covered by models in which at least a portion of the turbulence spectrum is resolved in the numerical domain. Such methods are termed Scale Resolving Simulation (SRS) models. Large eddy simulation (LES), the first SRS method, in which the large turbulent vortices are captured by the computational grid and the fine-scale turbulent motions are modelled by a so-called sub-grid model, is less intensive in computational resources and closer to engineering applications, relative to DNS, but is is still unlikely to become a common engineering tool, as it has never lived up to the expectations that it could eventually replace RANS models on a grand scale, despite the substantial effort invested into this technology. The main limitation comes from the high resolution requirements for wall bounded flows [Menter, 2011].

It is instructive to compare the numerical effort required for a RANS and LES simulation of the flow over a relatively limited geometry, like a single turbine blade in a gas turbine. Such an estimate is given in Figure 2.5.

	Number of cells	Number of time steps	Number of inner loops per time step	Effort relative to RANS
RANS	$\sim 10^6$	$\sim 10^2$-10^3	1	1
LES	$\sim 10^9$	$\sim 10^5$	1-10	$\sim 10^5$-10^6

Figure 2.5: Estimate of CPU resources for RANS and wall-resolved LES for a single turbine blade [Menter, 2011].

Detached eddy simulation (DES) has been proposed to eliminate the main limitation of LES models by using an hybrid formulation that switches between RANS and LES based on the grid resolution provided. By this formulation, the wall boundary layers are entirely covered by the RANS model and the free-shear flow portions are typically computed in LES mode. In spite of this, for many applications, RANS models are and will remain the optimal choice in terms of a proper balance of accuracy and computational resources. The goal of further improvements is the inclusion of additional effects such as turbulence anisotropy without compromising the current calibration level of the models [Menter, 2011].

The price for the present level of simplification of the RANS models, however, lies in the additional Reynolds stress tensor that appears in the RANS equation as a result of the non-linear terms of the underlying Navier-Stokes equations. These terms are unknown and the equations are therefore not "closed",i.e. there are more unknown variables than equations. The task of RANS turbulence modelling

is to close the RANS system of equations and provide a link between the mean velocity field and the Reynolds stresses.

2.2.2 Turbulence and Transition Modelling

"(Turbulence is) the invention of the devil on the seventh day of creation, when the Good Lord wasn't looking"

Peter Bradshaw

Turbulence modelling is the attempt to develop approximate formulations that, despite our incomplete understanding and limited computational resources, allow engineers to obtain approximate solutions for their pressing technological applications. Also, no single model (or modelling approach) can cover all such applications, and numerous modelling concepts need to be developed, supported by test cases [Menter, 2011].

Most flows of practical interest are turbulent, and turbulent mixing the usually dominates the behaviour of the flow. Turbulence plays a crucial part in the determination of many relevant engineering parameters, such as frictional drag, flow separation, transition from laminar to turbulent flow, thickness of boundary layers, extent of secondary flows and spreading wakes. After a century of intensive theoretical and experimental research, it is now accepted that no single turbulence model can effectively span all its potential applications, hence existing no generally valid universal model of turbulence. At a scientific level, turbulence is one of the great unsolved problems of non-linear computational physics [Casey et al., 2000].

For flows in industrial applications, the effects of turbulence are mostly examined using RANS equations. These are developed from the time dependent three-dimensional Navier-Stokes equations which are averaged in such a manner that the structures of small sizes in space and time are eliminated and become expressed by their mean effects on the flow through the so-called Reynolds (or turbulent) stresses. These stresses must be interpreted in terms of averaged variables in order to close the system of equations. This requires the construction of a mathematical model known as a turbulence model. At this point, several strategies are available, and a full discussion of this subject is outside of this work's scope. However, a brief review with incidence on the most relevant options is presented below in order to introduce a few fundamental concepts.

Turbulence Models

The simplest approach to turbulence modelling rests on the concept of a dynamic turbulent viscosity, μ_t. This relates the turbulent stresses appearing in the RANS equations to the averaged velocity gradients (i.e. the rate of strain), in direct analogy to the classic interpretation of laminar flow by means of the fluid viscosity μ. These are designated as Linear Eddy viscosity models. Unfortunately, unlike its viscous counterpart, the turbulent viscosity is not a function of fluid properties but of the state of turbulence instead. From dimensional considerations, $\frac{\mu_t}{\rho}$ is proportional to $V.L$, where V is a velocity scale and L is a length scale of the larger turbulent motions. Both the velocity scale V and the length scale L are

determined by the state of turbulence and, over the years, various prescriptions for V and L have been proposed, using so-called zero-equation (or algebraic), one-equation and two equation models.

The zero-equation models assume that V and L can be related by algebraic equations to the local properties of the flow. This is the simplest prescription V and L can be given. However, their practical application is based on boundary layer parameters which are not easily computed in a Navier-Stokes based method, and introduce significant additional uncertainty into the computation, as the solutions will be very dependent on implementation details, this being the reason why they are normally not recommended for most RANS applications.

One equation models attempt to improve upon the zero-equation models by using eddy viscosity that no longer depends solely on local flow condutions but also accounts for flow history (i.e. flow path). This is achieved by means of a new transport equation (in addition to the basic mass continuity, momentum and energy, if relevant, transported quantities of the Navier-Stokes equations)that, almost without exception, relates V with the turbulent kinetic energy per unit mass of fluid, k, arising from the turbulent fluctuations in velocity around the averaged velocity. The prescription of L in one-equation models is similar to the algebraic approach, presenting the same limitations. Spalart and Allmaras [1992] devised an alternative formulation for one-equation models specifically for aerodynamic flows, which determines the turbulent viscosity directly from a single transport equation for μ_t, and is proving quite successful for practical turbulent flows in external aerodynamics applications.

For general applications, however, it is more usual to solve two separate transport equations to determine V and L, with two-equation models. To the previously mentioned transport equation for k, an additional transport equation is solved which determines the length scale L. This class of models is the most widely used in industrial applications since is considered to be the simplest level of closure for the RANS equations which to not require geometry or flow dependent input.

The most popular of these (at an industrial level) is the $k-\epsilon$ model, where ϵ is the rate at which turbulent energy is dissipated to smaller eddies [Launder and Spalding, 1974] - the turbulent dissipation rate - as defined by equation 2.5, from whence L is determined from:

$$\epsilon = \frac{C_\mu k^{3/2}}{L} \tag{2.5}$$

,where C_μ is a constant. The second most popular two equation model is the $k-\omega$, where ω is the specific dissipation rate, usually defined by equation 2.6, originally proposed by Wilcox et al. [1998].

$$\omega = \frac{\epsilon}{kC_\mu} \tag{2.6}$$

This model performs very well close to walls in boundary layer flows, particularly under strong adverse pressure gradients (hence its popularity in aerospace applications). However, it is very sensitive to the free stream value of ω and unless great care is taken in setting this value, spurious results can be obtained in both boundary layer flows and free shear flows. The $k-\epsilon$ model is less sensitive to free stream values but is often inadequate in adverse pressure gradients and presents, thereby, a strong tendency to miss or under-predict separation.

The most popular solution to circunvent this problem retains the properties of $k-\omega$ close to the walls and gradually blends into $k-\epsilon$ the model away from the wall, mitigating the free stream sensitivity problem without sacrificing the $k-\omega$ near wall performance. This was the starting point for the baseline (BSL) and, eventually, the $k-\omega$ SST models, as proposed by Menter [1993] and [1994]. These models also attempt to improve performance deterioration of two-equation models when the turbulent structure is no longer close to equilibrium, which occurs when the production of turbulence energy departs significantly from the rate at which it is dissipated at the small scales, usually in boundary layer regions behind shocks or close to separation. In addition, the ω-equation is well suited for combining with the laminar-turbulent transition modelling [Menter, 2011].

The relative performances of the previously introduced linear eddy viscosity models were studied in NASA [Bardina et al., 1997], comparing predictions with experimental data. Tests to determine the numerical performance of the models included studies of grid refinement and sensitivity to initial and boundary conditions, free-stream turbulence, and numerical codes. The models were ranked with the $k-\omega$ SST model as the best overall model, followed by the Spalart-Allmaras model, then the $k-\epsilon$ model, and finally the $k-\omega$ model. The SST model was considered the best model because it did the best overall job in predicting the complex flows involving separation while giving results comparable with the best of the other models for simple flows.

This concludes the review for Linear Eddy Viscosity models. Alternatives to them are the: Reynolds stress transport models (RSTM), or second closure models (SMC), which dispense the notion of turbulent viscosity and determine the turbulent stresses directly by solving a transport equation for each stress component, requiring the solution of six additional coupled equations, sometimes interpreted as second moments of the momentum equations, together with an equation for ϵ to provide a length scale, which makes this model complex and expensive to compute but more apt to deal with flows with strong swirl or streamline curvature (Figure 2.6); and non-linear eddy viscosity models (NLEVM) which retain the underlying idea that the turbulent stresses can be algebraically related to the rate of strain (i.e. time averaged velocity gradients), but use higher order quadratic and cubic terms which feature additional coefficients which can then be used for more detailed calibration with experimental data. To the author's knowledge, the latter is not yet as well established as LEVM, but is gaining popularity as it may only require the same number of equations as two-equation models (and thus are computationally efficient) and provide improved results in flow impingement/reattachment areas where linear methods mostly fail [Casey et al., 2000].

Transition Models

The term "transition" refers to the phenomenon of laminar to turbulence transition in boundary layers. The location of the onset and extent of transition is of major importance in the design and performance of most aircraft as it can have a strong influence on wall shear stresses and separation behaviour of boundary layers.

Three primary modes of transition can typically occur:

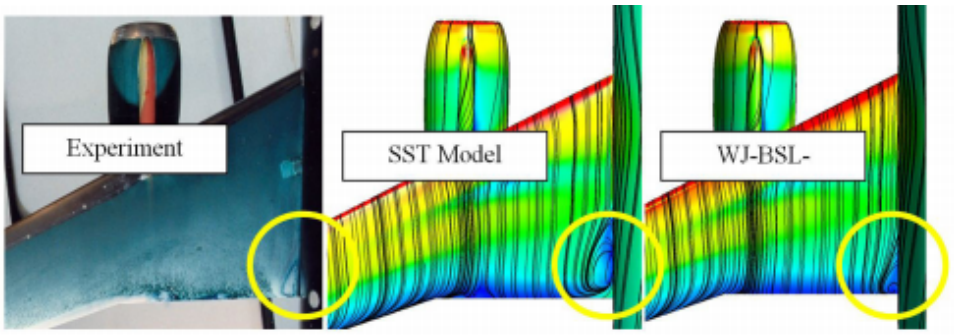

Figure 2.6: Oil Flow Visualization vs SST vs an RSM model. Improved predictions of the size of the corner separation bubble can be observed [Menter, 2011].

- Natural transition, in which a laminar boundary layer subjected to weak disturbances becomes linearly unstable beyond a critical Reynolds number at which Tollmien-Schlichting waves start to grow;
- Bypass transition, the process of transition in response to large disturbances outside the boundary layer. This can occur when an airfoil encounters the wake from an upstream device. Examples of bypass transition that can occur in flight are on the tail surfaces located in the wake of a fuselage, or on flaps of a multi-element airfoil;
- Separation induced transition, in which separation of the laminar boundary layer induces transition. The laminar boundary layer often reattaches in response to the enhanced mixing caused by the turbulent flow, forming laminar separation bubble upstream of the transition location.

While many industrial flows are in the range of $10^4 < Re < 10^6$, i.e. in regimes where significant portions of the boundary layers can be laminar, for many decades, modelling of laminar-turbulent transition in boundary layers was proven one of the most challenging tasks in CFD [Menter, 2011].

A transition model is a model that can be combined with a turbulence model in order to predict the onset of transition in a turbulent boundary layer. Transition models are necessary because turbulence models themselves cannot be relied upon to predict the onset of transition. There are several methods to account for transition in computational simulations, namely: the turbulence suppression model; the e^N method, and; the semi-empirical local correlation-based transition models (LCTM).

The turbulence suppression model does not really predict transition. Instead, it allows the user to mimic the effect of transition by suppressing the turbulence in a certain prescribed region region. This may be practical if accurate transition location measurements have been previously performed.

The e^N method is based on local, linear stability theory and parallel flow assumptions, in order to calculate the growth of the disturbance amplitude from the boundary layer neutral point to the transition location. A benefit of using the e^N method is related to the fact that it has a well-anchored theoretical basis and good agreement to experimental data of natural transition. The software X-Foil [Drela, 1989] uses an e^N method for transition prediction and is widely regarded as one of the best tools available for predicting transition on airfoils for low speed flows. This model may, for example, be used to estimate the transition location prescription for the previous turbulence suppression method.

However, there remain some formidable barriers towards applying the e^N method to general aerospace applications. The first is that since the e^N method is based on linear stability theory it cannot predict transition due to non-linear effects such as high free-stream turbulence or surface roughness. Secondly, there is no record in the open literature where the e^N method has been successfully applied to predict transition on a full 3-dimensional aircraft configuration [Langtry and Menter, 2005].

Semi-empirical local correlation-based transition models (LCTM) make use of experimental correlations which usually relate the free-stream turbulence intensity, Tu or I, defined according to equation 2.7 (sometimes presented as a percentage), and the local pressure gradient to the transition momentum thickness Reynolds number.

$$Tu = \frac{u'}{U_\infty} \tag{2.7}$$

, where u' is the root-mean-square of the turbulent velocity fluctuations and U_∞ is the mean free stream velocity .

The downside is that these methods are not as well theoretically anchored as the e^N method. Also, for classical correlation-based transition models, it is necessary to compare the actual momentum-thickness Reynolds numbers to the transition value from the correlation. This is not an easy task in a Navier-Stokes environment because the boundary layer edge is not well defined and the integration will therefore depend on the implementation of a search algorithm. These difficulties are exacerbated by modern CFD methods that are based on unstructured grids and massive parallel execution. Unstructured grids do not easily provide the infrastructure needed to integrate global boundary layer parameters because the grid lines normal to the surface cannot be easily identified. In the case of a general paralleled CFD code, the boundary layer can be split between different CPUs making the integration procedure tedious to perform in parallel. The use of classical correlation-based transition criteria is therefore incompatible with modern CFD codes.

However, the $\gamma - Re_\theta$ Transition model [Menter et al., 2006] [Langtry et al., 2006], a correlation-based model coupled with the $k - \omega$ SST model, provides true transition predictive capabilities and because it is based on two new transport equations using only local information - one for intermittency, which can be used to trigger transition locally, and a second which is solved for the transition onset momentum-thickness Reynolds number, tying the empirical correlation to the onset criteria in the first intermittency equation - it is fully compatible with modern unstructured, parallel CFD codes and aeronautical flow applications.

The computational costs of this model are significantly higher than fully turbulent calculations for two reasons. First, requirements on mesh resolution are greater (both wall-normal and streamwise spacing). Second, apart from the overhead of solving two additional transport equations, the interaction between the momentum, turbulence and transition equations requires more iterations for convergence. In addition, much more attention needs to be paid to the inflow or free-stream turbulence boundary conditions. To facilitate a better match with the turbulence intensity profiles, the turbulence decay implicit to the turbulence model formulation is typically deactivated, so that the inlet values are, in effect, leading

edge values, which can then be specified in terms of turbulence intensity and turbulent viscosity ratio (TVR), defined by equation 2.8 [Malan et al., 2009] [Langtry and Menter, 2005].

$$TVR = \frac{\mu_t}{\mu} \tag{2.8}$$

These relate to the former quantities via equations 2.9 and 2.10 and are more practical to prescribe, as experimental turbulence conditions are more often reported with these values.

$$Tu = \frac{\sqrt{(2/3)k}}{U_\infty} \tag{2.9}$$

$$TVR = \frac{k}{\omega\mu} \tag{2.10}$$

2.2.3 Meshing and Near Wall Treatment

Meshing

The computational grid, or mesh, represents the geometry of the region of interest. The computational domain needs to be discretized using grid cells that should provide an adequate resolution of the geometrical and expected flow features. Several types of grids exist for CFD, and their categorization in the literature is not entirely consistent throughout (compare Casey et al. [2000], Agarwal [1999] and [Hirsch, 2007]). However, for the intended purposes, the most fundamental classifications refer to: the approach to capturing both geometrical and (expected) flow features; grid topology, and; cell type. Details on each of these classes are outside of this work's scope, and only a brief review of this topic is presented below.

Two main approaches exist to capture the geometrical and flow pattern related details of the domain:

- In regular grids (Figure 2.7a), grid lines inside a rectangle (2-D)or rectangular box (3D) are aligned with a Cartesian coordinate system, allowing for a simpler implementation of the discretized fluid flow equations. For this reason, they are sometimes designated as Cartesian grids. Cells intersecting curved domain surfaces (such as the body's geometry) can be either removed, defining the boundary by sequence of steps and keeping the regular shape of the cells most close to the surface, or cut, defining the boundary by sequence of flat facets, with at least two points at the geometric surface of interest, for which case cells near the wall acquire an irregular shape;

- In body-fitted grids (Figure 2.7b), grid lines the follow curved domain surfaces and cells are design in order to keep a regular shape.

Regarding topology, grids can be:

- Structured (Figure 2.8a),for which connectivity between cells is pre-ordained, with cells adjacent to one another given consecutive indices, explicitly defining their position relative to one another, face-to-face, inside the computational domain. Cell edges form continuous mesh lines which start and end on opposite computational domain sides;

(a) (b)

Figure 2.7: (a) Regular grid; (b) Body fitted grid [Agarwal, 1999].

- Unstructured (Figure 2.8b), which are assembled freely (or arbitrarily), cell by cell. In these grids, connectivity information between cells, not having been specified à priori, must be stored in a table upon conclusion of the mesh generation process.

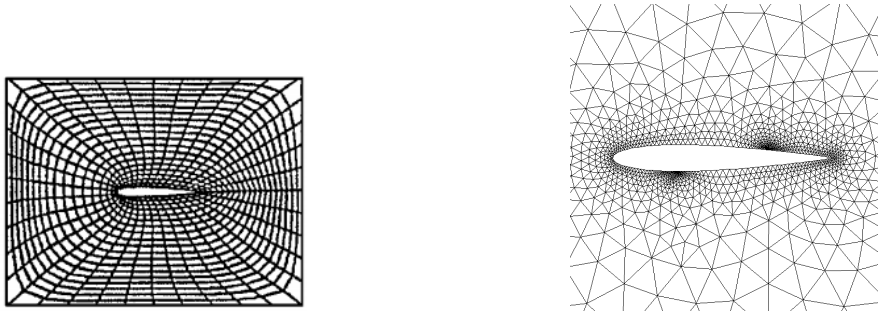

(a) (b)

Figure 2.8: (a) Structured Grid [Agarwal, 1999]; (b) Unstructured grid [Muller, accessed May 23rd, 2016].

Applicable cell types depend on mesh topology. Cells in structured meshes have an hexahedral shape and cells in unstructured meshes are typically of tetrahedral, hexahedral, polyhedral or prismatic shape. Unstructured grids may yet be split into:

- Bock Structured Grids (Figure 2.9a) - the mesh is assembled from a number of structured blocks attached to each other. Attachments may be regular (cell faces of adjacent blocks match), or arbitrary (general attachment without matching cell faces);
- Chimera Grids (Figure 2.9b) - structured mesh blocks are placed freely in the domain to fit the geometrical boundaries and to satisfy resolution requirements. Blocks may overlap and, instead of attachments at block boundaries, information between different blocks is transferred in the overlapping region;
- Hybrid Grids (Figure 2.9c) - these grids combine different cell types for greater flexibility, efficiency and better resolution in critical areas.

Grids must be fine enough to provide an adequate resolution of the important flow features, as well as geometrical features. This may be achieved by local grid refinement, either manually or automatically. Unstructured meshes are especially suited for this purpose. Most modern commercial meshing

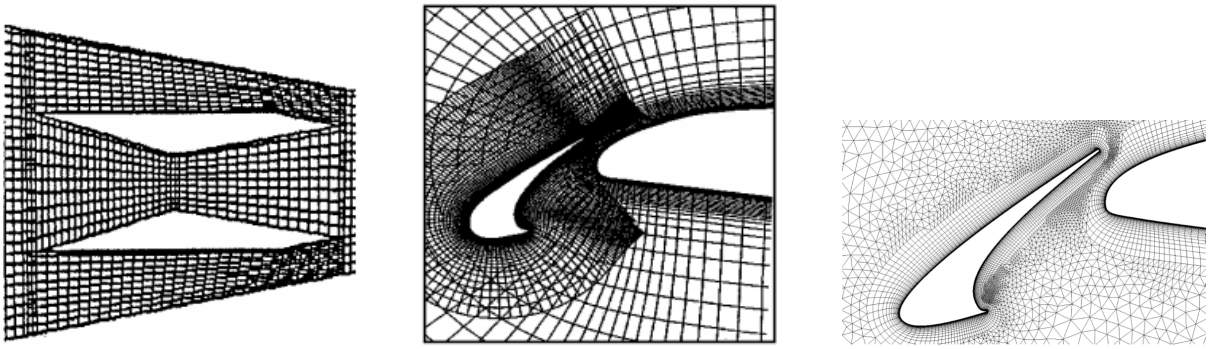

(a) (b) (c)

Figure 2.9: (a) Bock Structured Grid (b) and Chimera Grid [Agarwal, 1999]; (c) Hybrid Grid, with prismatic layers [Linkoping University, accessed May 23rd, 2016].

CFD tools are unstructured meshers, as unstructured grids have progressively become the dominating approach to industrial CFD [Hirsch, 2007]. So much so, that sometimes even when structured mesh generation is available in a particular CFD package, the included solvers may not be suited to take advantage from it, as is the case with Star-CCM+, equipped exclusively with unstructured solvers.

One of the advantages of unstructured grids is the possibility to perform local refinements in a certain region, without affecting the grid point distribution outside that region. This opens the way for flexible grid adaptation by local refinement or local coarsening Some CFD codes provide algorithms to adapt the grid resolution locally according to numerical criteria from the flow solution, based on information such as flow gradients or error estimators, efficiently placing more cells where they are most needed, in order to increase the accuracy in regions of strong flow variations, and reducing grid resolution in regions of little interest, impact on results or where the solution has already reached an acceptable accuracy. Grid adaptation is generally carried out by redistribution of grid points (achieved by moving grid points), refinement (achieved by adding or deleting grid points), or a combination of the two. Redistribution has been the favoured approach with structured grids and refinement is typically used with unstructured grids. The entire process has the ultimate goal of optimizing the number of grid points for a certain level of accuracy. Figure 2.10 illustrates this concept.

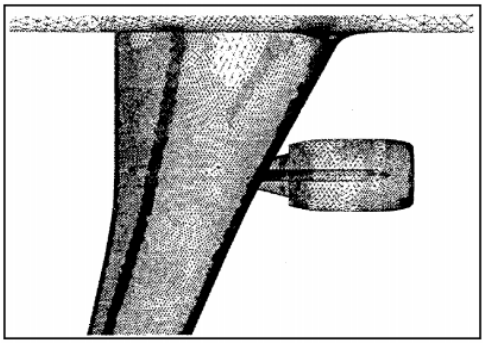

Figure 2.10: Unstructured mesh with local refinement (from grid adaptation) in order to properly capture shocks [Agarwal, 1999].

The accuracy of the simulation usually increases with increasing number of cells, i.e. with decreasing cell size. However, due to limitations imposed by the computer storage and run-time, some compromise

in mesh size is always nearly inevitable. In addition to grid density, the quality of a mesh depends on various criteria such as the shape of the cells. Cell aspect ratios, skewness and warp angles are all metrics of cell quality, and cell growth rates inside the grid are also of great importance.

One exception to general aspect ratio quality requirements concerns grid cells near walls, where typical restrictions may be relaxed and indeed it can be beneficial to have high aspect ratio cells inside the boundary layers. Unstructured meshing techniques take advantage of high aspect ratio prismatic layers (or prism layers) close to domain boundaries of interest (Figure 2.9).

Near Wall Treatment

In boundary layers, the normal gradients in some flow variables become large as the distance to the wall reduces to zero. A large number of mesh points placed close to the wall is required to resolve these gradients. Furthermore, as the wall is approached, turbulent fluctuations are suppressed and eventually viscous effects become important in the region known as the viscous sub-layer. This modified turbulence structure means that many standard turbulence models are not valid all the way through the wall. Thus special modelling procedures are required. There are typically two ways to approach this problem: with, or without wall functions. A quick explanation of both strategies is given below.

The use of wall functions is the most frequent industrial practice. The difficult near-wall region is not explicitly resolved but is bridged using so-called wall functions. In summation, this procedure is based on the assumption that the dimensionless velocity profile of U^+ (defined in equation 2.11) as function of the dimensionless wall distance y^+ (defined in equation 2.13) has an universal behaviour up to some limiting value of y^+ (Figure 2.11a).

$$U^+ = \frac{U_\infty}{u_\tau} \tag{2.11}$$

where the wall friction velocity u_τ is,

$$u_\tau = \sqrt{\frac{\tau_w}{\rho}} \tag{2.12}$$

$$y^+ = \frac{y \rho u_\tau}{\mu} \tag{2.13}$$

This is indeed observed in practice, with a linear relationship between U^+ and y^+ in the viscous sub-layer, and a logarithmic relationship, known as the law of the wall, in the layers adjacent to this, thus designated the log-layer. The y^+ limit of validity depends on external factors such as the pressure gradient and the penetration of far field influences.

These universal functions can be used to relate flow variables at the first computational point, at some distance y from the wall, directly to the wall shear stress without explicitly resolving the structure in between. The constraints to be observed are:

- The calculated flow must be consistent or nearly consistent with the assumptions made in arriving at the wall function equations, i.e. an attached two dimensional Couette flow with small pressure gradients, local equilibrium of turbulence and a constant near-wall stress layer (Figure 2.12);

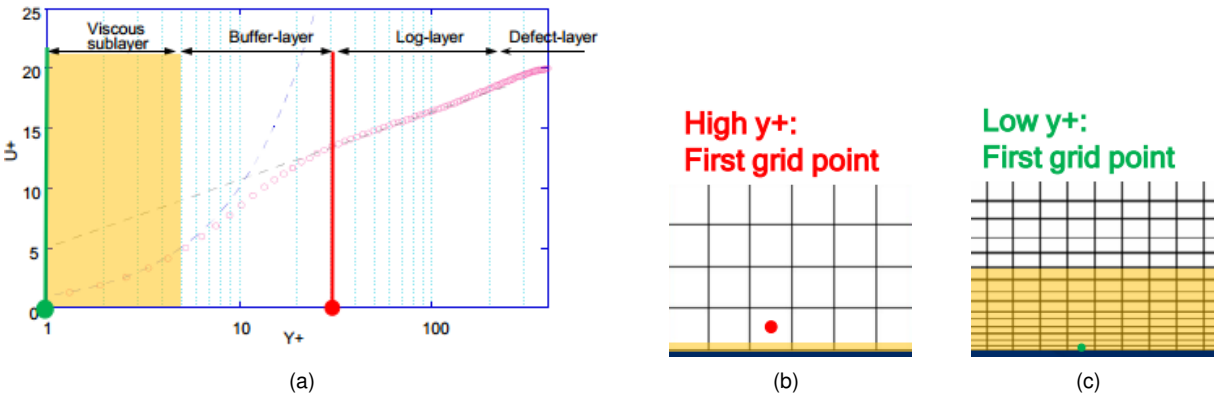

(a) (b) (c)

Figure 2.11: (a) Adimensional velocity boundary layer profile for a flat plate for a null pressure gradient; (b) High y+ first grid point; (c) Low y+ first grid point [Ewing, 2015].

- The value of y^+ at the first mesh point must remain within the validity limits of the wall function, both minimum and maximum, usually from 20 or 30 and up to 300, respectively.

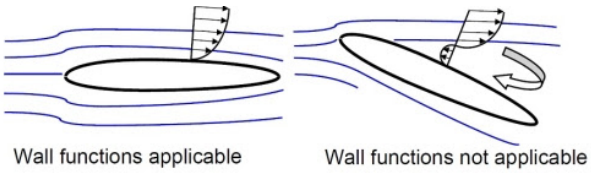

Figure 2.12: Applicability of wall functions [LEAP CFD Team, accessed May 23rd, 2016]

This means that, when studying attached flow, generally a wall function approach can be used, allowing for larger initial y^+ value - thus designating the adequate mesh and models as high y^+ (Figure 2.11b)- and smaller overall mesh cell count and faster run times. However, if highly 3-dimensional flow behaviour or flow separation is expected, and the accurate prediction of the separation point may have an impact target results, then the boundary layer should be resolved all the way to the wall with a finer mesh.

Additionally, it is important to reiterate that the purpose of wall functions is to bridge the extremely thin viscous layer near the surface. They do not free the CFD user from the need to adequately resolve the turbulent portion of the boundary layer if accurate prediction of boundary layer effects such as wall friction are intended. For low Reynolds number boundary layers, which may have an upper limit of as little as 100 y^+ units, it is difficult simultaneously satisfy the requirements that the first integration point be placed outside the viscous sublayer and that sufficient boundary layer resolution should be used.

The previous statements alert to the necessity of low Reynolds number models compatible with higher near-wall resolution and capable of explicitly resolve throughout the entire boundary layer – i.e. low y^+ or low Reynolds numbers grids and models (Figure 2.11c).

If fully turbulent flow is assumed, a low y^+ model typically requires a first grid cell in the $1 < y^+ < 5$ range, at least ten grid points below a y+ value of 30 in order to properly resolve the viscous sublayer, and a total of 24 to 32 points inside the boundary layer for adequate resolution [Ewing, 2015].

However, it is clear from validation studies that when the $\gamma - Re_\theta$ transition model is used, higher-

quality low Reynolds number grids are required. In these cases, the wall-normal mesh spacing should be fine enough that $0.1 < y^+ < 1$ and special attention should be paid to the streamwise mesh spacing near the transition region. If transition is induced by laminar separation, then the mesh should be fine enough to resolve the curvature of the body where the separation exists, and to capture the laminar separation bubble.

2.2.4 Errors, Uncertainties, Validation and Verification

CFD makes use of computer simulation to obtain an approximate solution to the governing equations of fluid flow. The solution is always approximate because only discretized versions of the continuum transport equations for fluid flow and energy transfer can be solved numerically. Moreover, in turbulent flows, the effects of turbulence cannot be represented in a mathematically accurate sense, but are modelled by approximate theories. Because it is not exact, CFD is used together with more traditional techniques such as flow measurement or analytical methods, for the investigation of fluid flows.

Engineering flows are generally analysed with a view to identifying weak features of a design so that a component may be improved in functionality. In this sense, even an inaccurate simulation can be of use to engineering design, provided that the error bounds on the predicted parameter are acceptable.

In the absence of quantitative accuracy the engineer often tends to examine the predicted flow field in qualitative terms to access global flow structures ad trends (e.g. the presence and extent of flow separations). The details of the complex flow-fields provided by CFD, even when not perfectly accurate, are in this way an important source of insight into design improvements and also into the design of experiments and the most appropriate location of any instrumentation.

Despite this, it is still very important to be aware of all factors limiting the accuracy of the simulations, i.e sources of uncertainty and error, as well as the recommended procedures for validation of results. These definitions are based on those from Committee et al. [1998] and Roache [1997], as compiled by Casey et al. [2000].

Errors and Uncertainties

Error in CFD is defined as recognizable deficiency that is not due to lack of knowledge. Uncertainty in CFD is defined as a potential deficiency that is due to lack of knowledge.

Typical known errors are the round-off errors in a digital computer and the convergence error in an iterative numerical scheme. In these cases, the CFD analyst has a reasonable chance of estimating the likely magnitude of the error. Unacknowledged errors include mistakes and blunders, either in the input data or in the implementation of the code itself, and there are no methods to estimate their magnitude.

Discretization errors arise due to the difference between the exact solution of the modeled equations and the numerical approximate solution, with a limited resolution in time (if transient) and space. Discretization is probably the most crucial source of error for the accuracy of numerical fluid flow simulations and needs to be carefully analysed.

In principle, the solution of a well converged simulation is independent of the numerical method and

the solution algorithm chosen, provided the grid is fine enough. Convergence errors occur due to the difference between a fully converged solution on a finite number of grid points and a solution that is not fully converged. The equations solved by CFD methods are usually iterative, and starting from an initial approximation to the flow solution, iterate to a final result. This should ideally satisfy the imposed boundary conditions and the equations in each grid cell and globally over the whole domain, but if the iterative process is incomplete then errors arise. In short, convergence errors arise when not enough time is provided for a converged solution to be reached, or if the numerical methods are inadequate and do not allow the solution algorithm to complete its progress to the final converged solution.

There is no convergence theory for the solution of the discrete RANS equations. Hence convergence cannot be enforced by theoretical means, but is based on empirical criteria. Driving all the residuals in all equations plus the residuals of the integral balances down to machine accuracy is the most generally accepted convergence criterion. Residuals are 3D fields associated with a conservation law, such as conservation of mass or momentum. They indicate how far the present approximate solution is away from the exact cancellation of flux balances in each cell. In principle, a solution is converged if the level of round-off error is reached. This level of convergence is an ideal that, for practical reasons related to time constraints, is not used for most engineering computations.

Instead, some methods measure the normalised change in variable values between successive iterations, or on values of globally integrated parameters, such as the lift or drag coefficients, or at the value of a physical quantity at a specific point of the flow domain. The second option, judging convergence according to the stabilization of the lift and drag coefficients is of particular relevance for aerospace applications.

However, in some situations, the iterative procedure will not converge, but either diverges or remains at a fixed and unacceptable level of error, or oscillates between alternative solutions. Careful selection and optimization of advanced/expert control parameters of the solution algorithm (such as damping factors, relaxation factors) may be needed in these cases to ensure that a converged solution can be found wherever possible. A procedure which proved successful for one class of problems may not be successful for a different problem.

Round-off errors are due to the fact that the difference between two values of a parameter is below the machine accuracy of the computer. This is caused by the limited number of computer digits available for storage of a given physical value.

Errors can also occur due to bugs in the software, unintended programming errors in the implementation of models or compiler errors on the computer hardware being used. Such errors are often difficult to find, as CFD software is highly complex, typically involving hundreds of thousands of lines of code for a commercial product. Computers are very unforgiving. Even a relatively simple typing error that might easily be overlooked can have disastrous consequences when incorporated into a line of code.

Many errors also arise from mistakes and carelessness of the user. Such errors generally decrease with increasing experience of the user, but in the nature of things cannot be completely eliminated as ”to err is human”. This error is often described by the popular jibe ”garbage in, garbage out”. Sometimes, however, garbage in does not lead to (terrible) garbage out because a genuine user error does not

always have a significant effect on the results.

Several factors may give rise to user errors, such as the too optimistic and uncritical use of CFD due to its high accessibility through simple interactive graphical user interfaces in commercial software and the seductive power of the colourful visualizations - having for this reason been occasionally referred to as ”Colorful Fluid Dynamics”. However, unlike linear finite element stress analysis, CFD still requires expertly trained users for good results.

Uncertainties arise because of incomplete knowledge of a physical characteristic, such as the turbulence structure at the inlet to a flow domain or because there is uncertainty in the validity of a particular flow model being used.

Model uncertainties are due to the difference between the real flow and the exact solution of the model equations. This includes errors due to the fact that the exact governing flow equations are not solved but are replaced with a simplified model of reality. The most well-publicised errors in this category are the errors from turbulence modelling, but other model errors may occur. Examples would be the simplification of an equation of state of a real gas to that of an ideal gas and the assumption of incompressible flow when compressibility effects may occur. In short, the model errors and uncertainties can be described as the uncertainties which arise because we are in fact solving the wrong equations.

Inaccuracy is also introduced because the application is complex and precise data needed for the simulation is not always available. These are application uncertainties. Examples of this are uncertainties in the precise geometry (e.g. due to design modifications), data (e.g. physical properties of the flow) or model (e.g. symmetry of the flow) that needs to be specified as boundary conditions (such as turbulence properties at an inlet), and uncertainties as to whether the flow is likely to be steady or unsteady.

Since there is little doubt that CFD on the basis of the RANS equations with a suitable turbulence model will continue to form the basis of most engineering calculations for many years to come, a way to deal with uncertainty in CFD simulations is needed. One approach to this problem is to establish an agreed list of best procedures and best practice to ensure that the results of a CFD simulation are as accurate and credible as possible [Casey and Wintergerste, 2000]. Examples of such initiatives are given by Mendenhall et al. [2006] and Casey et al. [2000].

Verification and Validation (V&V)

Verification in CFD is the procedure to ensure that the program solves the equations correctly or, in other words, the procedure to access if the code “solving the equations right”. It provides a means of checking that the code faithfully reproduces the model approximations incorporated in the algorithms. The main problem with verification is that the accuracy of a code can never be formally demonstrated for all possible conditions and applications, and for all possible combinations of valid input. It is the responsibility of the code developer to perform its verification.

Validation in CFD is the procedure to test the extent to which the model accurately represents reality or, in other words, if the simulation is “solving the right equations”. It is undertaken by systematic comparison of CFD results to reliable and appropriate experimental data or algebraic solutions, when

available, in a highly time-consuming process, as it requires a careful selection of suitable experimental data, assessment of its accuracy, careful and systematic simulation of the test case and analysis of the results. One of the limitations to small UAV computational analysis is the lack of accurate, comprehensive data for validation [Viken et al., 2014].

Another important definition, often forgotten or misused in the literature, is relative to the concept of calibration, the procedure to access the ability of a CFD code to predict global quantities of interest for specific geometries of engineering design interest. The author interprets the practical difference between validation and calibration as an issue of scope, meaning that calibration refers to a more focused assessment to specific applications.

However, in many industrial engineering cases, the distinction between them becomes blurred. Ironically, the present document is not an exception. This reflects the most frequent use of the term: calibration as the procedure of adjusting the values of the coefficients of a turbulence model to provide better agreement with the experimental data or, in other words, the process of fine tuning advanced/expert specifications of the modelling tools in order to achieve better correlation with results from other sources.

2.2.5 Sensitivity Tests and Grid Independence

The objective of a sensitivity test is to allow the examination of the effect of variations of any particular parameter in the simulation on the predictions.

In a first instance, this technique can be used to examine the predicted flow over a range of certain flow parameters and boundary conditions whose exact value may be ill-defined, such as the turbulence level at the inlet to the flow domain. Instead of changing parameters arbitrarily, the selection of relevant studies should be based on experience with the fluid dynamics of the case under consideration.

In addition, such sensitivity analysis can be carried out to examine the effect of grid types and mesh sizes. A major issue in CFD simulations is the accuracy of the numerical discretization on grids that are not good enough to produce grid independent solutions, especially for complex geometries in many industrial applications, due to practical constraints on memory capacity and computer power. Not checking for grid independence is a common cause of erroneous results in CFD [LEAP CFD Team, accessed May 23rd, 2016].

This has led to extensive discussion of the credibility of many CFD simulations. These difficulties are amply demonstrated by the many CFD validation exercises involving blind test cases, where ony sufficient information is made available to the participants to allow a CFD model to be set up and run, but the full test results are not available. The results of such exercises have been shown to be highly user-dependent, even when the same CFD software with the same models is being used [Casey and Wintergerste, 2000].

Various procedures for uncertainty estimation in CFD in present literature are based on grid refinement studies. Examples of such strategies are the Richardson extrapolation (RE) and the well known Grid Convergence Index (GCI) introduced by Roache [1997], with at least 5 or at least 3 successive grid refinements being required for each criteria, respectively.

Ideally, each different configuration and each observation of the results require an apropriate means of validation if test results are to have any scientific meaning, which can be a very time-consuming process and in complex cases they may be limited in scope. For this reason, these efforts should always be documented as it may be considered satisfactory to carry out sensitivity tests not for each specific application, but for similar classes of applications requiring the use of the same models and the same general settings. This is particularly relevant in engineering applications, and especially during conceptual and design stages of a new project (be it whole aircraft or single components). In these cases, a great number of design iterations simultaneously under consideration and valuable practical conclusions can be made even from preliminary simulations.

2.3 Wind Tunnel Testing

2.3.1 Background and Basic Principles

"The wind tunnel is indispensable to the development of modern aircraft. Today no aeronautical engineer would contemplate committing an advanced aircraft design to flight without first measuring its lift and drag properties and its stability and controllability in a wind tunnel. Tunnel tests first, free-flight tests later, is the proper order of things."

Donald D. Baals and **William R. Corliss** in "Wind Tunnels of NASA", 1981

However, as evident as the utility of wind tunnels is today, it was actually not the first aerodynamic testing device.

The first aerodynamicists recognized, as Leonardo da Vinci and Isaac Newton had before them, that they could either move their test model through the air at the required velocity or they could blow the air past a stationary model – an obvious interpretation of the principle of relativity and a fundamental concept to wind tunnel testing.

Early experiments were conducted on open air, with test models mounted above windswept ridges and in the mouths of blowing caves, until being forced to develop diverse mechanical schemes that provided more steady and controllable flow conditions. The simplest and cheapest contrivance moved models at high speeds with a whirling arm, a mechanism analogous to an aeronautical centrifuge. Benjamin Robins, a brilliant English mathematician, was the first to employ this strategy, in the first half of the 18th century. The arm tip of his apparatus merely reached a few feet per second. However, these machines evolved and, by the end of the 19th century, the whirling arm had provided most of the systematic aerodynamic data collected.

Its flaws, however, did not go unnoticed. Test results were adversely influenced as the arm's movement set all the air in its vicinity into rotary motion, and test models on the end of an arm would effectively fly into their own wakes. With so much turbulence, the true relative velocity between the model and the air could not be successfully determined and, furthermore, it was extremely complicated to mount instruments and measure the small forces exerted on the test articles when they were simultaneously spinning at high speeds. Something better was needed.

That something better was the wind tunnel. Frank H. Wenham, a Council Member of the Aeronautical Society of Great Britain, is generally credited with designing and operating the first wind tunnel in 1871, over 30 years before the first successful powered flight by the Wright brothers. Wenham had tried a whirling arm, but his unhappy experiences impelled him to urge the Council to raise funds to build a wind tunnel, which operated by means of a fan-blower upstream of the model, driven by a steam engine, propelled air down the tube, *"a trunk 12 feet long and 18 inches square, to direct the current horizontally, and in parallel course"* (his words), to the model.

Although a myriad of different types of wind tunnels currently exist, this device, in its most elementary representation, consists of an enclosed passage through which air is driven by a fan or any appropriate drive system, the heart of which is the test section, in which a model is supported in a carefully controlled airstream, which produces a flow of air about the model, duplicating that of "free-flight". At this point, it is necessary to introduce the principle of flow similarity, another fundamental concept to wind tunnel testing.

Due to diverse practical constraints, mainly financial and spatial in origin, the great majority of wind tunnel facilities do not allow for full-scale models of most typical configurations and sizes to be tested. Instead, smaller scale models are placed in the test section to be experimented on. This requires for a specific set of criteria to be respected, in order to warrant an accurate representation of the flow phenomena experienced during real flight conditions to be observed under test conditions, i.e., flow similarity.

The parameters for flow similarity are dimensionless coefficients that appear in the non-dimensional forms of the equations for fluid flow, namely: the Reynolds number, the Mach number, and the Froude number. A mathematical derivation for these parameters is given by Barlow et al. [1999], which is also the source of the simplified explanation presented below and the main reference to the remainder of this section.

When a body moves through a fluid, forces arise that are due to its viscosity, elasticity and gravity. These forces are represented directly by the various terms in the Navier-Stokes equations, briefly discussed in section 2.2. The Reynolds number, originally introduced, in section 2.1, represents the ratio between the inertial and viscous forces acting on the fluid, whereas the newly introduced parameters Mach number and Froude number are equivalent to the ratio between the inertial and elastic forces, and the square root of the ratio between the inertial and gravity forces, respectively.

However, these parameters are not equally relevant nor simultaneously attainable in every experiment and choices must be made based on which parameter is known to be most important for the flow situation under consideration. For example, the Froude number is an important similarity parameter only for dynamic tests where model motion as well as the aerodynamic forces are involved. It can therefore be neglected during the course of stationary wind tunnel tests. The two remaining parameters, the Mach and Reynolds numbers, cannot be matched simultaneously for a scaled model. In fact, it is frequently the case that neither Reynolds nor Mach numbers can be fully matched. However, the Mach number can be considered as a measure of the compressibility of a flow in external aerodynamics studies, and becomes relevant only when significant compressible flow conditions are expected, typically for Mach

numbers above 0.3.

This leads to the conclusion that, for stationary low-speed tests (to which the present work is limited), matching Froude and Mach numbers is not critical, and efforts should be directed towards matching the Reynolds number, whose effects are predominant.

2.3.2 Testing Facilities, Measurements and Models

The basic function of a wind tunnel is, for the purposes intended, to accelerate flow of density ρ and dynamic viscosity μ up to a speed U_∞, while conducting it towards a test section where a test article (or model) of characteristic length L is placed. It is intended that the Reynolds number (repeated below for convenience) between the test and the actual free-flight conditions match.

$$Re = \frac{\rho U_\infty L}{\mu} \tag{2.14}$$

Ergo, when a scale model is used and the reference length L is only a fraction of the real characteristic length of the aircraft or component being tested, the remaining three parameters in equation 2.14 must be changed in order for the coefficient to remain constant. This can be done, for example, by employing different working fluids (other than air and of greater density, e.g. water) or by accelerating the flow to a higher velocity than that of the real flight – presently, however, only the latter will be considered. Simultaneously, relatively undisturbed flow, representative of ideal stationary atmospheric flow conditions during flight, must be provided inside the test section, if accurate performance predictions, flow observations or measurements of any kind are to be made.

Types of Wind Tunnels

Almost endless variations of specific features of wind tunnels exist and, virtually, every wind tunnel with a test section larger than two square feet is one of a kind [Barlow et al., 1999]. However, there are two basic types of wind tunnels and two basic types of test section configurations. Namely, each can either be open or closed.

The air flowing through an open circuit (Figure 2.13a) tunnel follows an essentially straight path from the entrance through a contraction to the test section, followed by a diffuser, a fan section and an exhaust of the air. The air flowing in a closed return wind tunnel (also denominated as a Prandtl or Gottingen type, see Figure 2.13b) recirculates continuously with little or no exchange of air with the exterior. The test section of both types of wind tunnels (marked red in Figure 2.13) may have or not solid boundaries, in which case it is either a closed or open jet type of section, respectively. As with any other engineering design, there are advantages and disadvantages with both the open and closed circuit type wind tunnels and with both open and closed jet test sections.

Due to lower initial costs, open return wind tunnels are ideally suited for schools and universities where a tunnel is required for classroom work and research, and high utilization is not required. In contrast, a closed return wind tunnel is generally preferred for most industrial applications. As the latter is equipped with corner turning vanes and screens and the flow is continuously recirculated, it is much

(a) (b)

Figure 2.13: (a) Typical layout of an open circuit wind tunnel; (b) Typical layout of a closed circuit wind tunnel [Barlow et al., 1999].

cheaper to operate over long durations (less energy is required to accelerate the fluid), flow conditions are less sensitive to other activities in the building and/or to the weather (neither its inlet and/or exhaust are exposed to a room nor open to the atmosphere), and the quality of the flow can be well controlled. This does, however, make the closed return configuration less suited when extensive use of smoke flow visualization techniques is intended, provided there is no mechanism to purge the tunnel.

Ideally, the flow in the test section would present an uniform velocity profile at each station, constant pressure, no up nor cross flow and no turbulence, representative of conditions observed during stationary atmospheric flight. Realistically, up to 0.3% deviations from the average speed, or 0.6% deviation in dynamic pressure, and 0.1 degree deviations from the average flow angle are to be expected. The flow should be steady and, should any time depended variation exist, it should be of small amplitude and frequency as not to be noticed on balance and pressure measurements. Turbulence level requirements will vary according to practice but for most development applications a value of 0.5% is acceptable. However, lower values of 0.1% are typically desired.

Closed test sections typically offer the most controlled environment for wind tunnel tests, and are thus generally preferred. Open throat test section provide easier access to the model, simplifying set-up and removal procedures, and better visualization of on-going tests. In this case, if the wind tunnel has an external balance, that balance is usually shielded from the air jet and one of the boundaries tends to be closed. It is common for wind tunnels to have both the open jet configuration, by default, and a closed throat insert to be mounted according to the requirements of each test or the preferences of each user.

Wind Tunnel Measurements

The aerodynamic characterization of the flow surrounding the model inside the test section of a wind tunnel is performed by appropriate balances and instrumentation, depending on test type and application. Typical wind tunnel applications are in aerodynamic design, performance and control prediction, systems integration and computation of aerodynamic loads for structural design. Typical tests require mainly force, moment, and pressure measurements.

Modern force and moment measurements (such as lift, drag and pitching moment) are generally performed directly with six component balances, that measure forces in three perpendicular directions and moments about the same three axes. This is not always the case, however. Drag measurements are also commonly performed by surveying the momentum deficit in the wake behind the body, with a series of local flow field pressure measurements at several spanwise locations using probes or rakes. These

are appropriate for pressure measurements away from the walls. When surface pressure measurements are required either pressure taps or pressure sensitive paints are typically used.

A pressure tap, which consists of an orifice internally connected by a tube to a pressure sensor, on a wall is the most commonly used device to to provide pressure measurements on the surface of a body submerged in a fluid. However, the pressure measured at a static pressure hole differs slightly from the true static pressure, by an amount which depends on the hole size and shape [Shaw, 1960]. It was found that nearly true static pressure is obtained for very fine holes, and that small positive errors are present as hole size is increased. The round-off of the orifice shape also contributes to static pressure measurement error: a radius applied to the edge of the orifice produced a positive change in the pressure reading, while a countersink produced a negative change. And so does the orientation of the hole centerline to the surface: holes inclined downstream give positive changes in pressure readings, while negative changes are observed where holes are inclined upstream [Rayle, 1949].

It is, then, generally assumed that infinitely small square edged holes installed normal to flow boundaries give the correct static pressure. Now, it seems a relatively simple exercise to drill a small hole perpendicular to a flow boundary, but in reality, small holes are difficult to machine and exceedingly difficult to keep burr-free, an additional source of error (positive if the burr is placed downstream and negative if upstream) [Shaw, 1960]. Also, the smaller they get the slower they are to respond to pressure changes. Large holes, however, are less accurate by the amount of distortion they introduce in the flow-field due to eddies in the cavities (the shear stress of the boundary layer passing over the static pressure hole induces recirculating flows in the cavity, which in turn entrains relatively high momentum fluid from the free stream into the static pressure hole, resulting in a higher pressure reading).

Additionally, static pressure taps are capable of providing information only at discrete points on a surface. All these limitations make pressure taps very time-consuming and expensive to implement. In the aerospace industry a pressure-instrumented wind tunnel model for the purpose of estimating surface loads (equiped with hundreds to a few thousands of these pressure taps on the surface) costs on the order of $500,000 to $1 million to construct, the pressure taps and their installation accounting for approximately 30% of this expense [McLachlan and Bell, 1995]. These pressure loads are used to perform the structural analysis and design of the vehicle, and are generally not updated as the aerodynamic design is refined due to the associated costs.

Alternatively, modern wind tunnels implement Pressure-Sensitive Paints (PSP) instead of physical pressure taps [Kraft, 2010], providing cost-effective and updated structural load information as the aerodynamic shape of the vehicle changes during the complete design cycle, and facilitating validation against computational tools, as illustrated in Figure 2.14.

When using PSPs, the model surface is coated with an oxygen-sensitive luminescent molecule dispersed in an oxygen-permeable polymer binder and illuminated with suitable exciting radiation. The intensity of the resulting luminescence depends on the oxygen partial pressure seen by the coating molecules. Since the mole fraction of oxygen in air is a known constant, the air pressure can be readily calculated from a measurement of the luminescence intensity. In an aerodynamic test the luminescence intensity distribution associated with an airflow induced pressure field over the surface of a model can

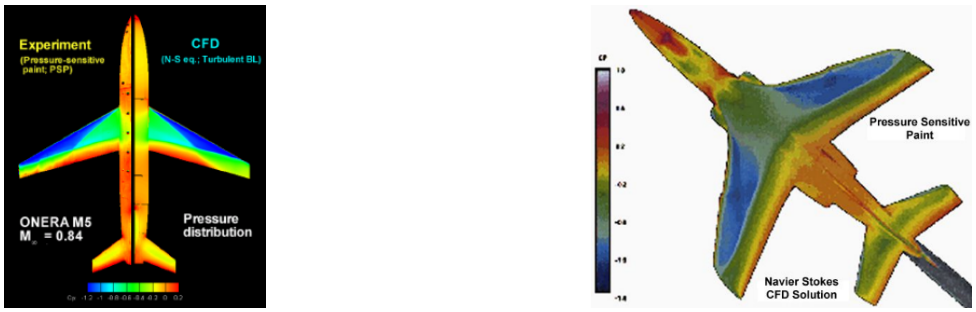

(a) (b)

Figure 2.14: Examples of PSP results against CFD solutions (a) For a typical airliner configuration [Jahanmiri, 2011] and (b) for a typical jet-fighter configuration [Jackson, accessed May 23rd, 2016].

be recorded using an imaging camera. As a pressure sensor, PSPs are unique as they provide a field measurement, pressure being measured over the entire surface of a model simultaneously at a very high spatial resolution.

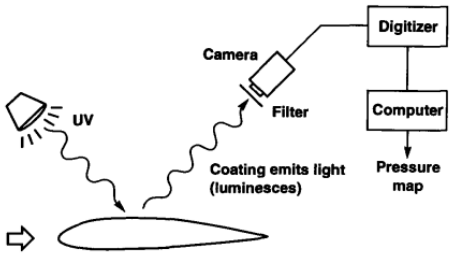

Figure 2.15: Schematic representation of PSP concept [McLachlan and Bell, 1995].

With pressure data available over the entire model surface, flow anomalies at any point on the surface are immediately obvious, rather than having to be deduced from discrete tap data or additional flow visualization tests. The cost of a PSP measurement system is small compared to that of installing even a small fraction of the pressure taps in a large wind tunnel model, and unlike taps, which must be installed in each new model, the PSP system can be reused indefinitely and the cost amortized over many tests. However, higher initial investment might be required if proper illumination, imaging, filtering, data acquisition and post-processing tools and equipment are not available in the testing facilities from the start. The most relevant drawbacks regarding pressure sensitive paint are its intrusiveness effects on aerodynamic data due to altered smoothness or roughness of the model surface with the PSP coating, neglectable in most but not all applications, namely low speed flows [Amer et al., 2003], its coating's luminescent intensity sensitivity to temperature gradients [Bencic, 1999] and its limited shelf-time due to the degrading response of the luminescent molecules in the PSP coating with time of exposure to the excitation illumination [Jackson, accessed May 23rd, 2016].

Interesting intermediate state-of-the-art solutions are flexible distributed pressure sensitive strips which offer a compromise in spacial resolution when compared to PSP, enabling only discrete pressure readings as with pressure taps, while providing a system that is easy and cost effective to implement. Two distinct solutions of this nature are the novel flexible pressure sensing strips, produced in both stan-

dard and custom formats (tailored to the model's geometry), equipped with micro-channels that connect orifices distributed on its surface to pressure transducer arrays [CSEM, accessed May 23rd, 2016] and capacitive sensor strips [Zagnoni et al., 2005].

Flow Visualization

All practices mentioned so far refer to quantitative measurements. However, relevant qualitative data can be collected with flow visualization techniques, both off- and on-surface. This discussion will be focused on simple, direct visualization, non-optical (not based on variations in refraction indexes) techniques applicable to wind tunnels with air as working fluid. A summary of alternatives is presented, for example, in Ristić [2007a] and Ristić [2007b].

Typical first approaches to flow visualization off-surface involve smoke injected into the flow in several ways and tuft nets (see figure 2.16). These methods allow for the observation and interpretation of flow patterns away from the surface of a model, revealing vortex structures in the flow (tufts and smoke), regions of flow separation and the shape and size of laminar separation bubbles (smoke). A useful practice, limited to low Reynolds numbers flows, when using smoke is to use a small diameter wire coated with oil: as this wire is heated, fine smoke streamlines form at droplets on the wire. As previously mentioned, however, smoke is generally not an ideal solution in a closed return circuit without means to purge excess smoke, which will be recirculated contaminate the posterior observations.

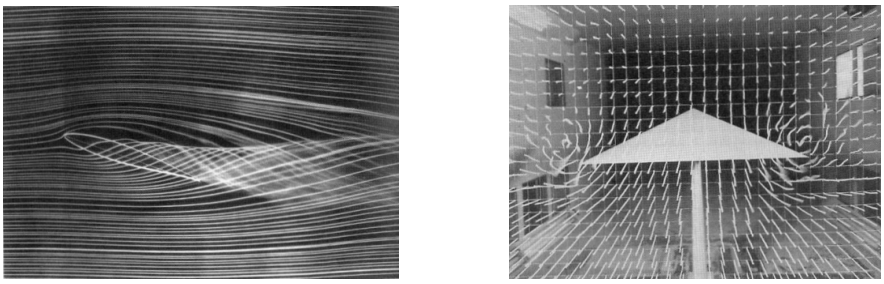

(a) (b)

Figure 2.16: (a) Streamlines past an airfoil visualized by smoke wire techniques; (b) Flow visualization with the tuft net method [Barlow et al., 1999]

Practical on-surface flow visualization traditionally use tufts, oil flow and china clay. The simplest and most frequently used method for surface flow visualization is to attach tufts to the surface of interest (figure 2.17). The tufts must be of light, flexible material that will align itself with the local surface flow as a result of direct aerodynamic force. The most commonly used material is light yarn or nylon monofilament (mini-tufts) with weights and lengths chosen according to model size and test speeds. Both can be treated with a fluorescent dye and observed under ultraviolet light to make them more visible. Even though the presence of tufts does affect aerodynamic force measurements to some extent, the method is so easy and economical to implement that is very often the first choice. Tufts readily show where flow is steady or unsteady and regions of complete separation and buffeting flow are readily identified. The resolution of the technique is determined by the spacing between tufts.

Liquid indicators, such as oil and china clay (among others) are widely used for depicting separation,

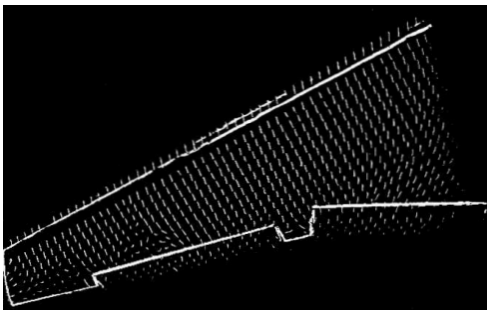

Figure 2.17: Fluorescent mini-tufts under an ultraviolet light source [Barlow et al., 1999].

flow direction and in some cases boundary layer transition. The selected material is usually spread on the areas of interest with a paint brush or roll. The flow speed of the air must then be sufficient to impress shear stress large enough to cause the oil to flow and reveal the surface patterns within an acceptable time. The most common material for oil flow visualization is petroleum lubricating oil. However, it is very messy to clean up afterwards, both on the model and more so in the tunnel. Also, the color of the oil needs to contrast with the color of the model surface. A widely used method is to use coloured oils (figure 2.18a) or to add a fluorescent dye to the oil and illuminate it with ultraviolet lights, as in the fluorescent mini tufts (figure 2.18b).

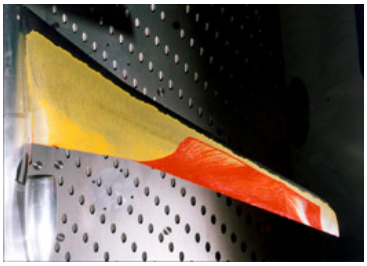

(a)

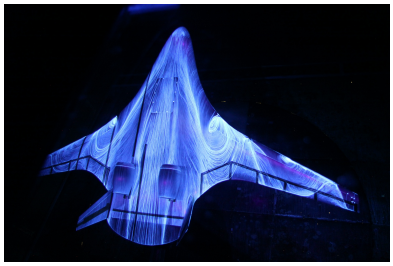

(b)

Figure 2.18: (a) Coloured oils with natural light [ONERA, accessed May 23rd, 2016]; (b) Fluorescent oils in UV light [NASA, accessed May 23rd, 2016a].

The choice of the oil medium for use with a particular pigment is determined by the time that is allowed for the pattern to develop in the prevailing conditions of air flow and surface shear. Oils of ascending viscosity, such as kerosene, light diesel oil and light transformer oil (by this order), are appropriate for increasing free stream test speeds. With one of these oils it is usually possible to mix a satisfactory paint which will start to flow at about 75% of the test speed and produce a fully developed pattern in about 2 minutes. The resulting pattern can be related to the distribution of skin friction coefficient on the tested surface [Maltby, 1962].

China clay (figure 2.19) is a suspension of kaolin in kerosene. It is a suspension technique most often practiced in low-speed wind tunnels in test conditions of 1 atmosphere and Mach numbers from 0.05 to 0.3. A typical mixture uses about 100 ml of china clay per litre of kerosene. At the time of application the mixture is stirred and liberally applied to the model surface with a brush or painting roll. It is best if the test surface is mostly horizontal as the low-viscosity carrier will start to run immediately on vertical

surfaces. Soon after application, the wind tunnel must be brought up to speed. The bulk of the liquid is sheared away quickly but the remaining indicator spreads in a thin layer and begins drying. When in liquid suspension the mixture is almost transparent but as the carrier dries the remaining china clay deposits take on a white appearance. If the model is dark, it provides a good contrast. Also, fluorescent or coloured pigments may be applied to the basic mixture for improved results [Johnson, 1998]. When the mixture has dried, photographs can be taken after the tunnel is shut down as the flow pattern does not change rapidly with time. It is one of the simplest methods to set-up and apply. This method clearly shows the flow pattern and flow separation.

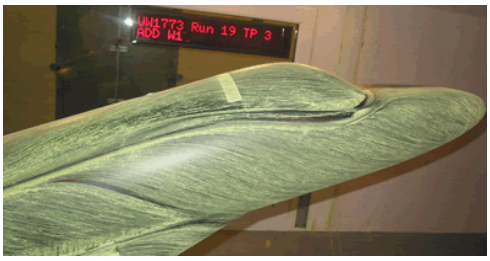

Figure 2.19: China clay flow visualization [University of Washington, College of Engineering, accessed May 23rd, 2016].

For comparison and validation purposes, often the most important information being sought by flow visualization methods is the locations for transition from laminar to turbulent boundary layers. It cannot be determined by tufts, and oil flow, infra-red imaging and sublimation techniques are the most suited. However, the china clay technique, with some difficulty, can also be used for this purpose. When attempting this it is not required to wait until the mixture has dried thoroughly, because due to different evaporation rates of the kerosene under laminar or turbulent flow, transition can be identified when the laminar region remains wet and the turbulent region is dried [Maltby, 1962]. This technique has been used by De Brederode et al. [1996] and compared against the stereoscope technique with good results, but it is only accurate when the transition occurs on-surface (as opposed to LSB associated transition).

Model Design

The proper conduction of wind tunnel experiments is limited to a constant pressure volume within the test section, function of the wing tunnel geometry. Limiting the model's dimensions inside this constant pressure volume is one of the most practical ways to avoid unacceptable experimental errors. On the other hand, it is evident that it would be attractive to test largest possible model, not only enable an increase of the testing Reynolds number but, additionally, to improve the accuracy of force measurements and of model geometry (smaller models prepared with the same tools will be less accurate due to resolution limitations in the manufacturing process).

Thus, it is important to have reliable criteria to choose the model size. The general rule of thumb states that the model span should be less than 0.8 of tunnel width due to, mainly, the adverse effects of wind tunnel walls on the flow [Swanson and Toll, 1943][Barlow et al., 1999]. In order to make the most of the available space, half models (or semi-span models) are often used, for tests limited to symmetric

flow conditions (figure 2.20). Asymmetric flow is prevented by a large plate at the plane of symmetry (or reflection plane), or by mounting the model on the floor, hence the additional designation of reflection plane models. The increase in Reynolds number over that of a full model is typically of the order of 20% [Barlow et al., 1999]. Another advantage relates to model construction costs. Additional popular model types include bi-dimensional models (airfoils), which span from wall to wall or are equipped with end plates to prevent the generation of wing tip vortices, and component test models that are comprised by only a section of an aircraft (e.g. an isolated fuselage or wing, the wing-root connection or the wingtip) in order directly study its performance or to allow a larger scale to be used.

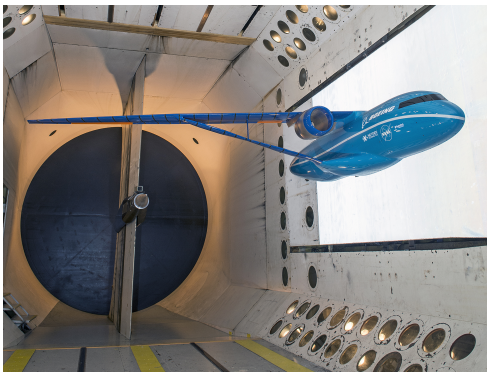

Figure 2.20: Aerospace industry grade semi-span wind tunnel model [NASA, accessed May 23rd, 2016b].

Independent of this, as previously stated, a substantial portion of project resources in terms of both time and money is typically consumed by the design and manufacture of wind tunnel models, often limiting the scope of experiments. Thus, methods that can expedite the model building processes are highly beneficial.

The manufacture of wind-tunnel models has traditionally been a highly skilled and time consuming process. By their nature aerodynamic bodies can have complex three-dimensional curvature and often the experiment requires internal details such as the provision for surface-pressure tappings. Thus, wind-tunnel models are often constructed from a number of parts, which require accurate fitting and hand finishing to obtain the necessary high surface finish. Ideally, the wind tunnel experiment is an integral part of the design process, which may call for a prescribed range of model configurations to be tested, or alternatively for the iterative optimization of a particular feature of the model. In the former case the range of configurations that can be tested is limited by the cost of each model and in the latter case by the speed at which a model feature can be changed [Heyes and Smith, 2004].

Whereas there are a number of different rapid-prototyping (RP) processes, two in particular are suitable for wind tunnel model manufacture, primarily because the resulting components have sufficient rigidity: stereo-lithography (SLA) and fused deposition modelling (FDM), which makes use of modern 3-D printers.

Stereo-lithography uses a vat of photopolymer epoxy resin which is sequentially cured and solidified under the light of an ultraviolet (UV) laser. The laser solidifies each layer in turn as the tray in which the resin lays is lowered and the next layer is solidified. The process is continued until the part is complete.

Upon removal from the machine the part requires post processing, being rinsed in a solvent to remove excess resin and post-cured in a UV chamber.

The FDM process involves layering extruded molten filaments of a thermoplastic polymer, typically Acrylonitrile Butadiene Styrene (ABS) or Polylactic acid or polylactide (PLA), via a movable nozzle in very thin layers, in a way similar to that of a hot glue. The plastic filament is supplied in rolls.

Both processes are limited by both horizontal and and vertical resolutions. Both methods can possess equivalent vertical resolutions, as low as 0.02 mm per layer, but the SLA's horizontal resolution is not limited by nozzle size, hence typically providing better results. Also, this process subjects the printed object to less forces and mechanical vibrations, ultimately resulting in much smoother surface finishing. This is supported by findings that state that the SLA method is the best RP process for preliminary design wind tunnel testing [Springer, 1998].

Due to resolution limitations, RP parts are sometimes visibly ridged with each vertical step, more so in FDM parts, and whereas SLA parts require minimal surface hand-finishing, lower resolution FDM parts often need to be extensively wet-sanded and coated. On the other hand, FDM, and namely 3-D printing, is a low cost prototyping technique and provides the most cost effective solution.

Both methods offer a number of key advantages over traditional methods for manufacturing wind tunnel models [Heyes and Smith, 2004], namely:

- the possibility of incorporating internal features directly into the modelling, allowing integration of surface pressure taps, for example;
- the capacity to produce models with a honeycomb internal structure, allowing for weight savings while maintaining structural rigidity;
- short times from CAD model to prototyping machine, which can take only a matter of minutes;
- machines operate mostly unsupervised, hence the operating costs being little more than the cost of the material.

Studies such as Springer [1998] have shown that rapid prototyping models show promise in limited, direct application for preliminary aerodynamic development studies at subsonic, transonic, and supersonic speeds, where cost savings and model design and fabrication time reductions greater than a factor of 4 can be obtained, relative to conventional model design and fabrication practices. The accuracy of wind tunnel test results, although lower than for a conventional machined metal model, mainly due to higher surface finish and dimensional tolerances and limited material properties that facilitate the bending of model components (more critical in thin section parts such as tips and control surfaces) produced by RP techniques, is considered accurate enough for that level of testing.

This makes wind-tunnel testing more affordable for small programs with lower budgets and for educational purposes, especially when dealing with more complex or less traditional designs where classical analytical and empirical tools often-times fall short.

2.3.3 Scalling to Free Flight

As previously stated, there is no traceable difference to having the model at rest and the air moving relative to the local earth reference. However, the distances of most (if not all) of the free stream boundaries away from a model are usually much less in wind tunnel than the distances observed in actual flight. The presence of these constraining boundaries at a finite distance from the body produces several unintended effects on measurements. In addition, the wind tunnel stream may not have the same distribution of flow properties as in free flight, i.e., flow non-uniformities such as flow angularity and spatial variations in dynamic pressure. A uniform stream is the most commonly envisioned ideal operational condition that is to be only approximated by a wind tunnel test. However, relatively small deviations can have significant effects on resulting surface stress distributions and corresponding total forces. These effects are in their nature interdependent, but are traditionally accounted for separately, with boundary (or wall) corrections [Barlow et al., 1999].

The most relevant corrections, for the intended purpose, as identified by Barlow et al. [1999] target:

- horizontal buoyancy, in reference to a variation of static pressure along the test section when no model is present;
- solid blockage, regarding the ratio of the ”frontal area” of an article to the stream cross sectional area, which is effectively zero in most actual operations; in wind tunnel tests, however, this ratio reflects the relative size of the test article and the test section, and it is usually chosen to be in the range of 0.01 to 0.10, with 0.05 being typical;
- wake blockage, resulting from the finite size of a body's wake and is in this sense similar to solid blockage. It is more complicated, however, as the size of the wake is itself a function of the body's shape and the ratio of the wake area to the stream cross section;
- streamline curvature, which refers to the alteration of the curvature of streamlines in the flow about a body inside a wind tunnel test section as compared to the corresponding curvature in an infinite stream;
- normal downwash change, relating to the component of induced flow in the lift direction at the test article; it is changed due to the finite distances of the boundaries;
- spanwise downwash distortion, due to an alteration of the local angle of attack along the span of a lifting wing.

Analytical techniques use solutions for the subsonic potential equation of the flow field in order to assess the boundary interference corrections. The classical application of these effects is done in a linear manner, each contribution estimated with the inclusion of a single singularity, doublet, source or sink, concluded with the superposition of all individual effects. Semi-empiric methods combine ”in situ” experimental measurements at the walls with the analytical solutions of the subsonic potential equation in order assess boundary corrections. Finally, numerical techniques use a panel method code or a CFD solver in order to determine the wall interference flow field, by taking the difference between the

wind tunnel and free flight simulation solutions [Ulbrich, 2016]. The latter can also be improved further by performing measurements at the test section boundaries and explicitly impose them as boundary conditions in the wind tunnel simulation [Lombardi G and Morelli, 2000].

Additional boundary corrections are required when studying stability, asymmetric flows and propeller effects, and both their relevance and value are highly dependent on both the wind tunnel test section and model configurations. For example, in open test sections there are free shear layers instead of boundary layers at some or all of the stream boundaries and this generally results in higher levels of unsteadiness relative to closed test sections. Also, when a model is mounted on a tunnel surface (or on a reflection plane) there is a direct interaction between that surface's boundary layer and the model's boundary layer.

These boundary effects, or corrections, are inserted into an even larger group designated scale effects, or corrections. These also include interference effects due to the presence of a model mounting structure (generally non-existent in semi-span models), tare (of measurements), omission of geometric details and sub-scale model design. Among these, potential Reynolds number shortfalls due to the model's scale factor is often the major and long-standing flight-to-wind tunnel scaling issue due to inaccurate boundary layer representation, especially that relating to transition behaviour. The latter is particularly relevant for low Reynolds number airfoils and UAVs. In these cases a large portion of the wing could be laminar and predicting transition position could have a large impact on drag and overall performance. Typical correction levels for several scaling issues/concerns for the drag case can total on the order of over 12% [Bushnell, 2006].

Fortunately, few tests require all previous corrections to be applied. Unfortunately, the high cost associated with acquiring free flight test data makes the amount of information about scaling ground to flight methodologies rare in the open literature and are often company proprietary and part of their competitive edge. For the intended purposes, relevant exceptions are Heyson [1971] and Toll [1943]. However, corrections used for wind tunnel wall and model support interference will always be, to some extent, wind tunnel specific. Large wind tunnel-to-flight scaling discrepancies can occur application-to-application and condition-to-condition. Typically, the most serious discrepancies are associated with flow separation [Bushnell, 2006].

A rather simple example to illustrate the impact of different experimental conditions and inadequate scaling techniques in different facilities is the well-known profile like the NACA 0012, which still provides a challenge for wind tunnel measurements, with significant differences, in the order of 10%, between collected results [Aerodynamic scaling to free flight conditions: Past and present]. An example for a relatively clean, full configuration, at cruise conditions was presented by a 1983 survey which concluded that for 12 commercial transport aircraft, constructed by 3 major American manufacturers over a 20 year period, wind tunnel tests are just as likely to estimate too high a drag as too low a drag, as six out of the 12 (scaling) predictions were low, 4 predictions were high, and 2 were right on. Drag predictions were as much as 22% low and 10% high [Bushnell, 2006].

All these concerns have been changing the role of wind tunnels in the aerospace industry for decades, as the computational capability improves in all aspects – computer storage and speed, ge-

ometric representation and meshing, algorithms. Therefore, scaling to free flight, per se, as an empiric or analytical practice, is becoming a subject without an object as increasing importance is given to CFD predictions. Current trends change the function of the wind tunnel from a predictor to a source of calibration and/or validation data for computational methods, whose simulation results are then utilized as the flight prediction and/or wind tunnel scaling tool [Bushnell, 2006]. Suggested reading on this subject are the published studies of Ciobaca et al. [2009] for open test sections and Melber-Wilkending et al. [2006] for closed test sections.

2.4 Note on the Complementarity of CFD and Wind Tunnel Testing

It has been argued that modern advances in computer hardware and software have the potential to dramatically alter the design and development processes for flight systems that include not only computational fluid dynamics but computational science and engineering in general. However, after almost half of a century, advanced computational science and engineering have still not significantly decreased the need for testing facilities or effectively reduced the overall cycle times for development of flight systems, and as of 2010, as many wind tunnel test hours were used in the process as over 20 years ago. This section is heavily based, but not solely, on the arguments presented by Kraft [2010].

The key concept into making progress on reducing the overall cycle time of a flight system's project, and associated financial costs, is in merging wind tunnel testing and CFD, instead of attempting to replace the former with the latter. In the United States Air Force (USAF), integrated computational fluid dynamics and wind tunnel testing (WTT) approaches have resulted in millions of dollars in savings. Two practical examples are the integration of CFD into the development process of the F-22, reducing the cost of models for testing in over $8 million, and the B-1B, for which CFD simulations of flare ejections eliminated a major part of a flight-test program with cost savings of $500 000 to solve an operational problem. These examples also illustrate the versatility of the CFD method.

In the early phases of design, when literally thousands of configurations need to be evaluated quickly, albeit with simpler engineering models, and, as the design matures, a handful of parametric factors need to be studied with increasingly higher fidelity. The quick turnaround computing to support interactive design, at this stage, is invaluable.

As stated by Kraft, USAF (2010), *"There is, however, a point at which doing another CFD solution will not reduce uncertainty further; hence, one needs to move on to wind tunnel testing. Likewise, there is a point of diminishing returns for doing another wind tunnel test, and the program needs to move on to flight testing"*.

Typically, once testing (either wind tunnel testing or flight testing) has commenced, CFD is heavily used as a complementary tool. Applications range from previewing test facility instrumentation requirements, analysis of potential wind tunnel effects such as support or wall interference and extrapolation of wind tunnel data to flight conditions (using computational methods, corrections for any shape and size tunnel can be obtained), to support operational flight issues that occur after a system has been developed and to evaluate incremental effects or anomalies that might show up during flight testing.

There are, however, limitations to the extent of this practice. Namely, computing power is not the sole requirement for an adequate performance of CFD tools. Having software that can efficiently and effectively make use of that computing power as well as robust algorithms for modelling of essential physical phenomena and verifying and validating (V&V) data and methods is equally important. Also, the fact that test facilities are used to predict not only the performance, to which the majority of published applications of CFD in aerospace refer to, but also the operability, reliability, and maintainability of an aeronautical system is frequently overlooked.

On the one hand, visual output from high-fidelity CFD models provides unprecedented insight into flow features difficult to obtain in any other way, and enabling the visualization of streamlines and vortex patterns on flow over a vehicle brings new understanding in the causative relations between aerodynamic shapes and vehicle performance. These tools also allow relatively rapid evaluation of changes to the design, which in its own way introduces even more insight. On the other hand, focusing only on advanced computational modelling has the downside of limiting real understanding of the physics of the problem, especially when extending into realms beyond the physical fidelity of the model. The experience gained from physically measuring phenomena is important because provides more depth in understanding and is absolutely essential to guide development and application of models to capture the physics of a problem. Models are only as good as the physical understanding of a problem, achieved through experimentation.

In summary, CFD simulation and wind tunnel testing each have inherent strengths and weaknesses. By understanding them, one can use them for their mutual benefit, creating synergies to allow for more efficient design cycles and reducing overall costs.

From the CFD's perspective, these costs are related with software (licensing fees and cores per parallel process), hardware (cost per physical cpu core) and operation (time to/per solution, power) requirements. Hence CFD being typically associated with lower initial costs and higher costs over time, per additional data point, relative to WTT.

From the WTT's perspective, the costs are linked to model design (complexity by number of parts and pressure taps, controls, quality of CAD models, time from CAD to test ready model), wind tunnel occupation (cost per hour of wind tunnel time, which is not applicable to the PrtAF as internal testing facilities are available, and cost per non-standard instrumentation) and operation (efficiency of staff, efficiency of equipment and data reduction tools, power costs). Generally this results in lower costs over time in spite of the much higher initial cost of actually building a test facility or even ordering a typical commercial aerospace grade model [Aeronautical Testing Service, Inc., 2010].

However, and in conclusion, the ever occurring technological advances are continually and positively reshaping both approaches, levelling the field further, and making them as attractive to the aerospace industry as they are useful, namely: by bringing tool improvements that increase experimental accuracy, reducing costs of sensors and introducing rapid prototyping techniques to model design (which can be modular from the start, for quick component changes), lowering the originally high cost and effort associated with setting up new cases and bringing added value to results; by decreasing hardware costs, lowering initial investment requirements in CFD; and by increasing computational power in process-

ing and communication speeds, introducing work-flow oriented software suited with intuitive graphical user interfaces (GUI), improving integration with other tools (such as CAD), developing more automated meshing tools (like surface wrapper and adjoint based mesh refinement), promoting new licensing formats such as the power-session concept and facilitating power on-demand computing, decreasing the effort and cost associated with the continued use of CFD.

Chapter 3

Methods

3.1 The Application and Validation Cases

In the context of unmanned aerial vehicle development in the Portuguese Air Force, an effective and efficient, experimentally validated computational fluid dynamics methodology is sought in order to provide accurate aerodynamic performance assessments of such platforms through their design cycle. This study aims to provide recommendations on such procedures, based on CFD and aerospace industries' best practice guidelines and the outcome of their implementation on an application case, namely, the Antex-X02 ALFA of the Portuguese Air Force, illustrated in figure 3.1.

Figure 3.1: The Antex-X02 ALFA.

In service since 2006, this is a small Class I unmanned aerial vehicle with a typical twin boom pusher prop configuration, reducing propeller effects on fuselage and mid-wing section aerodynamics and allowing the incorporation of Intelligence, Surveillance and Reconnaissance (ISR) subsystems without visual field limitations due to propeller interference [AFA, 2012].

It was developed as a test-bed for flight testing and novel technologies, equipments, engines, payloads, control algorithms and concepts of operation and is particularly suited for coastline and forest surveillance, traffic monitoring and vehicle tracking. It's easy to operate and maintain, and can be equipped with either an electric or internal combustion engine for a more flexible operation.

Several prototypes were made and operational specifications are not constant across all iterations. However, these platforms have up to 15 kilograms of maximum take-off weight (of which 50 percent is available for payload), an autonomy of either 2 or 5 hours if internal combustion or electric propulsion is used, respectively, a maximum operational ceiling at 2000 meters of altitude and a maximum speed of approximately 40 meters per second.

The main wing was designed with a Wortmann FX63-137 airfoil (see figure 3.2) which provides the ALFA with high lift and low stall speed characteristics, and enabling it to perform short take-off and landing (STOL) maneuvers. Its 0.325 m chord and 2.60 m span (including the Woerner wingtips) result in an aspect ratio 8 wing.

Figure 3.2: The Wortmann FX63-137 airfoil.

As the ALFA shows tremendous operational versatility due to its design, modular construction and significant payload capacity, in spite of its small size, cruise conditions vary according with the mission it performs. As it will be discussed in greater detail over following sections, flight testing was performed at an average operating speed of 19 m/s and 1400 ft (roughly 426 meters) in altitude, which were reported as typical parameters for the platform. Considering international standard atmosphere (ISA) air properties, and the reference length of 0.325 m (the main wing's chord) this is equivalent to an operating Reynolds number of approximately 4.1×10^5.

During the course of this work, computational methodologies (CFD) supported by experimental efforts (including wind tunnel and flight testing) suitable for data correlation across different approaches will be employed. In an attempt to address validation requirements for both computational and experimental methodologies, additional test cases are studied by means of simpler two-dimensional and three-dimensional problems for which sufficient and reliable published data is available for comparison purposes.

The 2-D benchmark studies the same Wortmann FX63-137 airfoil that equips the wing of the ALFA at a Reynolds number of 3.5×10^5 and angle of attack values of 1, 3 and 5 degrees. In the early days of small UAV design, one typically did not rely on designing an airfoil section for the particular UAV under consideration. Instead, the designer often used an airfoil section already designed and tested for some other application and the FX63-137, originally designed by F.X. Wortmann in 1981, was a popular choice [Mueller and DeLaurier, 2003]. Accordingly, this airfoil was the object of numerous wind tunnel tests in several different publications regarding low Reynolds number aerodynamics (Re under 5.0×10^5). This specific Re number was chosen due to its proximity to actual flight test conditions and range of available published data, which includes flow visualization data. However, there is a certain amount of uncertainty related to the published data, as results are significantly scattered. This issue has been the object of discussion in studies such as those by Marchman [1987], and is most likely linked to slightly different experimental conditions and the high sensitivity of the LRN regime. The choice of tested values for the angle of attack was considered sensible due to the fact that validation is procured for cruise conditions

only. This validation exercise will only be performed computationally.

The 3-D benchmark comprises a rectangular aspect ratio 8 wing, once again featuring the Wortmann FX63-137 airfoil as cross section profile, tested for $Re = 3.0 \times 10^5$, the maximum value for which published results were found to be available for this configuration, and angle of attack values of 1, 3 and 5 degrees on CFD simulations and ranging from -5 to 10 degrees in wind tunnel tests. The latter was considered advantageous due to the perceived lower cost (in testing time) per additional data point associated with wind tunnel testing when compared to three dimensional CFD simulations.

3.2 Computational Simulation

The computational fluid dynamics (CFD) simulations were performed on Star-CCM+ v10.04 [CD-adapco, 2015]. This commercial software allows for simplified unstructured meshing procedures, and provides an intuitive, linear work-flow type, graphic user interface (GUI) and a wide variety of finite volume (FVM) solvers.

The validation cases are also put through XFLR5 v6.12 [Deperrois, 2009b] calculations, in order to collect additional reference data for posterior correlation. This is a successful analysis software tool, primarily based on potential flow and panel methods, that enables small aerodynamic studies of simple geometries (both 2D and 3D) at low Reynolds numbers and provides fast calculations with a good compromise between accuracy and computational and temporal requirements. It has been extensively used in the aerospace industry and scientific community for academic purposes, as an auxiliary tool. This section however, will focus on the implementation of the formerly introduced CFD tool.

As previously stated, three increasingly complex external aerodynamics studies will be performed. The purpose of this is to take advantage of the simplicity and lesser computational and temporal requirements of the first cases and build up towards a computational approach applicable to a complete aircraft configuration that has already been proven to be successful in smaller, but representative, test cases. This assessment is made by correlating and, if possible, cross-validate, the collected data with published results from the literature. This is another advantage of starting with simpler and popular geometries, as they may already have been subjected to similar tests under similar testing conditions.

The 2-dimensional validation case is the first step towards establishing a set of recommended practice guidelines in CFD for UAV external aerodynamics. The use of a simple airfoil geometry (identical to the final application case) under the same flight regime (although at a slightly lower Reynolds number) allows for an increased number of simulations in a shorter period of time due to reduced computational requirements.

Neglecting, thus far, any 3-dimensional effects which will eventually rise during the course of this work, this initial validation case is used to perform a wide variety of sensitivity tests to a range of computational set-up parameters in order to identify those most suitable for this specific application. The starting point is always grounded on industry and academia best practices, studied from the literature.

In summation, these sensitivity tests were performed to evaluate turbulence and transition models, grid refinement requirements, including the placement of local refinement, computational domain sizing

and boundary condition prescriptions.

The suitability of each setting was evaluated differently depending on their nature. A grid parameter setting is considered adequate when a further increase in mesh refinement will not contribute significantly (within 1%) to an improved solution, considering its relative deviation against results of reference (e.g. published data). This concept is designated as grid independence, and it is generally verified refining the entire mesh proportionally (through its base cell size) but it can also be evaluated for individual grid parameters. In practice, however, grid independence is not always attainable, due to increased computational and temporal requirements (the more refined the grid, the longer it wakes for a converged solution to be attained, and the more resources are required), and therefore a compromise has to be made to the desired accuracy (i.e. correlation with published results) in light of the available resources. The appropriate size of the computational domain is also found with this procedure, since an increased distance between the object being tested and the remaining boundary conditions (designated as the far-field distance to the computational domain flow inlet and outlet boundaries, to name a few) will have favourable effect on the solution, due to a decrease in the interference that different boundary conditions have over one another.

Additional simulation parameters, such as those connected with turbulence and transition modelling, as well as inlet turbulence specifications, are evaluated differently, i.e. with results other than the integral quantity of interest (such as the overall lift and drag coefficients). Specifically, the pressure and skin friction coefficients distributions were monitored and compared with other numerical and experimental representations, in order to determine if relevant flow features such as the laminar separation bubble were being accurately captured, in spite of lift and drag prediction result correlations.

The 3-dimensional test case was used, mainly, to confirm the applicability of all previously established settings to 3D simulations. This is relevant since the rise of 3-dimensional flow features, not captured by 2D simulations, could possibly undermine the effectiveness of the computational model developed up to this point, and additional adjustments may be necessary.

Also, with reference to guidelines present in the literature, additional grid recommendations are implemented in order to deal with the 3D flow structures introduced by this case, the most relevant of which are wingtip vortices, a defining characteristic of aerodynamic flows over finite wings.

The ALFA case simulation was partially set up with the previously established parameters and completed with the introduction of additional measures aimed at dealing with full geometry effects, such as additional components (e.g. fuselage, landing gear, tail, etc.) and flow interactions between those different aircraft components (e.g. wake of the fuselage on the tail). Propeller effects were not included, though related research was undertaken in order to introduce them in the future.

In these simulations, the following criteria were used to evaluate (and compare) their performance:

- Solution convergence, evaluated by both residual convergence down to acceptable levels and stabilization of the lift and drag coefficients;

- Dimensional and adimensional velocity profiles of the resolved boundary layer and correlation with theoretical models;

- Correlation of lift and drag coefficients with published data and XFLR5 results (validation cases only);
- Surface chordwise pressure coefficient distribution, detection of laminar separation bubble bump and transition, and correlation with published data and XFLR5 results (validation cases only);
- Skin friction coefficient distribution, detection of flow separation and reattachment locations, and correlation with with published data and XFLR5 results (validation cases only).

All simulations were set to free flight conditions, with no explicit or implicit wind tunnel effects modelled. Additionally, all final templates (final configuration of each case) were evaluated for grid independence and numerical uncertainty.

The summarized list of recommended practices is presented in Appendix A.

3.3 Flight Testing

Flight testing required the development and programming of a in-flight data acquisition system equipped with pressure sensors and an angle of attack sensor, to be placed inside the payload section of the Antex-X02 ALFA NC 17507 (A07) unmanned aerial vehicle.

Miniaturized, low-cost sensors and electronic (Arduino based) components were use into building the entire circuit. The system was self-sufficient, working on its own batteries, independently from other on-board equipment.

The angle of attack sensor was of the wind vane type, using a Hall Effect sensor and diametric polarity magnet combination.

The pressure sensors were sealed in individual 3D printed cells, finished with an impermeable light coating of epoxy resin and silicon to fill gaps.

The aircraft had to suffer modifications in order to accommodate these sensors. The angle of attack sensor was placed at one side of the fuselage, which was reinforced with extra layers of carbon fibre, and ahead of the wing. New wings were required for better compatibility with pressure tap installation. These were not built from scratch, but from a set of clean polystyrene core and carbon fibre coating wings left over from previous years. They were prepared with shorter ailerons placed closer to the wingtip (relative to standard configuration), in order to reduce their interference in the pressure readings. The pressure taps were spaced irregularly due to structural constraints and placed in greater number near the leading edge where higher pressure gradients are expected.

All systems were checked for functionality before flight through ground (test-bed) and wind tunnel tests.

Flight tests were comprised of several laps around a high aspect ratio rectangular circuit at three different altitudes (1000ft, 1400ft and 1800ft), averaging on 1400ft of altitude and 4 minutes of levelled flight each lap, roughly 2 minutes each way (neglecting the sharp turn). These procedures were repeated for three different outings on a single day with clear sky and little or no wind.

3.4 Wind Tunnel Testing

The testing facilities were prepared in order to perform the closed return wind tunnel tests with an open test section and a reflection-plane configuration because: flow quality assessments in this wind tunnel shown reduced turbulence in the open test section (relative to the closed test section, in contrast with what would be expected, based on literature) [Baltazar et al., 1997]; open test sections offer a more practical access to the test article and facilitate set-up; semi-span models mounted on a reflection plane allow for higher Reynolds numbers to be achieved, in this case, making it possible to match the operating Reynolds of the ALFA at cruise conditions.

The wind tunnel models – two of them, one for the 3D test case and another for the ALFA – were 3D printed in semi-span configurations with accommodations for fixing the model directly to the six-component balance. These models were designed (3D test case) and pre-worked (ALFA) at the CAD level in order to prepare the entire geometries to be printed, by parts, within the 3D printer's capacities, and easily assembled.

The assembly was done with epoxy resin glueing the parts together. During assembly, both models were reinforced with an internal carbon fibre tube (acting as a spar, or beam) and polystyrene section blocks (acting as ribs), for increased structural rigidity. Both models were wet sanded, coated with a epoxy resin based treatment, wet sanded again and painted, for a quality surface finish.

Pressure taps (fifteen in number), and respective tubing, were manually installed chordwise on the main wing of the ALFA wind tunnel model during assembly – ten over the upper surface, and five over the lower surface, irregularly spaced, in order to match the flight tests and capture regions of higher pressure gradients.

Sizing of the models was performed in order to constrain them to the constant pressure volume of the test section [Baltazar et al., 1997].

The wind tunnel tests comprised independent six-component balance measurements, china clay based flow visualization and, for the ALFA scale model, wall static pressure measurements at the pressure tap locations with both a professional grade pressure scanner and the developed data acquisition system.

Wind tunnel experiments and computational simulations were set up for the same operating Reynolds number of 4.1×10^5 and an angle of attack of 3° , a sensible estimate for cruise conditions.

Flow visualization tests, based on the china clay technique, were employed in both the application case and the 3-dimensional test case. Quantitative wind tunnel tests (i.e. except the flow visualization exercise) were re-run at least once in order to access result repeatability.

Chapter 4

Results

In this chapter, collected results for all the considered cases will be presented and discussed, starting with the 2-dimensional test case (the Wortmann FX63-137 airfoil, for $Re = 3.5 \times 10^5$ and angles of attack ranging from 1° to 5°), followed by the 3-dimensional test case (a rectangular aspect ratio 8 wing with the same airfoil, for $Re = 3.0 \times 10^5$ and angles of attack also ranging from 1° to 5°) and, finally, the application case (the unmanned aerial vehicle ALFA, at cruise conditions, with $Re = 4.1 \times 10^5$ and a 3° angle of attack).

4.1 2-Dimensional Validation Case

2-Dimensional test case results refer to: data collected from Star-CCM+ simulations during sensitivity tests of selected parameters – the most relevant, as many others were tested; grid independence and numerical uncertainty analysis; lift and drag coefficient predictions; pressure coefficient distributions; and flow feature (such as laminar separation bubbles) location and extent. These results are compared against both published data and complementary XFLR5 calculations.

The reference experimental and numerical results – collected from wind tunnel tests performed at the subsonic wind tunnel of the University of Illinois at Urbana-Champaign (UIUC) and XFOIL calculations, respectively – are cited from McGranahan and Selig [2003] and Selig and McGranahan [2004]. Whenever an exact match is not available for a direct comparison, reference values are linearly interpolated from the nearest available test conditions.

A summary of specifications for the computational set-up of this validation case is presented in table 4.1.

4.1.1 Sensitivity Tests

Table 4.2 summarizes the results for the performed sensitivity tests by presenting the influence of the most relevant parameters on results. These are relative to incompressible flow simulations performed in Star-CCM+, for the Wortmann FX63-137 airfoil at a Reynolds number of 3.5×10^5 and a 1° angle of attack, using the $k - \omega\ SST$ turbulence model combined with the $\gamma - Re_\Theta$ transition model.

Table 4.1: Summary of set-up specifications.

Geometry	
Body	Wortmann FX63-137 airfoil (2D)
Chord	0.0889 m
Computational Domain	Square
Physics	
Models	k-ω SST (Menter) turbulence with γ-Reθ transition and low y+ wall treatment
Reynolds number	$3.5x10^5$
Density	1.225 kg/m^3 (ISA-MSL)
Dynamic viscosity	$1.789x10^{-5}$ Pa.s (ISA-MSL)
Inlet velocity magnitude	57.5 m/s
Mesh	
Number of cells	$5.4x10^4$ cells (medium grid)
Prism layer resolution	32 layers
Base size	$1/10^{th}$ of the chord
Cell size on the wing surface	12.5%*
Additional local refinement (includes surface and volumetric controls)	Leading edge and trailing edge (3.125%*); wake (50%*); and nearfield (100%*)
Maximum Wall Y+	0.4
Average Wall Y+	0.1
Boundary Conditions	
Far-field distance	60 chords (all directions)
Tu (inlet and ambient)	0.003 (0.3%)
TVR (inlet and ambient)	1

* percentage relative to base size.

Relevant parameters are those considered most influential on the numerical solution and not software nor advanced-setting specific. The actual sensitivity study was more exhaustive and detailed, the motivation for this being the establishment recommended practices for the specific application to low Reynolds numbers flows, which was found to be insufficiently documented in the literature. The influence of each individual parameter is evaluated by its overall impact on solution, defined as the difference between the minimum and maximum values of both lift and drag coefficient deviation relative to published experimental data, tested for a range of settings (with at least three levels) either around or leading to the industry's best practice guidelines. This is done for the reader's convenience, the objective being to illustrate the effect that simulation set-up can have on solution, while focusing on the most frequent and transversal parameters.

The first observation to be made from this table is that the drag coefficient is consistently more sensitive to the variation of simulation parameters. In fact, the impact of most tested parameters on lift is under 1%, well under the computational model's uncertainty (table 4.3), and therefore considered neglectable. This is also reflective of the adequability of the recommended practices as an efficient starting point.

The second observation is that while the drag coefficient responded favourably to an increased mesh refinement, the same was typically not the case for the lift coefficient. This is particularly relevant for the

Table 4.2: Summary of sensitivity test results.

Parameter	Tested Settings	Impact on C_L	Impact on C_D
Far-field Distance	30 to 60 chords	0.3%	-3.0%
Prism Layer Resolution	24 to 40 layers	1.1%	-1.7%
LE and TE Refinement	None to 1.6%*	-0.5%	-1.6%
Wake Refinement	None to 25%*	0.1%	-0.4%
Wing Surface Refinement	12.5%* to 1.6%*	2.0%	-4.3%
Base Size	150%* to 75%*	-0.9%	-2.5%

*ratio to reference base size, set as 1/10th of the chord, presented as a percentage.

prismatic layer resolution and wing surface refinement parameters, contradicting expectations. However, it was found necessary to use high resolutions for these mesh parameters in order to meet turbulence and transition model requirements and appropriately capture low Reynolds numbers flow features such as small laminar separation bubbles.

Finally, regarding inlet turbulence specifications, it was found that turbulence intensity has a greater impact on results than the turbulent viscosity ratio. However, these values must be kept consistent with each other and the turbulence model being used, otherwise convergence problems and numerical errors may arise. These issues may be exacerbated due to the implicit three-dimensionality and unsteadiness of the laminar separation bubble flow, which are not accounted for by the bi-dimensional steady simulation. The influence of these parameters on the solution is reflected on both the integral parameters (such as the lift and drag coefficients) and the location and extent of flow features over the airfoil, such as laminar separation bubbles. Although higher turbulence levels were found to improve convergence, this had a negative impact on the characterization of the flow around the airfoil, anticipating laminar flow separation, transition and reattachment, reducing the extent of laminar separation bubbles, and delaying turbulent separation, effectively changing the nature of the flow field around the airfoil. With this in consideration, the turbulence specifications for the final 2D simulations from the computational models whose sensitivity test results provided the best agreement in flow feature location against published experimental results (see figure 4.12 and table 4.5).

4.1.2 Grid Independence and Uncertainty Analysis

Figure 4.1, figure 4.2 and table 4.3 present the results for the grid independence tests and numerical uncertainty analysis. These results refer to the case with a 1° angle of attack. The coarse and fine meshes have a base cell size of 1.5 and 0.75 times the base size of the medium mesh, respectively. The numerical uncertainty study refers only to the uncertainty due to computational domain discretization (i.e., assumes that round-off and convergence errors are negligible), and is performed according to the grid refinement index (GRI) technique, as introduced by [Roache, 1997]. Figure 4.1 illustrates this procedure.

In figure 4.1, the intersections of the linear trendlines for (a) and (b) with the vertical axis give the exact numerical solution ϕ_0, i.e. the estimated numerical result when $r_i = 0$ (if a grid had an infinite number of infinitely small cells), for the lift and drag coefficients, respectively. The uncertainty U for each

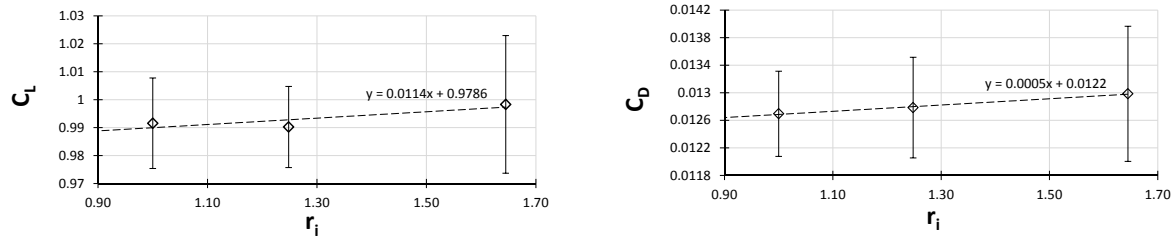

(a) (b)

Figure 4.1: Numerical uncertainty due to discretization for the calculated lift (a) and drag (b) coefficients. The grid characteristic number, r_i, on the horizontal axis, is defined as $r_i = \sqrt{\frac{h_f}{h_i}}$, where h_f refers to the number of cells in the most refined mesh and h_i is the number of cells in each different grid.

Table 4.3: Grid independence and uncertainty analysis.

		Coarse Mesh		Medium Mesh		Fine Mesh		
		$3.1x10^4$ cells		$5.4x10^4$ cells		$8.4x10^4$ cells		**Exact Numerical Solution**
Parameter	Exp. (UIUC)	Deviation	Uncertainty	Deviation	Uncertainty	Deviation	Uncertainty	Deviation
C_L	0.92	8.2%	2.5%	7.3%	1.5%	7.4%	1.6%	6.0%
C_D	0.012	11.3%	7.6%	9.6%	5.7%	8.8%	4.9%	4.6%

grid and parameter, represented by the error bars of the same figure, is defined as:

$$U = F_S \times |\delta_{RE}| \tag{4.1}$$

, where the safety factor F_S was set to 1.25 and δ_{RE} is the difference between the each grid's solution and the estimated exact numerical solution ϕ_0. The computational drag coefficient data collected with each grid is shown to have a greater associated relative uncertainty (U_i/ϕ_i) than its lift counterpart, which is consistent with the sensitivity test results.

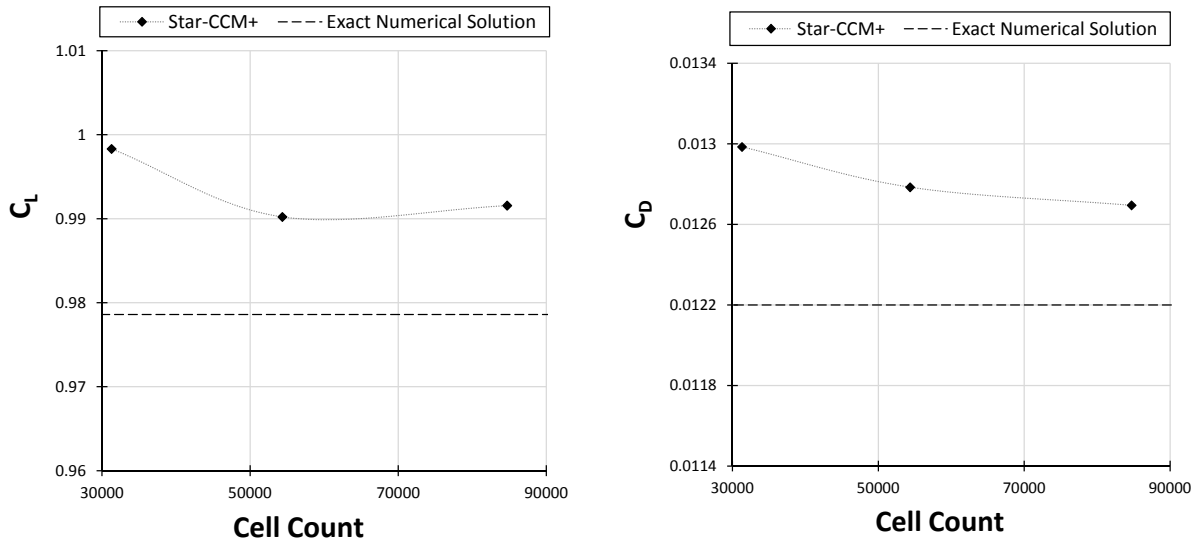

(a) (b)

Figure 4.2: (a) Lift coefficient grid independence; (b) drag coefficient grid independence.

Figure 4.2 shows how the computational results for lift and drag (clearer in the latter) tend converge asymptotically towards the estimated exact numerical solution. When an increased grid refinement does not benefit the solution further within a pre-established threshold, the solution is considered grid independent. During the course of this work, this threshold was set to 1%. In the present case, a grid independent solution was successfully obtained for both considered parameters.

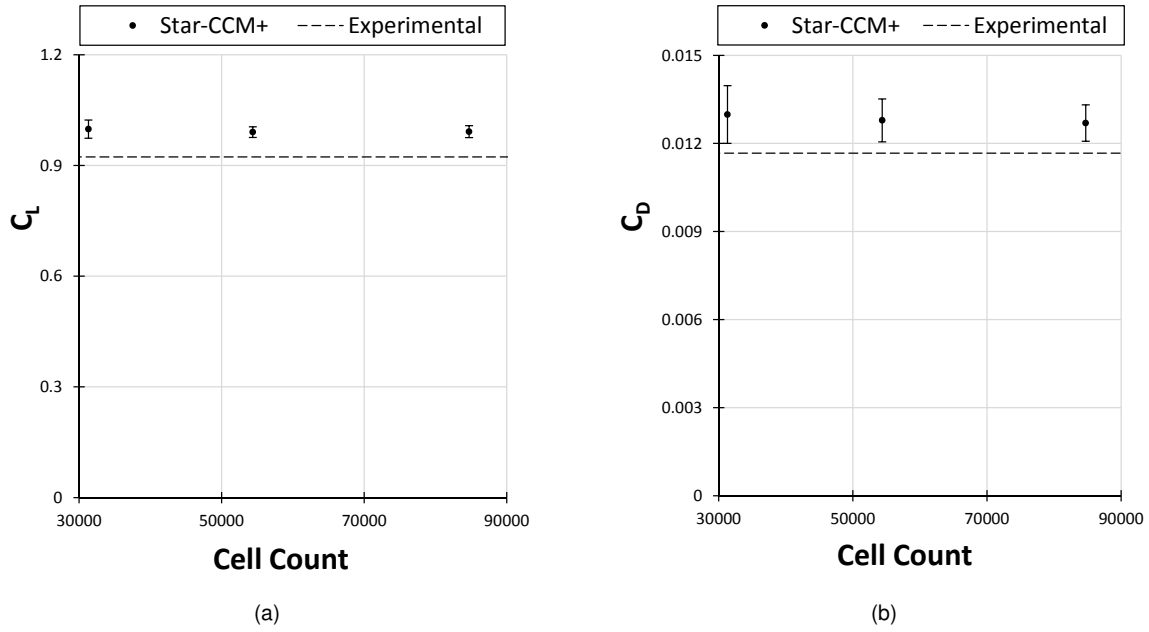

Figure 4.3: Comparison between numerical results and published experimental data: (a) lift coefficient ; (b) drag coefficient.

Figure 4.3 sets the computational results against experimental data from Selig and McGranahan [2004]. It can be seen that the published experimental data lies outside the numerical uncertainty of the computational solutions. However, a good agreement between computational and experimental data was still found. For the medium mesh, the relative deviation to the published experimental data (calculated as $\delta = \frac{\phi_{comp} - \phi_{exp}}{\phi_{exp}}$) is 7.3% and 9.6% for the lift and drag coefficients, respectively.

4.1.3 Aerodynamic Performance Curves

Figure 4.4 and table 4.4 summarize the results for all tested angles of attack, namely, 1° , 3° and 5° . It can be seen that the expected trends for the lift and drag coefficients' curves are closely represented by Star-CCM+ simulation results.

Taking into account the results presented in this figure it is shown that Star-CCM+ predictions for both lift and aerodynamic performance (lift over drag ratio, C_L/C_D) outperform XFLR5 calculations (which, for reference, used the maximum allowed 300 panels). On the other hand, experimental drag results compare more favourably with XFLR5 estimates than those from Star-CCM+. Also, where Star-CCM+ lift coefficient solutions present a relatively constant deviation to experimental data with increasing angle of attack, decreasing only slightly (by 2% over the tested range), drag coefficient correlation worsens considerably. This is typically expected in computational external aerodynamics due to the corresponding

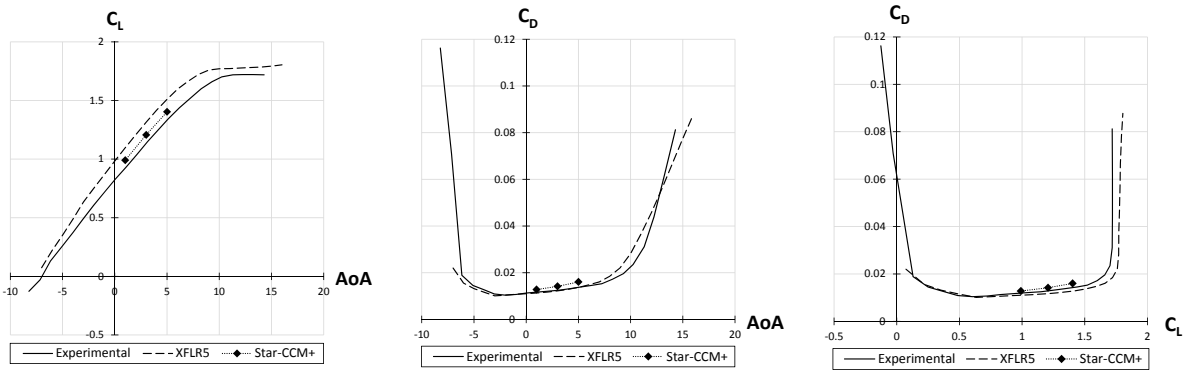

(a) (b) (c)

Figure 4.4: Comparison between numerical results and published experimental data: (a) lift coefficient ; (b) drag coefficient; (c) drag polar.

increase of the pressure drag component.

Table 4.4: Comparison between numerical and experimental results.

AoA	Parameter	Exp. (UIUC)	XFLR5	Star-CCM+
1°	C_L	0.923	18.8%	7.3%
	C_D	0.0117	-2.9%	9.6%
	C_L/C_D	-	22.3%	-2.1%
3°	C_L	1.13	15.9%	6.4%
	C_D	0.0124	-1.8%	13.9%
	C_L/C_D	-	18.0%	-6.6%
5°	C_L	1.33	13.3%	5.3%
	C_D	0.0137	-0.1%	16.8%
	C_L/C_D	-	13.4%	-9.8%

This does not, however, necessarily mean that XFLR5's drag predictions were more accurate. The reason for this statement is that the airfoil used with both numerical methods was a modified version of the Wortmann FX63-137 with a finite trailing edge [Ananda et al., 2012], in order to represent practical limitations in the construction of the wind tunnel models, consistently with the following 3-dimensional benchmark and final application cases. In light of the previous statements, a maximum deviation of less than 3% (absolute value) in XFLR5's drag coefficient predictions is suspicious and should be considered with care, as the numerical uncertainty due to geometry differences is currently unaccounted for in both types of simulation. Even so, XFLR5 does present itself as very computationally efficient tool for simple aerodynamic calculations.

4.1.4 Chordwise Pressure Distribution

In addition to lift and drag coefficient predictions, one of the most relevant computational results for validation purposes in external aerodynamics is the pressure distribution over airfoils. Experimental pressure tap measurements from the MIT Low Turbulence Wind Tunnel [Wo and Covert, 1989], reproduced in figure 4.5, show bumps characteristic of laminar separation bubbles (see also figure 4.10b in

the pressure distribution over both the upper and lower surfaces of the Wortmann FX63-137 airfoil.

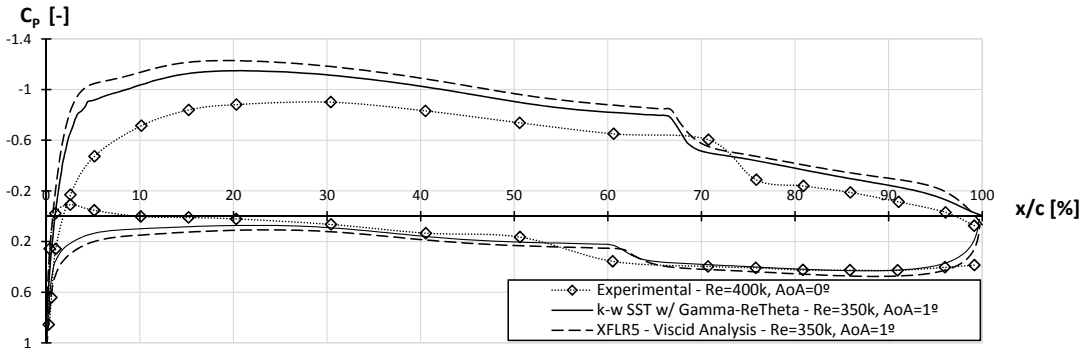

Figure 4.5: Comparison between published experimental pressure coefficient distribution data from pressure tap measurements [Wo and Covert, 1989], Star-CCM+ simulation results and XFLR5 calculations.

Figure 4.5 also shows that both the XFLR5 viscous calculations and the Star-CCM+ simulations with combined turbulence and transition models successful capture the previously stated phenomena. Additionally, it can be seen that Star-CCM+ results co-relate more favourably with the available experimental data. Even so, both numerical approaches present very similar results and, in this sense, cross-validate each other.

The most pronounced differences between the experimental data and the numerical results are the position and size of the laminar separation bubbles. The computational methods anticipate the upper surface LSB, delay the lower surface LSB and appear to slightly under-predict their extent. These deviations may be due to differences in the experimental testing conditions from [Wo and Covert, 1989] and the computational simulations, namely the higher testing Reynolds number of 3×10^5 and the lower angle of attack of $0\,\mathrm{deg}$. In spite of this, the data was still used as reference due to lack of alternative suitable results in the literature.

The small difference in testing Reynolds number should have little effect in the dimensionless pressure distribution profile at the higher end of the LRN regime. The difference in angle of attack should be the most predominant cause for the deviations. This observation is supported by the results presented in figure 4.6. In the context provided by this figure, and extrapolating from it based on visual trends (such as the displacement of the suction peak and LSB bumps with the changing AoA), the pressure tap measurements from figure 4.5 can be expected to co-relate closely with the computational pressure coefficient distribution from a Star-CCM+ simulation with matching a angle of attack.

Also, it is important to note that wind tunnel tests designated as 2-dimensional are, in reality, performed in a 3-dimensional set-up. The main difference is that the finite wing being tested has end-plates on both wingtips in order to lessen the influence of 3-dimensional effects on results, and therefore providing a better approximation to infinite wing (or 2D) conditions. However, in practice, 3D effects can never be fully eliminated nor corrected and, consequently, differences between experimental results published as bi-dimensional and 2D computational simulations (performed in bi-dimensional computational domain) are to be expected.

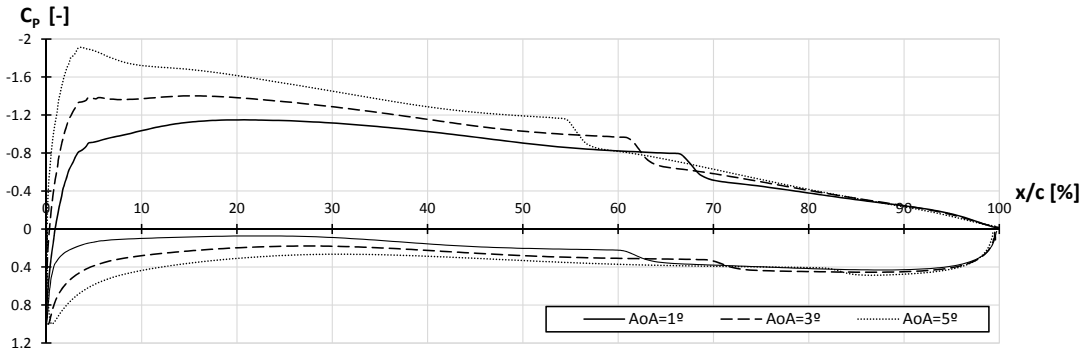

Figure 4.6: Pressure coefficient distribution over the Wortmann FX63-137 airfoil for different angle of attack values from Star-CCM+ simulations.

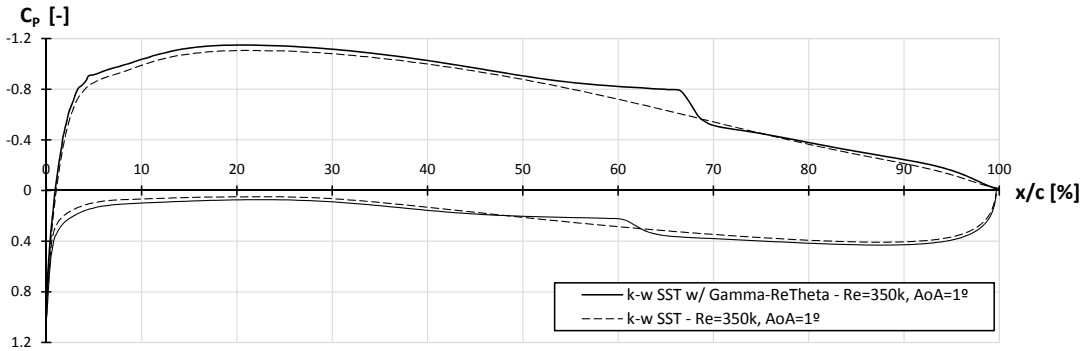

Figure 4.7: Pressure coefficient distribution over the Wortmann FX63-137 airfoil for fully turbulent *(dashed line)* and transition predictive simulations *(full line)*.

Lastly, figure 4.7 illustrates the importance of selecting appropriate turbulence and transition models in CFD. Opting not to use a transition model in this case resulted in failure to predict laminar separation bubbles and, because a fully turbulent flow was assumed (neglecting the presence of laminar flow over the majority of the airfoil), the viscous drag was largely over-predicted, reporting a 41.8% deviation for the drag coefficient against the previous 9.6%. The lift coefficient predictions were not adversely affected, with the deviation actually decreasing from 7.3% to a low 0.8%. However, considering that a visibly different flow is being modelled, this result loses relevance.

4.1.5 Flow Features

Figures 4.8a and 4.8b illustrate the flow around the airfoil for the 1° simulation. The contour plot in figure 4.8a shows how the velocity magnitude varies inside the computational domain, in the vicinity of the airfoil (warmer colors refer to higher velocities). A few features in this figure are worthy of note, namely, the stagnation point in *blue* at the leading edge, the greater flow acceleration in the upper surface in *red*(leading to lower pressures relative to the lower surface, hence its designation as the suction side,

and, consequently, lift), the lower velocity recirculation areas corresponding to the upper a lower surface laminar separation bubbles and the trailing edge turbulent separation (both in *blue*). Figure 4.8b shows mean flow streamlines and one recirculating streamlines in perifery of each LSB. These results are consistent with the previously presented adimensional pressure distribution profiles about the airfoil.

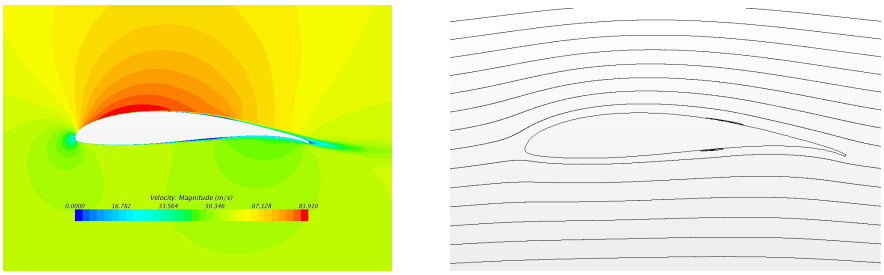

(a) (b)

Figure 4.8: Contour plot of the velocity of the flow field (a) and streamlines around the airfoil (b).

In figure 4.9, flow recirculation occurring at the laminar separation bubbles and trailing edge of the airfoil are represented by streamlines in greater detail. This level of detail in CFD results is unmatched by simpler and less computationally demanding software applications such as the XFLR5.

(a) (b)

Figure 4.9: Detail of recirculating flow regions associated with laminar separation bubbles (a) and trailing edge turbulent separation (b).

Table 4.5 presents a quantitative comparison between published experimental and XFOIL flow feature location predictions from oil flow observations, by McGranahan and Selig [2003], and both Star-CCM+ and XFLR5 simulations performed during the course of this work. This study was limited to the upper surface of the airfoil.

Table 4.5: Comparison between experimental and computational flow feature location results.

	Laminar Separation			**Transition**		**Oil Accumulation**		**Reattachment**			**Turbulent Separation**	
AoA	**Exp. (UIUC)***	XFOIL	Star-CCM+	**XFLR5***	Star-CCM+	**Exp. (UIUC)***	Star-CCM+	**Exp. (UIUC)***	XFOIL	Star-CCM+	**Exp. (UIUC)***	Star-CCM+
1°	**48.7%**	8.6%	7.7%	**66.8%**	-0.3%	**66.0%**	-0.9%	**69.0%**	-1.6%	-0.7%	**98.9%**	0.02%
3°	**44.4%**	7.4%	5.5%	**60.0%**	1.7%	**60.3%**	-0.04%	**62.7%**	-2.5%	0.1%	**98.2%**	0.1%
5°	**40.0%**	6.6%	1.6%	**50.2%**	8.5%	**52.6%**	1.7%	**54.6%**	-5.6%	3.6%	**98.2%**	-0.4%

*Reference values for the location of each feature, as a percentage of x/c, where c is the airfoil chord. The remaining percentages refer to relative deviations.

The most significant deviations between Star-CCM+ results and the remaining sources (experimental if available, XFLR5 otherwise) corresponded to the laminar separation locations at lower angles of attack

and the transition location at the highest. However, whenever both experimental and XFOIL results were available for comparison, the latter was consistently outperformed by Star-CCM+ solutions in terms of deviation against the experimental reference.

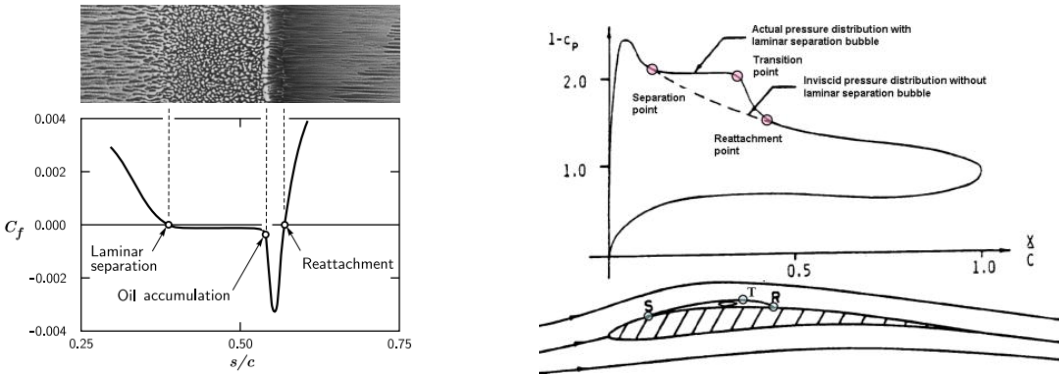

Figure 4.10: Flow feature location from: (a) the skin friction coefficient distribution [McGranahan and Selig, 2003]; and (b) pressure coefficient distribution [Hu and Yang, 2008].

Figure 4.10 ilustrates how computational results can be used to identify different flow feature locations, from skin friction and pressure coefficient distributions.

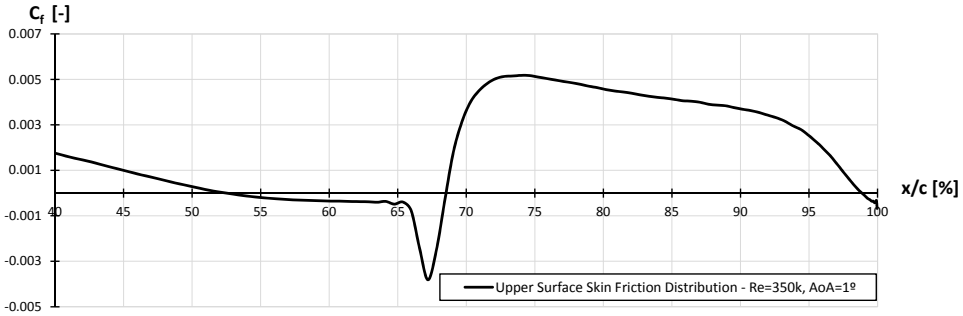

Figure 4.11: Skin friction distribution, over the surface of the Wortmann FX63-137 airfoil, detailing separated flow location and extent (negative values).

In figure 4.11 a plot with the skin friction coefficient distribution over a large section of the airfoil is presented. These computational results collected from Star-CCM+ simulations support the conceptual representation proposed by [McGranahan and Selig, 2003], based on oil flow observations, and reproduced in figure 4.10a – this is seen as a relevant contribution to the scientific community, as at the time of writing, to the author's knowledge, no computational results had yet been published to this end. The most relevant observation to be made refers to the evidence towards the validity of the oil accumulation feature and the following negative spike in the C_f distribution introduced by this representation.

Figure 4.12 provides a visual comparison between Star-CCM+ results for flow feature location and experimental results, the exception being the transition location for which XFLR5 calculations are used as reference due to lack of available experimental data for comparison. This figure omits oil flow location predictions and XFOIL results in order to provide an easier interpretation of the most relevant results in

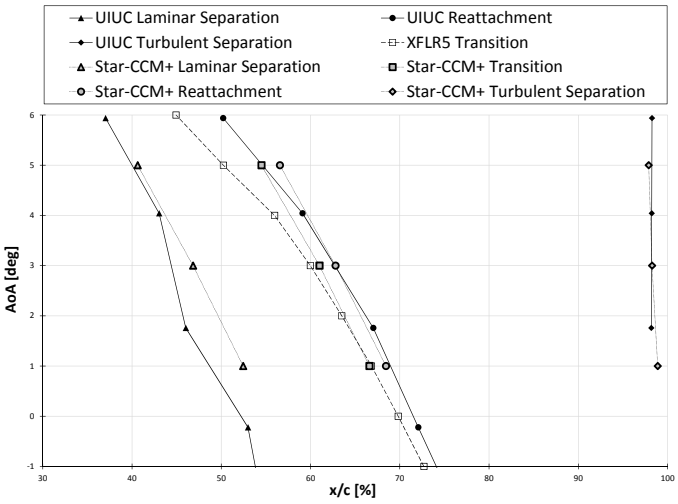

Figure 4.12: Comparison of important flow feature locations between numerical solutions and published experimental data.

the context of this work. However, it was found that the agreement between reported oil accumulation locations and Star-CCM+ predictions is excellent (within 1.7%).

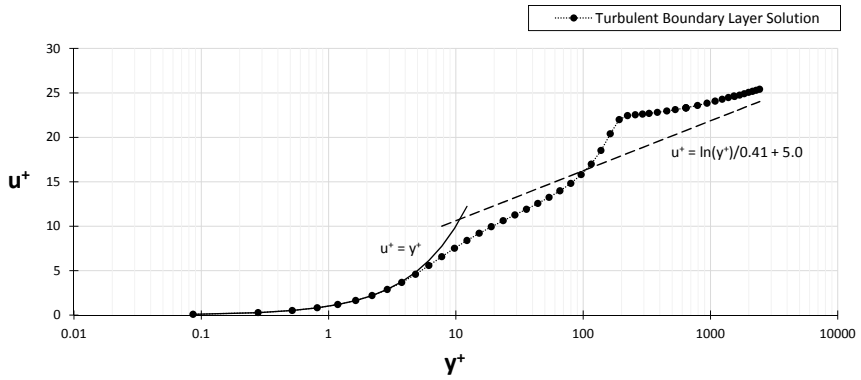

Figure 4.13: Turbulent boundary layer solution from Star-CCM+ simulations superimposed over theoretical turbulent boundary layer approximations, namely for the viscous sublayer (*full line*) and the logarithmic and defect layers (log-law, *dashed line*) [White and Corfield, 2006].

Finally, figure 4.13 is presented in order to demonstrate the suitability of the implemented prismatic layer resolution in resolving the turbulent boundary layer and meeting the turbulence and transition models' requirements. Namely, it is shown that, along a line "probe" placed across a pressure plateau and normal to the airfoil surface, the adimensional velocity profile inside the the turbulent boundary layer is in good agreement with analytical flat plate relations, sufficient grid points (more than 10) have been used under a y^+ of 30 in order to properly resolve the viscous sublayer, and a y^+ distance between the wall and the first grid point near the wall under 0.1, as recommended when working with a transition model.

4.2 3-Dimensional Validation Case

3-Dimensional test case results refer to: grid independence and numerical uncertainty analysis associated with the Star-CCM+ solutions; lift and drag coefficient predictions from both computational simulations and wind tunnel tests; numerical pressure coefficient distributions; and correlation between computational flow patterns and flow visualization wind tunnel test results.

The reference experimental results – collected from wind tunnel tests performed at the Virginia Polytechnic Institute and State University facilities (VPI) – are cited from Marchman et al. [1985] and Marchman and Abtahi [1985]. Additional 3D results from XFLR5 calculations are also presented for comparison purposes.

A summary of specifications for the computational set-up of this validation case is presented in table 4.6.

Table 4.6: Summary of set-up specifications.

Geometry	
Body	Finite wing (3D) of AR=8 with a Wortmann FX63-137 airfoil (semi-span model)
Chord	0.0889 m
Computational Domain	Hexahedral with a symmetry plane
Physics	
Models	k-ω SST (Menter) turbulence with γ-Reθ transition and low y+ wall treatment
Reynolds number	3.0×10^5
Density	1.225 kg/m^3 (ISA-MSL)
Dynamic viscosity	1.789×10^{-5} Pa.s (ISA-MSL)
Inlet velocity magnitude	49.3 m/s
Mesh	
Number of cells	1.3×10^7 (medium grid)
Prism layer resolution	32 layers
Base size	1/10th of the chord
Cell size on the wing surface	12.5%*
Additional local refinement (includes surface and volumetric controls)	Leading edge, trailing edge and wingtip (3.125%*); wingtip vortex (25%*); wake (50%*); and nearfield (100%*)
Maximum Wall Y+	1.5
Average Wall Y+	0.1
Boundary Conditions	
Far-field distance	60 chords (all directions)
Tu (inlet and ambient)	0.01 (1.0%)
TVR (inlet and ambient)	10

* percentage relative to base size.

4.2.1 Grid Independence and Uncertainty Analysis

Figures 4.14, figure 4.15 and table 4.7 present the results for the numerical uncertainty analysis and grid independence tests, similarly to the 2-dimensional test case. These are relative to incompressible

flow simulations performed in Star-CCM+, for an aspect ratio 8 finite wing with a Wortmann FX63-137 airfoil at a Reynolds number of 3.0×10^5 and a 1° angle of attack, using the $k-\omega\ SST$ turbulence model combined with the $\gamma - Re_\Theta$ transition model The considered coarse and fine meshes have a base cell size of 1.5 and 0.75 times the base size of the medium mesh, respectively. The computational domain was design to take advantage of the symmetric flow conditions and therefore cut in half at the symmetry plane.

Table 4.7: Grid independence and uncertainty analysis.

		Coarse Mesh $6.0x10^6$ cells		Medium Mesh $1.3x10^7$ cells		Fine Mesh $2.3x10^7$ cells		Exact Numerical Solution
Parameter	Exp. (VPI)	Deviation	Uncertainty	Deviation	Uncertainty	Deviation	Uncertainty	Deviation
C_L	0.67	12.9%	1.9%	12.0%	0.9%	12.2%	1.1%	11.2%
C_D	0.024	55.0%	4.3%	52.7%	2.6%	52.6%	2.5%	49.6%

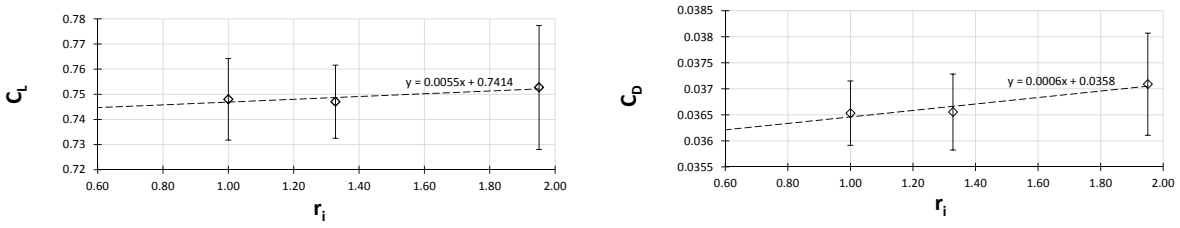

(a) (b)

Figure 4.14: Numerical uncertainty due to discretization for the calculated lift (a) and drag (b) coefficients.

The numerical uncertainty due to discretization associated with drag prediction is once again superior to the uncertainty related with lift. Even so, a grid independent solution within 1% was successfully attained for both lift and drag coefficients.

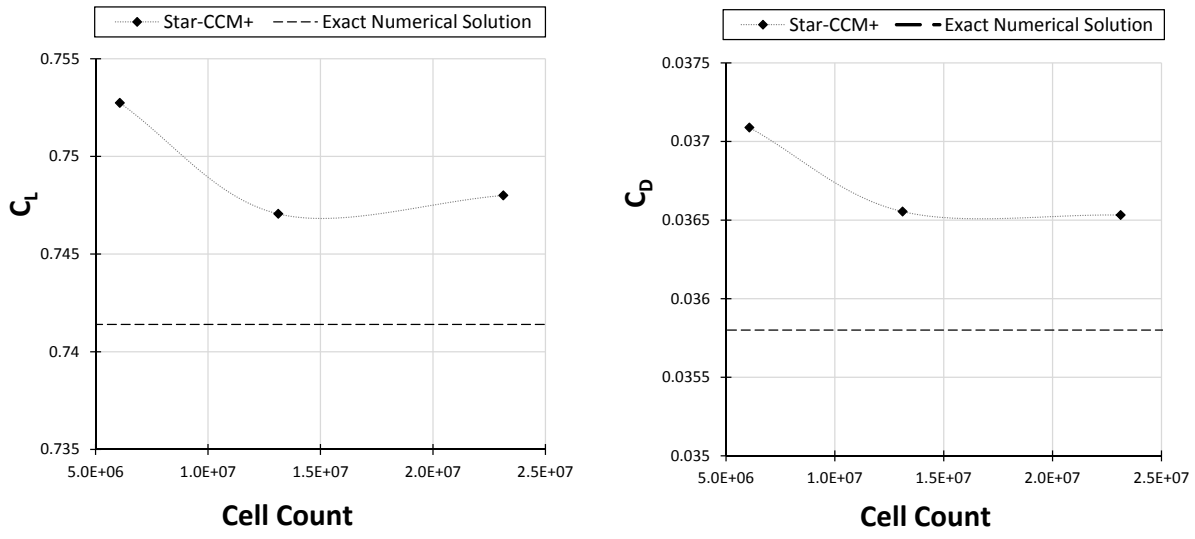

(a) (b)

Figure 4.15: (a) Lift coefficient grid independence; (b) drag coefficient grid independence.

Figure 4.16 sets the computational results from Star-CCM+ simulations against published experimental data from Marchman et al. [1985] and Marchman and Abtahi [1985] and experimental results from wind tunnel tests performed by the author during the course of this work. The latter were performed at the Portuguese Air Force Research Center wind tunnel facilities (LABAER) using a semi-span model and an open test-section configuration with a reflection plane at the bottom. Also, at the time of writing, these results were uncorrected for any wind tunnel effects.

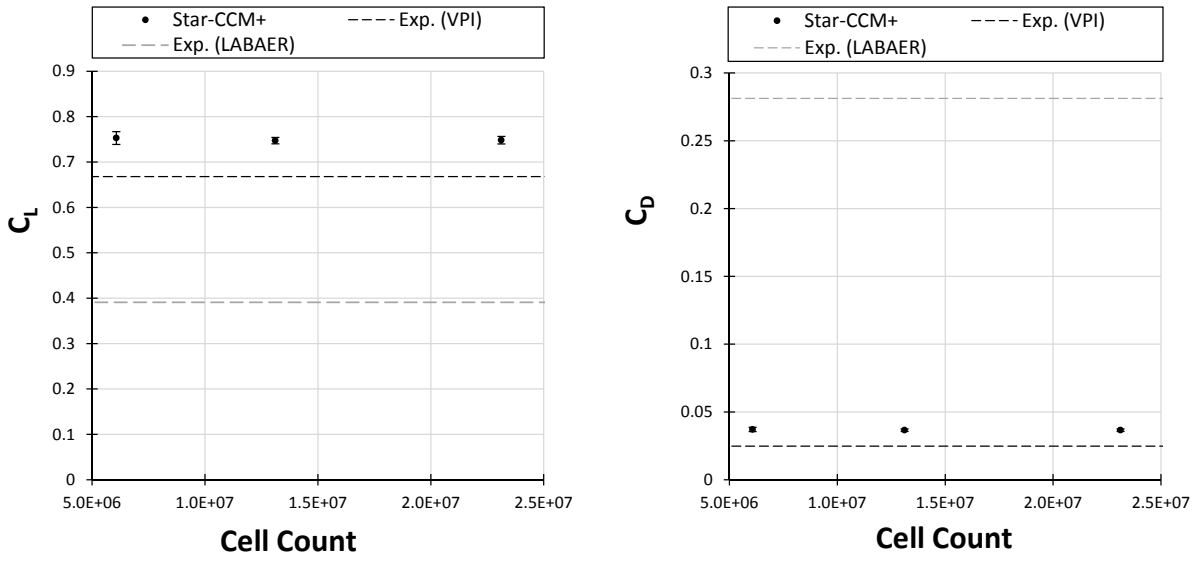

Figure 4.16: Comparison between numerical results and experimental data: (a) lift coefficient ; (b) drag coefficient.

It is clear from these results, uncorrected as they are, that experimental tests performed at LABAER largely under-predict lift and over-predict drag, relative to those from VPI. On the other hand, Star-CCM+ results over-predict both lift and drag coefficients, but correlate more favourably with the published results, although the latter lie outside the computational models' numerical uncertainty. Quantitatively, Star-CCM+ over-predicts the lift and drag coefficients by 12.0% and 52.7%, respectively, with the medium mesh. These deviations are greater than those observed in 2-dimensional simulations, but this is consistent with the literature and was to be expected.

4.2.2 Aerodynamic Performance Curves

Figure 4.17 and table 4.8 summarize the results for all testes angles of attack, namely, 1° , 3° and 5° . In figure 4.17a and c it can be seen that the lift coefficient curve from the published experimental results (VPI) are closely approximated by Star-CCM+ simulation results.

Also in figure 4.17a, experimental data from the performed wind tunnel tests is presented in scatter and approximated by a linear trend curve. This evidences the experimental uncertainty associated with the employed wind tunnel testing technique. It is also shown that, although offset, wind tunnel results successfully capture the expected trend in the linear regime of the lift curve.

However, drag coefficient results from Star-CCM+ do not correlate as favourably with the published data as its lift counterpart. However, it should be noted that both numerical tools (Star-CCM+ and XFLR5) offer very similar results and, in this sense, increase the level of confidence attributable to their predictions. As it did in 2D calculations, XFLR5 proves to be very efficient tool for lift and drag predictions when dealing with simple configurations. In these calculations, 2000 panels were used with the vortex lattice method (VLM), considered the most accurate for most applications [Deperrois, 2009a].

It should also be noted that some uncertainty is also associated with the published experimental results, as even though both cited references provide wind tunnel test results performed by the same authors in the same facilities under supposedly the same testing conditions, there are discrepancies in their results. Namely, a 1.5° offset in angle of attack was found between both lift curves. In light of this, the lift and drag coefficient results published in Marchman and Abtahi [1985] were offset by -1.5° in angle of attack, so that both published lift curves matched, as drag results were not given in Marchman et al. [1985] but its lift curve provided a better correlation. Only the corrected data from Marchman and Abtahi [1985] is used in figure 4.17 and table 4.8.

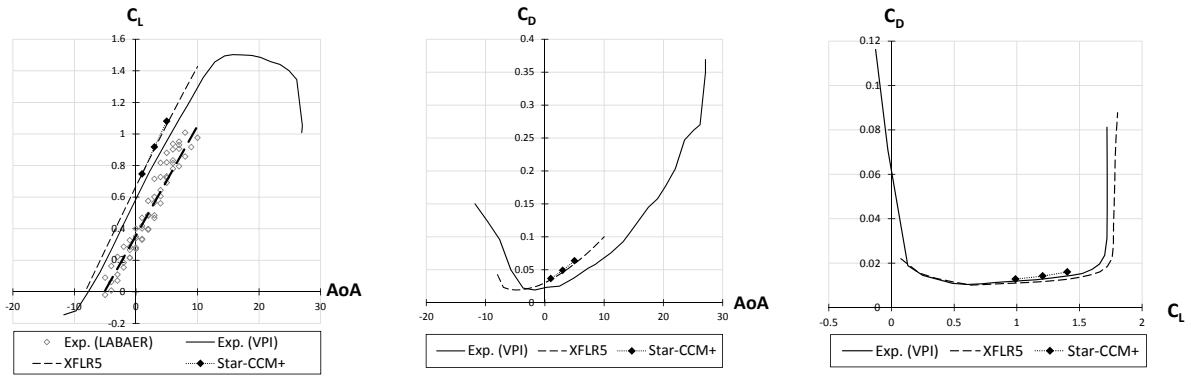

(a) (b) (c)

Figure 4.17: Comparison between numerical results and experimental data: (a) lift coefficient; (b) drag coefficient; (c) drag polar.

Table 4.8: Comparison between numerical and experimental results.

AoA	Parameter	Exp. (VPI)	XFLR5	Star-CCM+	Exp. (LABAER)
1°	C_L	0.67	12.1%	12.0%	-41.4%
	C_D	0.024	45.8%	52.7%	-
	C_L/C_D	-	-23.1%	-26.6%	-
3°	C_L	0.82	10.8%	12.4%	-30.6%
	C_D	0.028	65.4%	76.5%	-
	C_L/C_D	-	-33.0%	-36.3%	-
5°	C_L	0.95	10.9%	13.2%	-19.4%
	C_D	0.0380	55.1%	67.3%	-
	C_L/C_D	-	-28.5%	-32.3%	-

Drag results from the wind tunnel tests performed during the course of this work are not shown in figure 4.17 nor table 4.8. These were found to by greatly inconsistent and presented to high a deviation (figure 4.16) to be considered suitable results. A more detailed study of the probable causes for this should be performed in the future. However, it was found that the six-component balance that equips the

wind tunnel was past its recommended calibration date. Also, during the tests, it was observed that both the test article, a 3D printed semi-span model of PLA reinforced with a carbon tube, and the reflection plane were subjected to a strong vibrations, which could undermine the force measurements. Additional error may have been introduced due to the sizing and placement of the model, i.e. since the model had a small wingspan relative to the height of the test section (with only approximately $0.36m$ against $0.80m$) and was adjacent to the reflection plane, a large portion of the model may have been subjected to both the boundary layer from the reflection plane and the mixing layer from the nozzle of the wind tunnel. Finally, drag force measurements are typically one order of magnitude lower than the corresponding lift force measurements and, therefore, more sensitive to perturbations.

4.2.3 Chordwise Pressure Distribution

Figure 4.18 compares the adimensional pressure distribution over the surface of the wing's central cross-section, i.e. at the symmetry plane, with 2-dimensional computational results from the previously presented 2D simulations and the pressure tap measurements from [Wo and Covert, 1989].

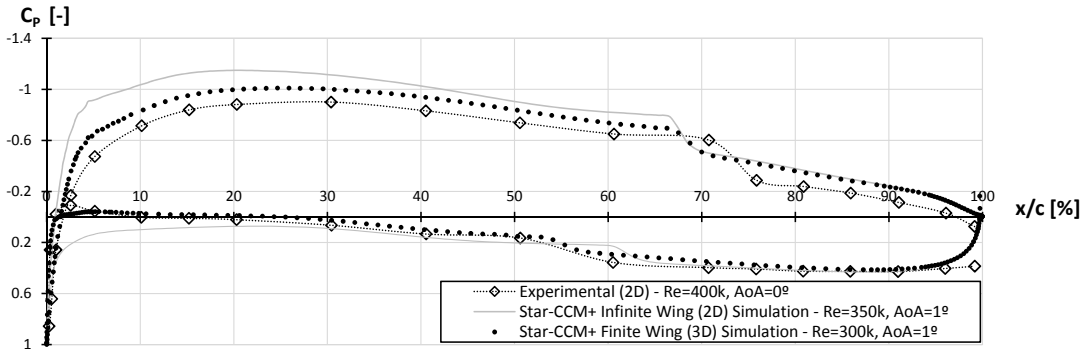

Figure 4.18: Comparison between published 2-dimensional experimental pressure coefficient distribution data from pressure tap measurements (from [Wo and Covert, 1989]) and both infinite wing (2D) and finite wing (3D, from the airfoil section across the symmetry plane) Star-CCM+ simulation results.

This figure shows the 3-dimensional (or finite wing) effects on the pressure distribution over an airfoil section, reducing its effective angle of attack. This is evidenced by a more favourable correlation between 3D results and experimental data [Wo and Covert, 1989] for an angle of attack of 0°, than with 2D computational results for the same nominal angle of attack of 1°.

4.2.4 Flow Visualization

In addition to lift and drag force measurements with a six-component balance, wind tunnel tests for the 3-dimensional validation case also comprised a flow visualization exercise, using the china-clay technique, for the $AoA = 1^\circ$ case. The results are illustrated in figures 4.19 and 4.20.

Figure 4.19 shows an excellent agreement between the china-clay technique results and the computationally attained flow patterns combining skin friction coefficient distribution over the wing surface with

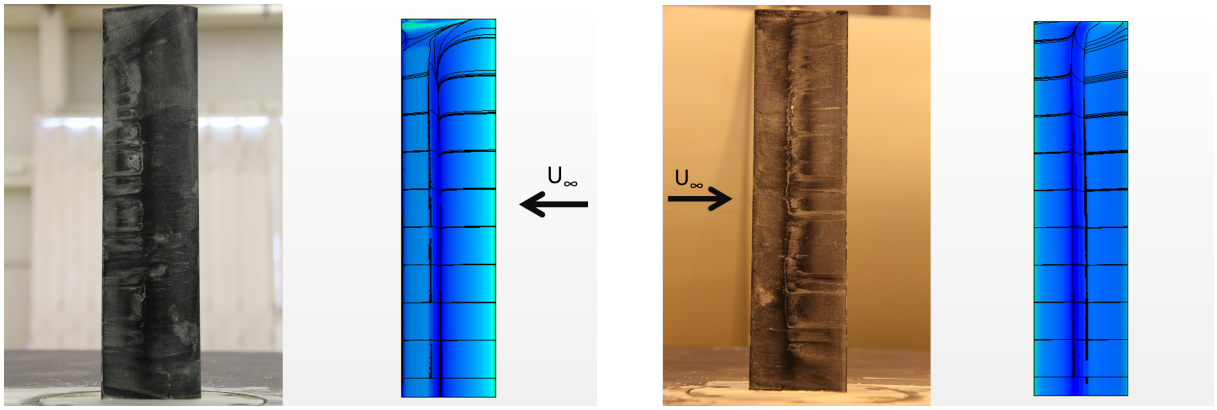

(a) (b)

Figure 4.19: Comparison between china-clay flow visualization wind tunnel results (*left*) and skin friction distribution and near surface streamlines from CFD simulations (*right*) over the upper (a) and lower (b) wing surfaces.

surface adjacent streamlines. In the experimental results, regions clean of china-clay deposits (revealing the black paint of the test article) represent separated flow regions. In CFD simulations the colder colours refer to lower skin friction regions, the dark blue representing separated flow regions, and the streamlines are shown as black.

The first observation to be made is that these results experimentally confirm the occurrence of laminar separation bubbles on both upper and lower surfaces of the wing, validating the use of the $\gamma - Re_{\Theta}$ transition model combined with the $k - \omega$ SST turbulence model. In addition, it can be noted how the computational model successfully captures streamline curvature at the wingtip (*top*) for both the upper and lower wing surfaces, as well as separated flow regions due to the wingtip vortex (at corner of the trailing edge with the wingtip in the upper surface) in agreement with the experimental results.

The main distinction between experimental and numerical results in figure 4.19 is due to the presence of a reflection plane (which is essentially a wall boundary) in the wind tunnel experiment whereas in the CFD simulations a true symmetry boundary condition is imposed. In the pictures from the experimental procedure it can be seen that the china-clay pattern becomes less clear nearer to the reflection plane (*bottom*) and is actually wiped clean due to flow separation in the upper surface (possibly following the airfoil's maximum thickness at 13.7% of the chord).

Figure 4.20 compares in detail the experimental and computational patterns over the surface of the wing. With this level of detail it is possible to identify additional discrepancies and similarities between both types of results. On the positive, it can be seen that both the experimental and computational methods employed are capable of capturing the turbulent separation occurring near the trailing edge in the upper surface. On the negative, it is shown that the location and extent of the laminar separation bubbles are different between techniques. Specifically, the wind tunnel tests appear to anticipate the both LSBs (which appear further downstream in the computational solution) and under-predict their extent.

These differences may be due to higher turbulence levels inside the test section, either due to the mean flow quality or the previously mentioned vibrations of the test article. It can also be due to an

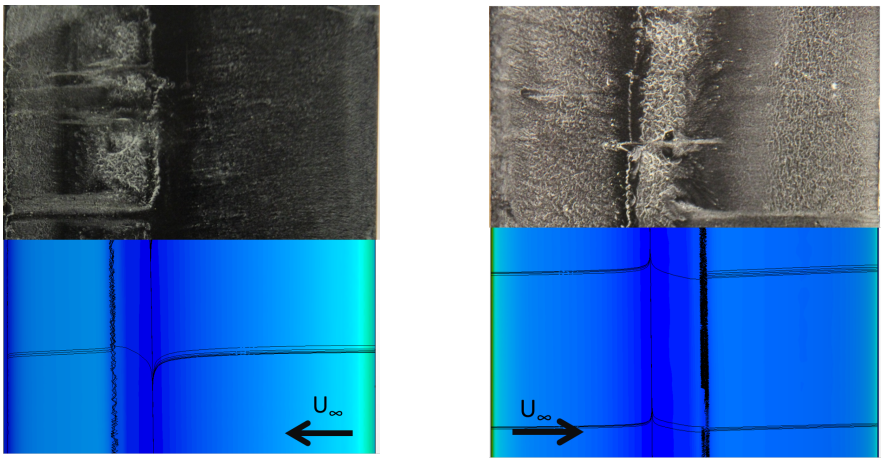

(a) (b)

Figure 4.20: Detail of the comparison between china-clay flow visualization wind tunnel results (*top*) and skin friction distribution and near surface streamlines from CFD simulations (*bottom*) over the upper (a) and lower (b) wing surfaces.

uncorrected experimental angle of attack. Even though the nominal angle of attack for both the experimental test and the CFD simulation is the same (set to 1°) wind tunnel effects during the experimental procedure are likely to cause change the effective testing angle of attack. The same does not occur in the CFD simulation because free stream conditions were considered in its set-up.

In spite of this, the china-clay technique was shown to provide valuable experimental results with application to the efforts of CFD simulations in external aerodynamics.

4.3 ALFA Application Case

The final object of study is the unmanned aerial vehicle ALFA, at cruise conditions, which correspond to a Reynolds number of 4.1×10^5 and a 3° angle of attack.

No published results (neither experimental nor computational) are available for comparison purposes and, due to the complex geometry, XFLR5 calculations are not suitable. The collected results comprise: in-flight angle of attack measurements by a wind-vane type sensor and its calibration curve from wind tunnel tests; grid independence and numerical uncertainty analysis associated with Star-CCM+ solutions; lift and drag predictions from Star-CCM+ simulations and wind tunnel tests performed with a semi-span scale model and an open test section configuration with a bottom reflection plane; adimensional pressure distribution profiles from pressure tap measurements, from both flight and wind tunnel tests, and computational results; and, lastly, flow visualization tests performed in the wind tunnel with the china-clay technique.

A summary of specifications for the computational set-up of this validation case is presented in table 4.9.

Table 4.9: Summary of set-up specifications.

Geometry	
Body	Antex X02 ALFA unmanned aerial vehicle (1:1.8 scale semi-span model)
Chord	0.18 m
Computational Domain	Hexahedral with a symmetry plane
Physics	
Models	k-ω SST (Menter) turbulence with γ-Reθ transition and low y+ wall treatment
Reynolds number	4.1×10^5
Density	1.225 kg/m^3 (ISA-MSL)
Dynamic viscosity	1.789×10^{-5} Pa.s (ISA-MSL)
Inlet velocity magnitude	33.3 m/s
Mesh	
Number of cells	2.2×10^7 (medium grid)
Prism layer resolution	32 layers
Base size	1/10th of the chord
Cell size on lifting surfaces	12.5%*
Additional local refinement (includes surface and volumetric controls)	Leading edge, trailing edge and wingtip (3.125%*); part connection, landing gears and nose (6.25%*); fuselage, boom and wingtip vortex (25%*); wake (50%*); and nearfield (100%*)
Maximum Wall Y+	9.2
Average Wall Y+	0.1
Boundary Conditions	
Far-field distance	60 chords (all directions)
Tu (inlet and ambient)	0.01 (1.0%)
TVR (inlet and ambient)	10

* percentage relative to base size.

4.3.1 Cruise Angle of Attack

Previous to these flight tests, the average cruise angle of attack for the ALFA was unknown. A wind-vane type sensor was developed especially to determine this parameter for wind tunnel and CFD simulations. The angle of attack (AoA) sensor flight tests were successful and the average angle of attack for cruise conditions was found to be 3.2° (with a 1.3° standard deviation).

This result was only possible to obtain after calibrating the angle of attack sensor for fuselage and wing interference effects, by performing dedicated wind tunnel tests. Figure 4.21 shows the calibration curve for the angle of attack sensor, constructed by placing the actual UAV inside the wind tunnel test section at three different positive angle of attack positions and testing each one at cruise speeds.

This figure shows that, if uncorrected by the proposed calibration curve, effectively positive cruise angles of attack would be read as negative by the sensor (whose reference 0° orientation was originally offset to match the geometric orientation of the wing's chord line) during actual flight. This is due to streamline curvature caused by wing and the fuselage effects on the flow near the sensor. The small dimensions of the ALFA would not allow for the angle of attack sensor to be placed anywhere unaffected by these disturbances.

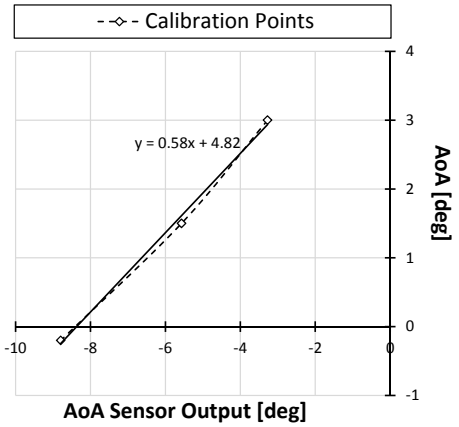

Figure 4.21: Wind tunnel calibration curve correcting for fuselage and wing interference. The reference angle (0°) for the sensor output *(horizontal axis)* is offset to match the geometric orientation of the wingroot cross-section chord line.

Due to time constraints, it was not possible to perform the calibration measurements with the engine turned on and, therefore, propeller effects, if present (and they should be) were thus far neglected.

4.3.2 Aerodynamic Performance, Grid Independence and Uncertainty Analysis

Figures 4.23, figure 4.22 and table 4.10 present the results for the grid independence tests and the numerical uncertainty analysis. The former shows that, once again, there is a greater uncertainty associated with the prediction of drag. However, it should be noted that an atypically high uncertainty is associated with the drag solution in medium grid.

Table 4.10: Grid independence and uncertainty analysis.

		Coarse Mesh		**Medium Mesh**		**Fine Mesh**		
		$1.0x10^7$ cells		$2.2x10^7$ cells		$4.0x10^7$ cells		**Exact Numerical Solution**
Parameter	Exp. (LABAER)	Deviation	Uncertainty	Deviation	Uncertainty	Deviation	Uncertainty	Deviation
C_L	0.48	60.4%	2.2%	59.4%	1.4%	59.1%	1.2%	57.6%
C_D	0.097	-40.3%	4.6%	-40.6%	4.0%	-41.6%	2.0%	-42.5%

In fact, for this final case, a grid independent drag solution within 1% was not successfully achieved in the medium mesh, which helps explain the increased uncertainty. The discrepancy between medium and fine mesh drag predictions was traced to a small geometric detail in the fuselage which was not explicitly removed, and was only captured with the most refine grid. Also, it is important to note that the experimental reference for grid independence assessment are results from wind tunnel test runs performed during the course of this work, instead of published results, to which additional uncertainty may be attributed.

In spite of this, it is still shown in figure 4.23 that the lift and drag predictions for the different grids are converging with increasing refinement towards the estimated exact numerical solution of the computational model. This trend, however, does not benefit the correlation between Star-CCM+ simulation and

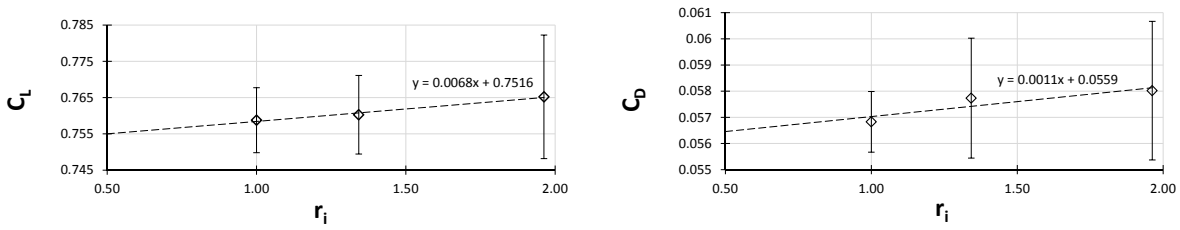

(a) (b)

Figure 4.22: Numerical uncertainty due to discretization for the calculated lift (a) and drag (b) coefficients.

wind tunnel test results, increasing the deviation between drag predictions (table 4.10).

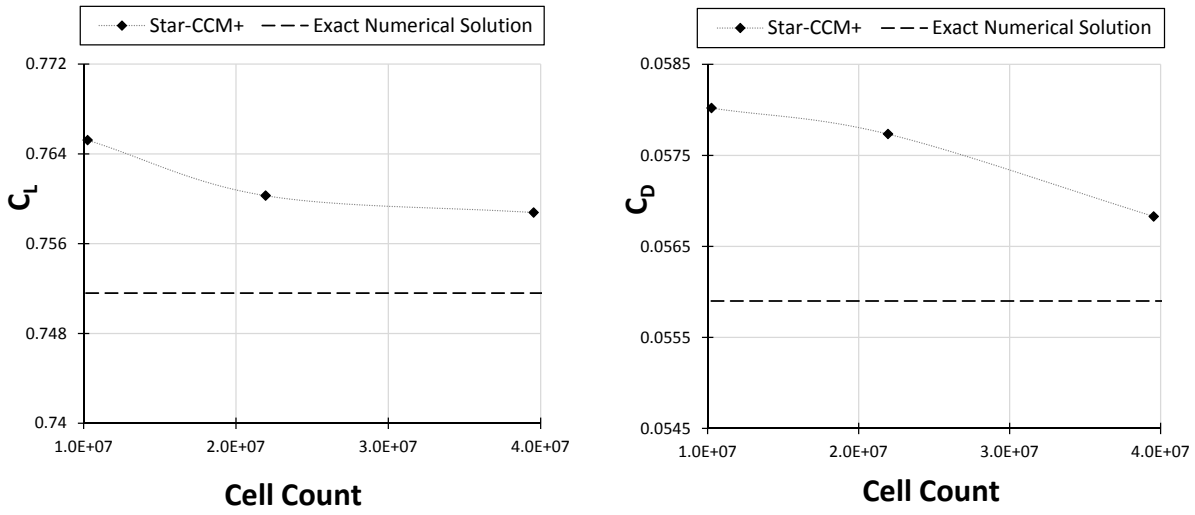

(a) (b)

Figure 4.23: (a) Lift coefficient grid independence; (b) drag coefficient grid independence.

Figure 4.24 compares the computational and wind tunnel results. As in the 2D and 3D test cases, the experimental results are outside the numerical uncertainty bounds of the computational model. However, the six-component balance measurements consistently under-predicted lift and over-predicted drag, and the latter with a significant decrease in deviation relative to computational results, when compared with the 3-dimensional validation case.

4.3.3 Chordwise Pressure Distribution

The adimensional pressure coefficient profiles presented in figure 4.25 were obtained from pressure tap measurements installed in the scale model, performed with two different sets of sensors and acquisition systems, and Star-CCM+ results, at the same spanwise positions (48.7%).

The *pressure scanner* is a professional equipment, whereas the *data acquisition system* is a small, portable and inexpensive equipment developed during the course of this work to be used in UAV flight testing, essentially using miniaturized pressure sensors and low-cost electronic components.

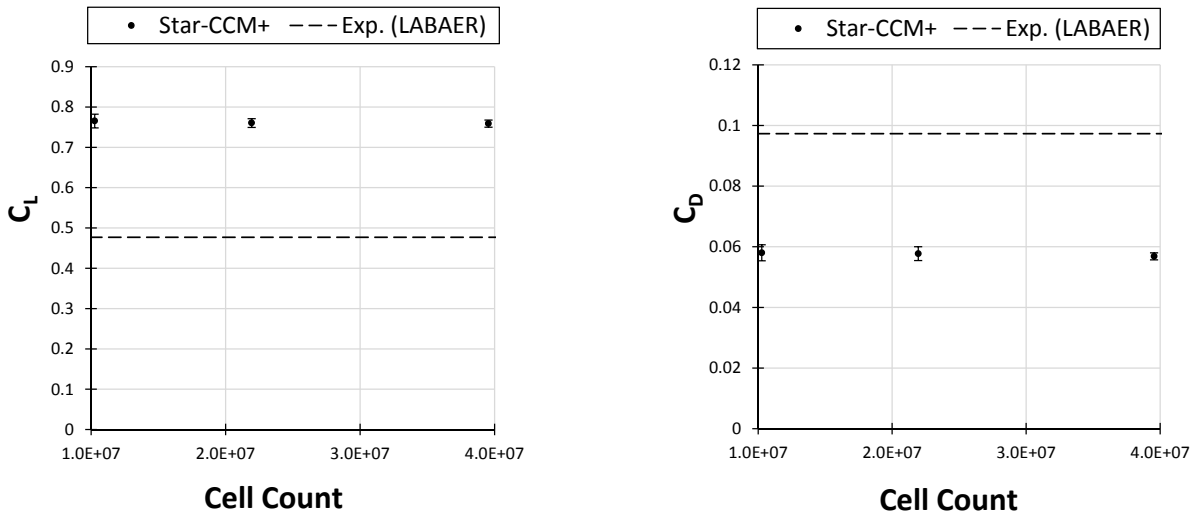

Figure 4.24: Comparison between numerical results and experimental data: (a) lift coefficient ; (b) drag coefficient.

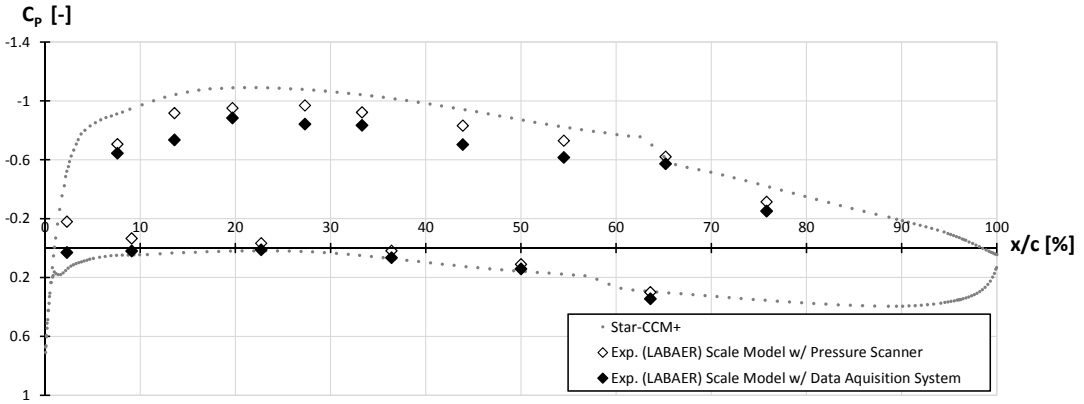

Figure 4.25: Pressure coefficient distribution from wind tunnel scale model pressure tap measurements, from two different equipments, and Star-CCM+ simulations at 48.6% of semi-wingspan.

Figure 4.25 shows that both equipments provide very similar results, even though those given by the pressure scanner correlate slightly better with the computational results. The data acquisition system's limitations appear to be in the suction side of the wing, under predicting the negative pressure coefficients. On the pressure side of the wing, however, most of the measurements are actually an improvement on those from the pressure scanner, even if only by a small amount.

Another relevant observation refers to the pressure taps themselves, namely their limited quantity and forward distribution (towards the leading edge). This lack of resolution towards the trailing edge is restrictive to result interpretation as not enough experimental point information is available to understand, for example, if the transition bump was captured any of the systems. This was due to practical manufacturing constraints, namely, limited wing thickness near the trailing edge.

Figure 4.26 replaces the results from the pressure scanner with results from the data acquisition system installed in the actual UAV, placed and fixed inside the wind tunnel test section, with the engine

turned on and at cruise speed. Pressure tap location in the actual wing is identical to that of the scale model. This procedure was performed as a ground check to the data acquisition system before the flight tests. The readings are very similar to those from the scale model. In fact, some of the readings offer an improvement on the measurements performed with the scale model, when set against the computational data. The discrepancies between both experimental profiles are most likely due to geometric differences between the scale model and the actual UAV's wing, as well as differences between corresponding pressure taps. The exceptions to this are the pressure coefficient readings at the pressure tap placed in the wing's upper surface at 27.3% of its chord which was traced to an installation defect, since corrected.

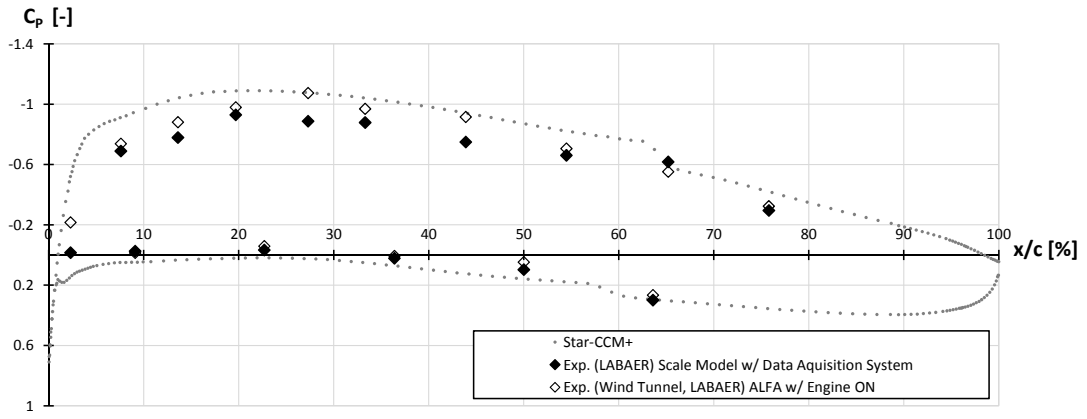

Figure 4.26: Pressure coefficient distribution from pressure tap measurements with the data system, both from the scale model and the actual UAV (placed inside the wind tunnel test section), and Star-CCM+ simulations.

Finally, figure 4.27 shows the pressure distribution profile collected during flight, sampled from a levelled flight segment out of the complete flight circuit, under ideal weather conditions. It is clear that it correlates poorly with the remaining data, especially in the upper surface. Probable causes behind these results are the instability and unsteadiness of the actual flight, even when attempting a levelled flight, due to the UAV's small size and weight and low speed, and pressure sensor hysteresis, which was detected in wind tunnel tests but found, in those conditions to be negligible. In flight however, larger pressure variations due to additional changes in altitude (flight tests were performed up to $1800ft$), may have exacerbated these adverse effects.

4.3.4 Flow Visualization

The semi-span scale model of ALFA was also submitted to china-clay flow visualization tests. Presently, only the wing pattern will be studied. Figures 4.28 and 4.29 show, an excellent agreement between computational and experimental results, with both methods successfully capturing streamline curvature near the wingtip and separated flow regions associated with laminar separation bubbles, cross-validating one another.

Figure 4.30 shows both the computational and experimental patterns in greater detail. This figure shows an improved agreement in upper surface experimental LSB location and extent when compared

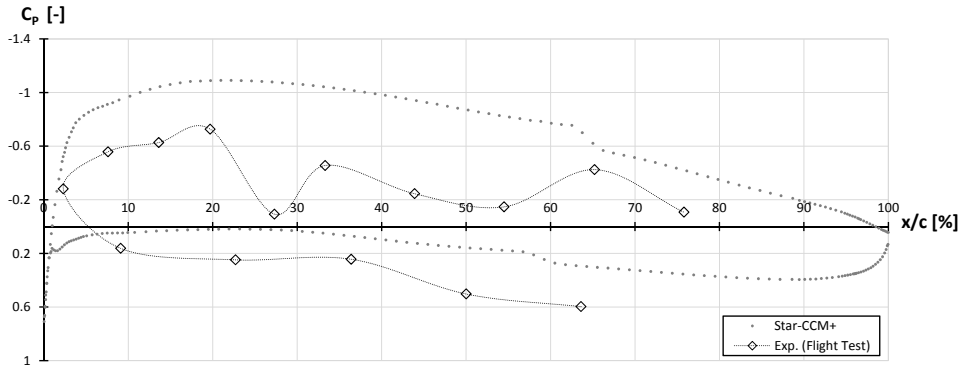

Figure 4.27: Comparison between the typical in-flight pressure coefficient distribution profile (collected with the data system and relative to a randomly selected levelled flight segment of the testing circuit) and Star-CCM+ results.

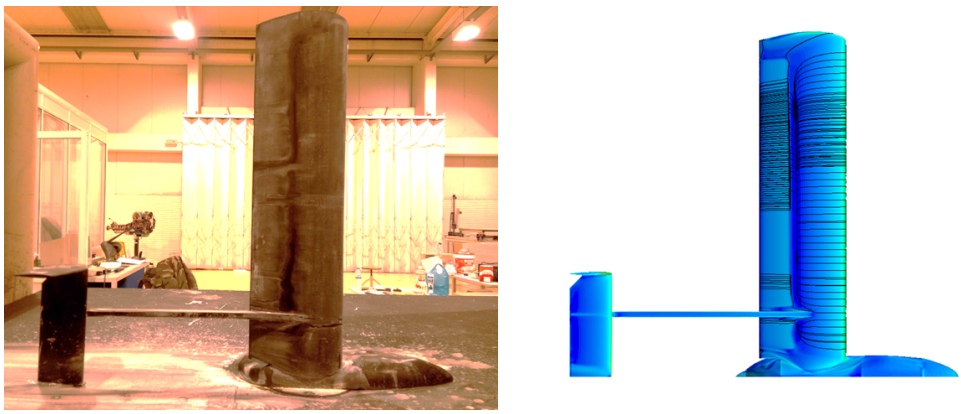

Figure 4.28: Comparison between china-clay flow visualization wind tunnel results (*left*) and skin friction distribution and near surface streamlines from CFD simulations (*right*) over the upper wing surface.

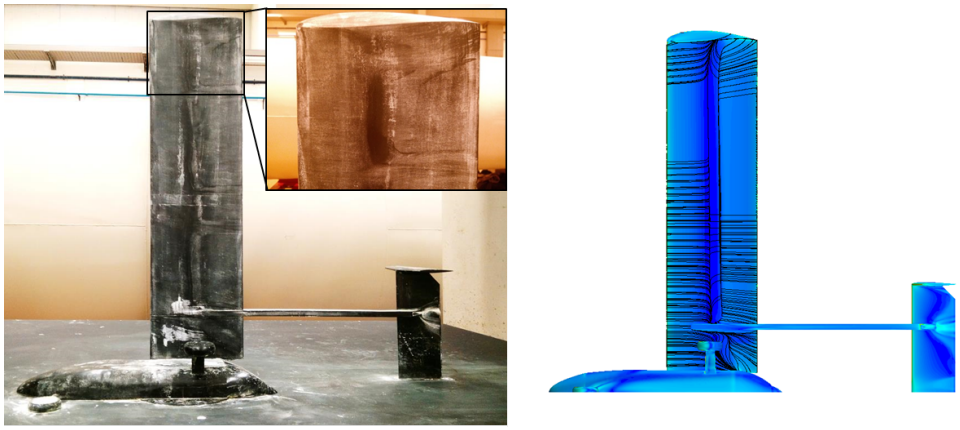

Figure 4.29: Comparison between china-clay flow visualization wind tunnel results (*left*) and skin friction distribution and near surface streamlines from CFD simulations (*right*) over the lower wing surface.

with the 3-dimensional test case results. In the lower surface, however, the LSB is still significantly antecipated relatively to computational results, even though its extent appears to be very similar.

Once again, the inexpensive, fast and practical china-clay flow visualization technique contributed with valuable data that support CFD simulations results and the computational methodology behind them, and may be considered as an useful qualitative, though accurate and detailed, validation exercise.

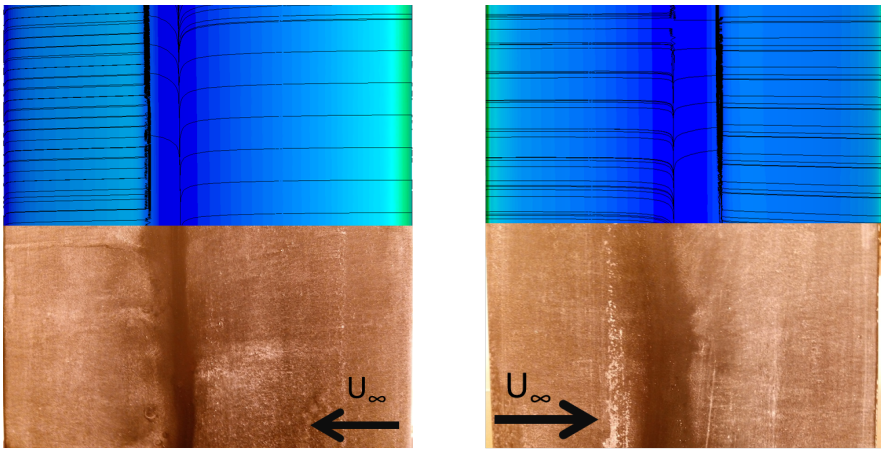

(a) (b)

Figure 4.30: Detail of the comparison between china-clay flow visualization wind tunnel results (*bottom*) and skin friction distribution and near surface streamlines from CFD simulations (*top*) over the upper (a) and lower (b) wing surfaces.

This concludes this dissertation's chapter on results.

Chapter 5

Conclusions

At the outset, this document presented an extensive and detailed literature review of fundamental concepts related to computational simulation and experimental testing in external aerodynamics, particularly for the low Reynolds number (LRN) regime, characteristic of unmanned aerial vehicles (UAV) operations. Most of this overview was focused on computational fluid dynamics (CFD) and wind tunnel testing techniques and provided the necessary background in order to identify recommended practices in numerical simulations and experimental validation procedures, based on CFD and aerospace industry recommendations, to assist in small unmanned aerial vehicles design in the context of the Portuguese Air Force (PrtAF).

During the course of this work, these best practices were determined and applied to increasingly complex problems, starting with simple airfoil (2D) and finite wing (3D) simulations, until an external aerodynamics CFD computational model for a complete UAV configuration could be set-up and tested with confidence and validation. The guidelines are summarized for future consultation in the Appendix A.

The computational simulations were performed with Star-CCM+ and the results, whenever possible, were compared with published experimental or numerical data and additional XFLR5 calculations. The experimental validation efforts comprised both wind tunnel and flight tests.

XFLR5 proved to be an useful tool due to its low computational cost, fast calculations and good performance for simple LRN flows. It cannot handle complex geometries and the results it provides are limited. However, it is very useful to use as reference (for data correlation) during preliminary CFD simulations.

The wind tunnel tests provided useful experimental validation data, from successful pressure tap measurements and china-clay flow visualization tests. The former, although successful, required a larger (but not prohibitive) amount of time and care during the installation process. The latter proved to be a very economical and practical qualitative testing technique with excellent correlation with computational results. However, balance measurements largely under-predicted lift and over-predicted drag. No wind tunnel corrections were applied to these results, which may have exacerbated these discrepancies. Also, the reflection-plane and semi-span model testing technique may require improvement, as strong

vibrations often occur on both model and reflection-plane during testing, with possible contact between them and consequent transmission of loads.

The scaled wind tunnel model parts were 3D printed, successfully exploring the potential of this rapid prototyping technique for wind tunnel testing, reducing model construction time, effort and specialized personnel requirements. This technique allows for part connections to be modelled and printed for simpler assembly, as well as internal details for sensor embedding or structural reinforcements. However, 3D printing proved difficult to master, and was more time consuming than expected, with frequent malfunctions delaying progress. But, in the end, a dimensionally accurate model with a smooth surface finish and adequate mechanical resistance was attained.

The pressure reading component of the developed Data Acquisition System provided good results during the wind tunnel testing stage compared to a professional pressure scanner, with good measurements on the pressure side of the wing, but slightly under-predicting pressure coefficient values on the suction side of the wing. This demonstrates the value of current low-cost and miniaturized electronics to modern aerodynamic testing. However, it did not provide accurate readings during flight. This is believed to be related with the natural unsteadiness of real flight and sensor hysteresis.

Flight testing of the developed AoA sensor revealed an average cruise angle of attack of 3.3° , which compares favourably with the initial guess of 3° used in setting up the final CFD simulations and wind tunnel tests. This wind-vane and Hall Effect based sensor was calibrated with wind tunnel testing procedures for wing and fuselage interference, but propeller effects were not accounted for.

Converged, grid independent computational solutions within 1% were successfully obtained for both the 2D and the 3D validation models. The same did not occur in the final application case, most likely due to a small geometric detail (CAD defect) which was only captured by the most refined grid tested.

The 2-dimensional simulation results were in excellent agreement with published experimental data and XFLR5 results. Sensitivity tests proved local grid refinement controls, computational domain size and inlet turbulence specifications to have a significant impact on results, especially over drag predictions. 3-Dimensional simulations showed good qualitative agreement with wind tunnel experiments, namely, by comparison of the streamline and skin friction patterns on the surface of the wing in CFD against china-clay flow visualization results from wind tunnel tests.

For the final application case, CFD streamline and skin friction patterns were once again in excellent agreement with china-clay flow visualization results. Also, the experimental pressure tap measurements compared favourably with computational results.

Computational fluid dynamics simulations of external aerodynamics problems for low Reynolds numbers flows, taking advantage of steady, incompressible and symmetric flow conditions, enables successful CFD simulations of complete UAV configurations at cruise conditions with less than 40 million cells, providing just as many data points, with valuable engineering information. The RANS equations with the $k-\omega\ SST$ turbulence and $\gamma-Re_{\Theta}$ transition models, and a low y^{+} wall treatment, proved to successfully capture experimentally observed flow features with accuracy. The poor, though consistent, correlation between computational and wind tunnel integral quantity results (such as lift and drag coefficients) are believed to be due to problematic experimental conditions and lack of wind tunnel corrections.

Chapter 6

Future Work and Recommendations

Research and work developed during the course of this dissertation raised numerous questions regarding external aerodynamics simulation, both with computational and experimental approaches, that could not be fully answered due to practical time constraints. In this closing chapter, further studies are recommended to address this issues for the Portuguese Air Force Academy Aeronautics Laboratory, in agreement with current state-of-the-art standards.

Firstly, if effective and efficient wind tunnel testing capabilities are to be attained, the staff should be trained to handle the currently available equipment and data reduction tools. Additionally, these should be kept up-to-date and calibrated.

In spite of its limitations, classical wind tunnel corrections offer the fastest route to estimating tunnel-to-flight scaling effects, and its implementation should be made systematically by means of an auxiliary program – which should be developed – already fitted to the facility's characteristics and requiring only the input of specific test conditions for the case at hand.

However, the use of CFD simulation to complement and even in some ways improve on wind tunnel testing is the current state-of-the-art practice in the aerospace industry. Although not yet a definitive solution to the subject of wind tunnel to flight scaling, CFD tools solving the Reynolds Averaged Navier-Stokes equations present themselves as an efficient option in assessing wind tunnel correction requirements. These simulations can also provide its own correction factors, directly applicable to the parameters of interest, such as the lift and drag coefficients, by taking the difference in results between a free-flight simulation and another featuring the same test model placed in the test section of the wind tunnel with the appropriate representative boundary conditions set, and using it to correct the wind tunnel's test data.

In this sense the present work serves as a first step towards building a computational framework which allows the practice of this straight-forward approach to the determination of appropriate wind tunnel corrections at the AFA Research Centre facilities through CFD simulation, by setting the guidelines for free-flight simulation of small UAVs. The computational simulation of wind tunnel flows is a separate problem, to which most of the followed procedures will apply, with the addition of several new concerns relating to a more complex computational domain and boundary condition. Further study should be

performed on this very relevant topic, for which recommended reading has already been presented.

Simulations for a wider angle of attack should be computed, in order to evaluate limitations of the proposed methodology. Due to the use of hexahedral cells, it is expected that the performance of the computational model deteriorates for higher angles of attack, when flow direction around the lifting surfaces will be significantly deviated from main grid lines. It is expected that a polyhedral cell grid on a bullet shaped or spherical computational domain would provide improvements in implementation when testing for a wide range of angle of attack flows, and in result accuracy at higher angles of attack. These simulations are useful when studying the entire flight envelope, instead of cruise conditions, and determining stall behaviour. For a complete longitudinal characterization of the aircraft, acquiring pitching moment data is also recommended, unless only the aerodynamic performance, as defined by the relation L/D, is of interest.

Further improvements on meshing should implement the previously introduced concept of adaptive mesh refinement techniques for automatic local refinement in critical regions with steeper gradients, and anisotropic mesh refinement techniques that take advantage of the preferred orientations of different flow features (e.g. greater longitudinal refinement should be privileged over the lifting surfaces and greater transversal refinement should be used in regions affected by wingtip vortices). Additionally,adjoint-based mesh refinement techniques show great promise for optimization of grid point distributions [Fidkowski and Darmofal, 2011].

The performed wind tunnel tests were limited to use of the open test section. Tests should be performed with a close test section to, at the very least, evaluate the practical magnitude of discrepancies between both configurations. Also, in reference to the subject of computing wind tunnel corrections through the use of CFD, while not neglecting the motivations behind the choice of an open test section for these exercises (expressed in Chapter 3), a computational simulation where the wind tunnel geometry is explicitly defined may be arguably simpler to set-up for a closed test section, mainly due to computational domain and boundary condition simplifications, i.e. an open test section is more exposed to diverse and less controllable outside influences that a closed test section, which is, in this regard, favourably more isolated.

Another relevant subject concerns alternative semi-span wind tunnel testing techniques through the use of different model configurations, other than the most typical reflection plane geometry, in which the half-model is precisely half of the full span model, as if cut by its symmetry (or longitudinal) plane. Studies such as Eder et al. [2006] investigate the effect of these configurations on the aerodynamic coefficients and their co-relation with full-span tests of the same aircraft model. Results have shown, for example, that it is beneficial to leave a gap between the model and the wall, with the optimal gap size relating to the displacement thickness of the tunnel wall (onto which the model is mounted) boundary layer in front of the fuselage. This topic directly applies to the long term objective developing best practices in wind tunnel aerodynamics, even if only for validation of computational data, and additional study is recommended. Additional literature on the subject is presented in Milholen et al. [1996], Gatlin and McGhee [1996] and Marchman [1998].

As duly expressed before, error and uncertainty assessment is a very important component of all

testing, both computational and experimental. For the intended purposes, and due to time constraints, only a general overview of this subject was performed, for awareness. However, the definition of uncertainty estimation strategies, as well as the establishment of strategies for reduced uncertainty, should be an integral part of a set of best practice guidelines for computational simulation and experimental validation. Recommended reading on this subject is given in Mendenhall et al. [2006], Roache [1997] and Stern et al. [1999].

The most relevant modern technology for experimental validation of CFD simulations of external aerodynamics flows encountered during the course of this work is the Pressure Sensitive Paint (PSP). Pressure sensitive paints represent a very promising practical alternative to pressure tap installation and measurements, both in costs (when compared to high-end aerospace industry level models) and resolution, providing instant quantitative pressure information over the entire coated surface of a model, making for very easy co-relation with computational results. For this reason, PSPs should be considered for future endeavours in wind tunnel testing. However, due to the present lack of adequate auxiliary equipment at the research facility and experience from personnel in dealing with this tool, which increases the initial investment, the option was dismissed for the present time.

Flow visualization techniques proved to be of very practical implementation, at very low costs, while still providing useful validation data. It is recommended that further studies of this nature are performed. In the wind tunnel, flow visualization tests, so far, have been constrained to the main wing. It is advisable that the fuselage and tail sections undergo a similar analysis. Also, some of the techniques introduced in Chapter 2 are applicable to flight testing, and this too would be of great value towards acquiring effective validation data for computational simulations and wind tunnel experiments.

Finally, it is recommended that a set of recommended practices in 3-D printing directed towards wind tunnel model preparation are fully developed. This effort was initiated with this project, with a substantial amount of ground work laid out by the undergrad student João Vieira during the course of his summer internship, and, given the demonstrated usefulness and practicality of this technology, it should be concluded. Preferably, an additional investment should also be made on equipment of this nature, with the acquisition of a professional level 3-D printing tool, specifically designed to produce high-fidelity models and to be less susceptible to failure due to the faulty functioning of lower quality components of entry level 3-D printers. This will also reduce the required amount of supervision during manufacture, increasing overall productivity. 3-Dimensional scanners are also available that allow to account for dimensional uncertainties of wind test models and can be used to provide a better agreement between experimentally tested and computationally simulated representations.

In summation, there is still a long way to go where the practical application and usefulness of concepts introduced during the course of this work is concerned. Modern times, along with associated technological advances are re-shaping the landscape of roughly century old experimental external aerodynamics practices, reducing wind tunnels into a tool complementary of computational techniques, but not entirely replacing its valuable close relation with reality, and therefore not entirely eliminating the need for such facilities in the aerospace industry. In contrast, CFD has become a mature technique for aerodynamics studies over the last few decades, providing great insight at lower costs and with

lower effort, when compared to traditional testing techniques. Also, the dissemination of miniaturized low cost electronics and open-source software in these modern days has contributed to a variety of improvements to both experimental and computational methods. In an institution whose efficiency and efficacy is heavily dependent on its relationship with technology, a continuous and systematic review of the current state-of-the-art is required and, whenever promising developments with application for the PrtAF arise, its implementation should be swift, as if reflecting the fast pace of the constantly changing times. The present document aims to provide a new solid starting point for future endeavours in external aerodynamics for a modern Portuguese Air Force invested in unmanned aerial vehicle research and development with complementary computational and experimental methodologies, as per the current best practices guidelines of the industry.

Bibliography

Aeronautical Testing Service, Inc. CFD and wind tunnel testing: Complementary methods for aircraft design. 2010.

AFA. Manual D.3.3 Manual do Sistema UAV Antex X02. Technical report, PITVANT, Portuguese Air Force, 2012.

R. Agarwal. Computational fluid dynamics of whole-body aircraft. *Annual Review of Fluid Mechanics*, 31(1):125–169, 1999.

T. Amer, C. Obara, and T. Liu. Quantifying the effect of pressure sensitive paint on aerodynamic data. *AIAA Paper*, 3951:21, 2003.

G. K. Ananda, P. Sukumar, and M. S. Selig. Low-to-moderate aspect ratio wings tested at low Reynolds numbers. *AIAA paper*, 3026, 2012.

J. D. Anderson Jr. *Computational fluid dynamics: the basics with applications*. McGraw-Hill, Inc., 1995.

A. Baltazar, J. Nogueira, and R. Carvalho. Caracterização do escoamento do túnel aerodinâmico da Academia da Força Aérea Portuguesa. Instituto Superior Técnico, Universidade Técnica de Lisboa, 1997.

J. Bardina, P. Huang, and T. Coakley. Turbulence modeling validation. *AIAA paper*, 2121:1997, 1997.

J. B. Barlow, W. H. Rae, and A. Pope. Low speed wind tunnel testing, 1999.

A. Barros. Centro de Investigação, Desenvolvimento e Inovação da Força Aérea - Projectos de Investigação e Desenvolvimento. Briefing, 2015.

A. Barros and G. M. Gonçalves. Projecto de Investigação e Tecnologia em Veículos Aéreos Não-tripulados - Relatório Final de Projecto. Briefing, 2015.

T. J. Bencic. Pressure-sensitive paint measurements on surfaces with non-uniform temperature. 1999.

M. Brendel and T. Mueller. Transition phenomena on airfoils operating at low chord Reynolds numbers in steady and unsteady flow. In *Numerical and Physical Aspects of Aerodynamic Flows IV*, pages 333–344. Springer, 1990.

D. M. Bushnell. Scaling: Wind tunnel to flight. *Annual Review of Fluid Mechacnics*, 38:111–128, 2006.

M. Casey and T. Wintergerste. *Best practice guidelines*. European Research Community on Flow, Turbulence and Combustion – Special Interest Group on Quality and Trust in Industrial CFD., 2000.

M. Casey, T. Wintergerste, and S. Innotec. Best practice guidelines. *European Research Community on Flow, Turbulence and Combustion – Special Interest Group on Quality and Trust in Industrial CFD.*, 2000.

CD-adapco. Validation of STAR-CCM+ for external aerodynamics in the aerospace industry. Briefing.

CD-adapco. State of the art CFD simulation for aerospace aerodynamics. Webinar, 2012.

CD-adapco. User Guide – Version 10.02. *Star-CCM+ Documentation*, 2015.

D. R. Chapman, H. Mark, and M. W. Pirtle. Computers vs. wind tunnels for aerodynamic flow simulations. 1975.

V. Ciobaca, S. Melber-Wilkending, and M. Pott-Pollenske. A CFD process chain for simulating open windtunnel test sections. 2009.

A. S. Committee et al. AIAA Guide for the Verification and Validation of Computational Fluid Dynamics Simuations (G-077-1998), 1998.

CSEM. Flexible distributed pressure sensing strips. URL: http://www.csem.ch/home, accessed May 23rd, 2016.

V. De Brederode, P. Jorge, J. Marcelino, and R. Patraquim. Aerodynamics of the Armor X7 UAV. In *AGARD Conference Proceedings*, pages 14–15, 1996.

A. Deperrois. About XFLR5 calculations and experimental measurements. 2009a.

A. Deperrois. XFLR5: Analysis of foils and wings operating at low Reynolds numbers. *Guidelines for XFLR5*, 2009b.

M. Drela. XFOIL: An analysis and design system for low Reynolds number airfoils. In *Low Reynolds number aerodynamics*, pages 1–12. Springer, 1989.

S. Eder, K. Hufnagel, and C. Tropea. Semi-span testing in wind tunnels. In *25th Int. Congress of the Aeronautical Sciences, ICAS*, 2006.

P. Ewing. Best practices for aerospace aerodynamics. CD-adapco, South East Asian Conference, Singapore, 2015.

K. J. Fidkowski and D. L. Darmofal. Review of output-based error estimation and mesh adaptation in computational fluid dynamics. *AIAA journal*, 49(4):673–694, 2011.

G. M. Gatlin and R. J. McGhee. Study of semi-span model testing techniques. *AIAA Paper 96*, 2386, 1996.

A. L. Heyes and D. A. Smith. Rapid technique for wind-tunnel model manufacture. *Journal of Aircraft*, 41(2):413–415, 2004.

H. H. Heyson. Rapid estimation of wind-tunnel corrections with application to wind-tunnel and model design. *NASA Technical Report*, 1971.

C. Hirsch. *Numerical Computation of Internal and External Flows: The Fundamentals of Computational Fluid Dynamics*. Butterworth-Heinemann, 2007.

H. Hu and Z. Yang. An experimental study of the laminar flow separation on a low Reynolds number airfoil. *Journal of Fluids Engineering*, 130(5):051101, 2008.

D. Jackson. Pressure sensitive paint – summary. URL: http://www.aerospaceweb.org/design/psp/summary.shtml, accessed May 23rd, 2016.

M. Jahanmiri. Pressure sensitive paints: the basics & applications. Technical report, Chalmers University of Technology, 2011.

R. Johnson. *The Handbook of Fluid Dynamics*. Mechanical Engineering. Springer Berlin Heidelberg, 1998. ISBN 9783540646129. URL `https://books.google.pt/books?id=JBTlucgGdegC`.

E. M. Kraft. *After 40 Years Why Hasn't the Computer Replaced the Wind Tunnel?* Defense Technical Information Center, 2010.

R. Langtry and F. Menter. Transition modeling for general CFD applications in aeronautics. *AIAA paper*, 522(2005):14, 2005.

R. Langtry, F. Menter, S. Likki, Y. Suzen, P. Huang, and S. Völker. A correlation-based transition model using local variables - part II: test cases and industrial applications. *Journal of Turbomachinery*, 128 (3):423–434, 2006.

B. E. Launder and D. Spalding. The numerical computation of turbulent flows. *Computer Methods in Applied Mechanics and Engineering*, 3(2):269–289, 1974.

LEAP CFD Team. Tips and Tricks: Turbulence Part 2 - Wall Functions and Y+ requirements. URL: http://www.computationalfluiddynamics.com.au/tips-tricks-turbulence-wall-functions-and-y-requirements/, accessed May 23rd, 2016.

Linkoping University. Research at computational mathematics. URL: https://liu.se/mai/bm/forskning?l=en, accessed May 23rd, 2016.

P. Lissaman. Low-Reynolds-number airfoils. *Annual Review of Fluid Mechanics*, 15(1):223–239, 1983.

M. Lombardi G, Salvetti and M. Morelli. Numerical analysis of blockage effects in slotted wind tunnels. *ICAS Congress*, 2000.

P. Malan, K. Suluksna, and E. Juntasaro. Calibrating the Gamma-ReTheta transition model for commercial CFD. In *47th AIAA Aerospace Sciences Meeting*, pages 5–8, 2009.

R. Maltby. Flow visualization in wind tunnels using indicators. Technical report, DTIC Document, 1962.

J. Marchman. Aerodynamic testing at low Reynolds numbers. *Journal of Aircraft*, 24(2):107–114, 1987.

J. Marchman. Semi-span testing at low reynolds number. In *AIAA, Aerospace Sciences Meeting & Exhibit, 36 th, Reno, NV*, 1998.

J. Marchman and A. Abtahi. Aerodynamics of an aspect ratio 8 wing at low Reynolds numbers. *Journal of aircraft*, 22(7):628–634, 1985.

J. Marchman, A. Abtahi, V. Sumantran, and Z. Sun. Effects of aspect ratio on stall hysteresis for the Wortmann airfoil. *AIAA Paper*, 1770:1985, 1985.

M. D. Maughmer and M. S. Selig. Low Reynolds Number Airfoil Design. In *Proceedings of the Conference on Low Reynolds Number Airfoil Aerodynamics, Edited by T.J. Mueller*, page 15, 1985.

B. McGranahan and M. Selig. Surface oil flow measurements on several airfoils at low Reynolds numbers. In *21 st AIAA Applied Aerodynamics Conference*, 2003.

B. G. McLachlan and J. H. Bell. Pressure-sensitive paint in aerodynamic testing. *Experimental Thermal and Fluid Science*, 10(4):470–485, 1995.

S. Melber-Wilkending, A. Heidebrecht, and G. Wichmann. A new approach in CFD supported wind tunnel testing. In *25th International Congress of the Aeronautical Sciences, ICAS, Ham-burg*, volume 3, 2006.

M. R. Mendenhall, P. M. Stremel, and M. C. Hegedus. A best practices system for reduced uncertainty in CFD. ICAS, 2006.

F. R. Menter. Zonal two equation k-turbulence models for aerodynamic flows. *AIAA paper*, 2906:1993, 1993.

F. R. Menter. Two-equation eddy-viscosity turbulence models for engineering applications. *AIAA journal*, 32(8):1598–1605, 1994.

F. R. Menter. Turbulence modeling for engineering flows. *Technical Paper, ANSYS inc*, pages 1–25, 2011.

F. R. Menter, R. Langtry, S. Likki, Y. Suzen, P. Huang, and S. Völker. A correlation-based transition model using local variables - part I: model formulation. *Journal of Turbomachinery*, 128(3):413–422, 2006.

W. E. Milholen, N. Chokani, and R. J. McGhee. Development of semispan model test techniques. *Journal of aircraft*, 33(6):1115–1122, 1996.

J. Morgado and J. Sousa. O Programa de Investigação e Tecnologia em Veículos Aéreos Autónomos Não-tripulados da Academia da Força Aérea. *Cadernos do IDN*, pages 9–24, 2009.

T. J. Mueller. The influence of laminar separation and transition on low Reynolds number airfoil hysteresis. *Journal of Aircraft*, 22(9):763–770, 1985.

T. J. Mueller and J. D. DeLaurier. Aerodynamics of small vehicles. *Annual Review of Fluid Mechanics*, 35(1):89–111, 2003.

J.-D. Muller. Grid generation tools. URL: http://www.ae.metu.edu.tr/tuncer/ae546/prj/delaundo/, accessed May 23rd, 2016.

NASA. Hybrid Wing Body (HWB) oil visualization. URL: https://www.nasa.gov/, accessed May 23rd, 2016a.

NASA. Boeing Sugar Volt semi-span model. URL: https://www.nasa.gov/, accessed May 23rd, 2016b.

ONERA. Flow field survey visualization. URL: http://windtunnel.onera.fr/flow-field-survey-and-visualization, accessed May 23rd, 2016.

R. E. Rayle. *An investigation of the influence of orifice geometry on static pressure measurements*. PhD thesis, Massachusetts Institute of Technology, 1949.

S. Ristić. Flow visualisation techniques in wind tunnels: Part I - non optical methods. *Scientific Technical Review*, 62:1, 2007a.

S. Ristić. Flow visualisation techniques in wind tunnels: Part II - optical methods. *Scientific Technical Review*, 62:1, 2007b.

P. J. Roache. Quantification of uncertainty in computational fluid dynamics. *Annual Review of Fluid Mechanics*, 29(1):123–160, 1997.

M. S. Selig and B. D. McGranahan. Wind tunnel aerodynamic tests of six airfoils for use on small wind turbines. *Journal of Solar Energy Engineering*, 126(4):986–1001, 2004.

R. Shaw. The influence of hole dimensions on static pressure measurements. *Journal of Fluid Mechanics*, 7(04):550–564, 1960.

P. R. Spalart and S. R. Allmaras. A one equation turbulence model for aerodinamic flows. *AIAA journal*, 94, 1992.

A. Springer. Evaluating aerodynamic characteristics of wind-tunnel models produced by rapid prototyping methods. *Journal of Spacecraft and rockets*, 35(6):755–759, 1998.

F. Stern, M. Muste, M.-L. Beninati, and W. E. Eichinger. Summary of experimental uncertainty assessment methodology with example. Technical report, IIHR Report, 1999.

R. S. Swanson and T. A. Toll. Jet-boundary corrections for reflection-plane models in rectangular wind tunnel. *NASA Technical Report*, 1943.

T. A. Toll. Jet-boundary corrections for reflection-plane models in rectangular wind tunnels. *NASA Technical Report*, 1943.

N. Ulbrich. Wind tunnel wall interference corrections (a brief overview). Jacobs Technology In., Moffett Field, California, 2016.

University of Washington, College of Engineering. Flow visualization. URL: https://www.aa.washington.edu/AERL/KWT/techguide/flowviz, accessed May 23rd, 2016.

S. A. Viken, N. Favaregh, C. Zeune, and J. Dansie. Comparison of computational approaches for rapid aerodynamic assessment of small UAVs. 2014.

G. Visavale. Y+ Wall Function in CFD. URL: https://www.linkedin.com/pulse/20140725081243-58050580-y-wall-function-in-cfd, accessed May 23rd, 2016.

F. M. White and I. Corfield. *Viscous fluid flow*, volume 3. McGraw-Hill New York, 2006.

D. C. Wilcox et al. *Turbulence modeling for CFD*, volume 2. DCW industries La Canada, CA, 1998.

A. M. Wo and E. E. Covert. Unsteady aerodynamics of Wortmann FX63-137 airfoil at low Reynolds numbers. In *Low Reynolds number aerodynamics*, pages 206–217. Springer, 1989.

M. Zagnoni, A. Golfarelli, S. Callegari, A. Talamelli, V. Bonora, E. Sangiorgi, and M. Tartagni. A non-invasive capacitive sensor strip for aerodynamic pressure measurement. *Sensors and Actuators A: Physical*, 123:240–248, 2005.

Appendix A

Best Practice Guidelines

Best Practice Guidelines

CFD applied to UAV Aerodynamics with Star-CCM+

Geometry	
Parameter	Recommendations
Aerodynamic Body (airfoil, wing or aicraft)	● Use the highest quality and most up-to-date CAD model available ● If possible work on CAD geometry with the available internal tools ● Perform CAD bolean operations (e.g. add, subtract, intersect) instead of discrete bolean operations, so that the original geometry definition is not lost ● If importing the geometry from an external application, use parasolid (*.x_t) files. ● Split the body into multiple part surfaces for custom controls ● Remove any negletable details, especially those expected to be under local cell size. If this proves complicated at CAD level, due to CAD quality and tool limitations, repair the surface mesh manually ● Change the AoA by rotating the body ● Use models with finite trailing edges (for increased grid quality and numerical stability)
Domain	Square (2D) or Hexahedral with a symmetry plane (3D)

Physics	
Parameter	Recommendations
Flow	Segregated (ideal for incompressible fow simulations)
Turbulence Model	RANS with k-ω SST (Menter)
Transition Model	γ-Re_θ (with the free-stream edge defined as 4 times the estimated maximum boundary layer thickness)
Wall Treatment	Low y^+
Equation of State	Constant Density (incompressible flow, for mach numbers under 0.3)
Time	Steady
Viscous Regime	Turbulent
Space	Three or Two-Dimensional (use preliminary 2D simulations in order to define grid refinement requirements and solver settings when dealing with new problems with unkown physics phenomena)
Gradient Metrics	Gradients
Material	Gas (Air)
Air Properties	Unless complete experimental information is given to fully replicate those conditions computationally, International Standard Atmosphere air properties at Mean Sea Level (ISA-MSL) should be used and the testing Re number matched by changing the inflow velocity magnitude

Boundary Conditions	
Parameter	Recommendations
Far-field distance	60 chords or 10 body lengths or wingspans (whichever is greatest) in all directions
Upwind and lateral boundaries	Velocity Inlets
Downwind boundary	Pressure Outlet
Symmetry plane	Symmetry
Tu (inlet and ambient*)	0.001 (0.1%) to 0.01 (1%)
TVR (inlet and ambient*)	1 to 10

Mesh	
Parameter	Recommendations
Meshing Operations	Use Parts Based Meshing (PBM) for better control and automation
Type of mesh	Trimmed mesh (unstructured grid with hexahedral cells) with prism layers
Number of cells	~20 million (for full configuration simulations)
Base size	$1/10^{th}$ of the chord

Basic surface curvature	36 to 54
Cell size on lifting surfaces	10% of the base size (use 12.5%** with hexahedral cells)
Curvature on lifting surfaces	76
Additional local refinements (Includes surface and volumetric controls)	● Around leading, trailing edges and tips of lifting and control surfaces ● Downstream of lifting surfaces and control surfaces in order to capture vortices that are shed in these locations (up to 8 chords downstream of the body) ● Around protruding aircraft components (such as landing gears) ● At body (fuselage) junctions with lifting or control surfaces (wing and stabilizers) ● In the wake of the body (up to 10 chords downstream of the body) ● Use a single "near-field" volumetric control surronding all the above regions of interest in order to control the placement of cell size transition into the reference base size. Outside this volume, cell size may increase gradually towards maximum cell size at the uter boundaries. This strategy can also be adopted in small critical volumes with between different cell sized surfaces, for example.
Minimum cell size	1/4th of the trailing edge thickness
Maximum cell size	At least one chord, body length or wingspan, whichever is higher. Also, this cell size should be imposed in the outer boundaries with custom controls
Minimum Face Quality	0.2
Volumetric Growth Rates	Very Slow
Surface Growth Rate	Typically from 1.05 to 1.30. Should match the volumetric growth rate, for grid consistency, especially at the symmetry boundary. A good practice is to choose the upper bound value and allow the volumetric control (***above***) to overide it and impose a consistent lower rate
Prism layer resolution	32
Stretching function	Hyperbolic Tangent
Stretching mode	Wall Thickness
Minimum Thickness Percentage	0.01
Layer Reduction Percentage	0 (for conformal prisms in all layers)
Maximum Wall y^+	0.1 to 1 (target value should preferably be in the order of 0.25)
First Cell Heigh Estimate, y_1 *** (for the Prism Layer Near Wall Thickness setting)	$y_1 = \frac{y^+_{target}\,\mu}{\rho\,U_\tau}$, where $U_\tau = \sqrt{\frac{\tau_\omega}{\rho}}$, $\tau_\omega = \frac{1}{2} C_f \;\; \rho \;\; U^2$ and $C_f = 0.058 Re^{-0.2}$
Boundary Layer Thickness Estimate, δ *** (for the Prism Layer Total Height setting)	Use Prandtl's expression for turbulent boundary layers over flat plates: $\delta \approx 0.37 \;\; Re^{-1/5} \;\; L$, where L is the component reference length

Solution Monitoring

Parameter	Recommendations
Convergence criteria	Residual and integral parameter of interest stabilization (e.g. C_L and C_D)
Reports and Monitors	Monitor residuals for all transported quantities and integral parameters of interest

* by activating the Ambient Source Term (ASM)

** percentage relative to base size. Also, increasing and decreasing hexahedral cell size should always be done by a factor of 2.

*** these parameters should be determined separately for each individual aircraft component (wing, fuselage, tail, etc.) and enforced through local controls.